

Measurements of B Meson Lifetime Ratios with the LHCb Detector

THÈSE N° 5280 (2012)

PRÉSENTÉE LE 30 MARS 2012

À LA FACULTÉ DES SCIENCES DE BASE
LABORATOIRE DE PHYSIQUE DES HAUTES ÉNERGIES
PROGRAMME DOCTORAL EN PHYSIQUE

ÉCOLE POLYTECHNIQUE FÉDÉRALE DE LAUSANNE

POUR L'OBTENTION DU GRADE DE DOCTEUR ÈS SCIENCES

PAR

Johan LUISIER

acceptée sur proposition du jury:

Prof. O. Schneider, président du jury
Prof. T. Nakada, directeur de thèse
Prof. K. Kirch, rapporteur
Dr O. Steinkamp, rapporteur
Dr N. Tuning, rapporteur



ÉCOLE POLYTECHNIQUE
FÉDÉRALE DE LAUSANNE

Suisse
2012

Remerciements

Un travail de doctorat est un travail de longue haleine, qui implique d'interagir avec bon nombre de personnes. Il est maintenant temps de remercier certaines personnes que j'ai pu côtoyer durant ces quatre ans de thèse et six années passées au sein du LPHE.

Premièrement, j'aimerais remercier mon superviseur, le Prof. Tatsuya Nakada, pour sa patience, ses conseils et pour les nombreuses corrections qu'il a apporté à ce document. Je suis également reconnaissant aux Prof. Aurelio Bay et Olivier Schneider qui m'ont donné l'opportunité de réaliser une thèse au LPHE.

Mes remerciements vont aussi à tous mes collègues du LPHE pour leur aide et pour la sympathique ambiance de travail : Yasmine Amhis, Fred Blanc, Joel Bressieux, Shirit Cohen, Greig Cowan, Hubert Degaudenzi, Levent Demirörs, Frédéric Dupertuis, Vincent Fave, Raymond Frei, Neal Gauvin, Rodolfo Gonzalez, Guido Haefeli, Pierre Jatton, Anne Keune, Viet Nga La Thi, Remi Louvot, Neus Lopez March, Raphaël Märki, Raluca Anca Muresan, Bastien Muster, Matt Needham, Julien Rouvinet, Lesya Shchutka, Paul Szczycka et Minh Tâm Tran. J'aimerais remercier tout particulièrement nos secrétaires Esther Hofmann et Erika Lüthi qui répondent toujours présentes lorsque l'on a besoin d'elles.

Finalement ma gratitude va à ma famille et à mon amie Sarah, qui partage mon existence depuis plus de cinq ans, pour leur soutien et leurs encouragements tout au long de mon parcours académique.

Novembre 2011

Johan Luisier

Résumé

L'expérience LHCb est une des quatre expériences principales au Grand Collisionneur de Hadrons (LHC) au CERN. Le détecteur LHCb est un spectromètre à un bras qui est consacré à la mesure de précision de la violation de \mathcal{CP} et à l'étude des désintégrations rares des hadrons b. L'énergie dans le centre de masse et la luminosité ont des valeurs jamais atteintes dans un collisionneur hadronique. LHCb a commencé de prendre des données en novembre 2009.

LHCb peut compter sur ses excellentes efficacités de reconstruction et de déclenchement, une très bonne résolution sur les mesures de masse et de temps de vol et un système d'identification des particules fiable pour atteindre la précision voulue. Ces performances ne peuvent être réalisées sans une calibration précise du détecteur. Par exemple, les données du Trajectographe Interne (IT) sont traitées par 42 cartes d'acquisition, appelées *TELL1*. Les données du Trajectographe Turicensis (TT) sont traitées par 48 cartes d'acquisition *TELL1*. Chacune de ces cartes d'acquisition a plus de 18'000 paramètres qui doivent être ajustés pour réduire le nombre de faux impacts dans les trajectographes. Dans le cas où ce nombre est trop élevé, l'efficacité de reconstruction des trajectoires est amoindrie.

La première partie de cette thèse discute la calibration des *TELL1s* de l'IT et du TT. La première étape a été de trouver un moyen d'extraire des données prises en l'absence de faisceau la valeur des paramètres nécessaires. Une fois ces paramètres réunis, une solution de stockage a été développée. Le choix s'est porté sur l'utilisation d'un fichier XML, puisque ce format était déjà utilisé pour la description de la géométrie du détecteur et pour les paramètres physiques du détecteur. En outre, un fichier XML offre la possibilité d'utiliser aisément les paramètres de la *TELL1* dans les programmes d'analyse de LHCb. Néanmoins il n'était pas possible de l'utiliser pour la prise de données, c'est à dire que ni les *TELL1s* ni le programme de contrôle n'avait la possibilité de lire ce fichier. Une librairie logicielle a dû être développée pour "traduire" l'information contenue dans ce fichier XML en un format pouvant être traité par le logiciel de contrôle.

La deuxième partie de la thèse traite de la mesure de l'efficacité de collection des impacts du Trajectographe Interne. Ces mesures se sont montrées être un moyen de surveiller l'état du détecteur. Plusieurs problèmes ont ainsi pu être découverts en analysant les efficacités obtenues. L'étude de cette efficacité en fonction des seuils d'agrégation a permis d'améliorer la discrimination du bruit dans l'IT et le TT en augmentant la valeur d'un de ces seuils.

Finalement, la dernière partie de la thèse couvre la mesure du temps de vie des mésons B dans trois canaux de désintégrations :

- $B^+ \rightarrow J/\psi(1S) (\mu^+ \mu^-) K^+$,
- $B^0 \rightarrow J/\psi(1S) (\mu^+ \mu^-) K^{*0} (K^+ \pi^-)$,
- $B_s^0 \rightarrow J/\psi(1S) (\mu^+ \mu^-) \phi (K^+ K^-)$.

Dans le cas du B^\pm et du B^0 , ces valeurs sont déjà bien connues, mais leur mesure représente une étape importante dans la mesure de ϕ_s , la phase responsable de la violation de \mathcal{CP} dans la désintégration $B_s^0 \rightarrow J/\psi(1S) \phi$. Les rapports des temps de vie sont aussi présentés : $\tau_{B^\pm} / \tau_{B^0}$, $\tau_{B_s^0} / \tau_{B^0}$ et τ_{B^-} / τ_{B^+} . Les deux premiers permettent de tester la théorie effective décrivant le comportement des quarks lourds (HQET), tandis que le dernier permet de tester la symétrie \mathcal{CPT} , qui est la pierre angulaire de la théorie des champs quantiques.

Mots-clefs : CERN, LHCb, Silicon Tracker, TELL1, temps de vie des mésons B.

Abstract

The LHCb experiment is one of the four main experiments at the Large Hadron Collider (LHC) at CERN. The LHCb detector is a one-arm spectrometer dedicated to precise measurements of the \mathcal{CP} -violation and studies or rare b-hadron decays. The centre of mass energy and luminosity (for a hadron collider) have both values never reached before. LHCb started data taking in November 2009.

LHCb relies on excellent reconstruction and trigger efficiency, very good mass and proper time resolution, reliable particle identification systems to achieve the wanted precision on \mathcal{CP} -violation parameters. These performances cannot be fulfilled without the detector to be calibrated. For instance, the Inner Tracker (IT) is readout by around a thousand chips, and the data are processed by 42 data acquisition cards, called *TELL1*. The Tracker Turicensis (TT) data are processed by 48 TELL1 boards. Each of these TELL1 boards has more than 18,000 parameters that need to be tuned in order to reduce the fake hits in the tracking systems. A high number of fake hits would result in poorer tracking performances.

The first part of this thesis discuss the calibration of the IT and TT TELL1 boards. The first step was to find a way to extract the needed parameter values from data taken without beam. Once the parameters were gathered, a way to store them for future usage had to be found. The chosen solution was to use XML file, since XML files were already used for the detector geometry description and detector conditions. The XML file offered a convenient way to use the TELL1 parameters in the software framework, but those parameters were of course also required for data taking, i.e. they have to be uploaded to the TELL1 boards. A software library had to be developed in order to ‘translate’ the information contained in the XML file into a format handled by the control software.

The second part discuss hit efficiency measurements in the IT. These measurements were shown to allow a monitoring of the detector status, as several hardware problems could be discovered by looking at the obtained efficiencies. Studies of the efficiency as a

function of the clustering threshold allowed to improve background rejection in IT and TT by increasing one of the clustering thresholds.

Finally, the last part covers the measurement of the B-meson lifetime in three decay channels:

- $B^+ \rightarrow J/\psi(1S) (\mu^+ \mu^-) K^+$,
- $B^0 \rightarrow J/\psi(1S) (\mu^+ \mu^-) K^{*0} (K^+ \pi^-)$,
- $B_s^0 \rightarrow J/\psi(1S) (\mu^+ \mu^-) \phi (K^+ K^-)$.

These values are already quite well known for B^\pm and B^0 , but their measurement represent a milestone in the measurement of the \mathcal{CP} violating phase ϕ_s in the $B_s^0 \rightarrow J/\psi(1S) \phi$ decay. Lifetime ratios are also presented: τ_{B^\pm}/τ_{B^0} , $\tau_{B_s^0}/\tau_{B^0}$ and τ_{B^+}/τ_{B^-} . The first two allow to probe the Heavy Quark Effective Theory (HQET), whilst the last one is a test of \mathcal{CPT} symmetry, foundation of the Quantum Field Theory.

Keywords: CERN, LHCb, Silicon Tracker, TELL1 board, B-meson lifetime.

Contents

I. The LHCb experiment at the LHC	3
1. The Large Hadron Collider at CERN	5
1.1. The LHC accelerator	5
1.2. Experiments at LHC	7
1.3. Luminosity	8
1.4. $p\bar{p}$ interactions	9
1.5. b quark production at LHC	10
2. The LHCb experiment at LHC	13
2.1. Asymmetric detectors	13
2.2. The LHCb experiment	14
2.3. Tracking system	17
2.3.1. The magnet	17
2.3.2. The vertex locator	18
2.3.3. The Tracker Turicensis	19
2.3.4. The Outer Tracker	19
2.3.5. The Inner Tracker	20
2.4. Particle identification	20
2.4.1. The RICH detectors	21
2.5. Calorimeter	22
2.5.1. The SPD and PS	22
2.5.2. The ECAL	23
2.5.3. The HCAL	23
2.6. Muon detector	23
2.7. The PVSS SCADA system	24
2.8. Summary	24

II. Silicon Tracker calibration and configuration	25
3. TELL1 board calibration	27
3.1. Introduction	27
3.2. TELL1 algorithms	28
3.2.1. Header correction	28
3.2.2. Pedestal subtraction	29
3.2.3. Common mode subtraction	29
3.2.4. Clusterisation	30
3.3. The XML database	31
3.4. Extraction of the parameters from data	32
3.4.1. Extraction sequence	33
3.4.2. The STVetraAnalysis package	34
3.4.3. STVetraAnalysis achievements	35
3.5. Summary	37
4. TELL1 board configuration with PVSS	39
4.1. Introduction	39
4.2. TELL1 parameters	41
4.2.1. Software-like parameters	41
4.2.2. Hardware-related parameters	43
4.3. The mapping file	44
4.4. Implementation	46
4.5. Summary	47
III. Inner Tracker studies	49
5. Efficiency study of the Inner Tracker	51
5.1. Introduction	51
5.2. Description of the method	52
5.3. Implementation	55
5.4. Results	56
5.4.1. Detector efficiency	57
5.4.2. Spillover efficiency	58
5.4.3. Efficiency vs. confirmation threshold	60
5.4.4. Spillover efficiency vs. confirmation threshold	62

5.5. Summary	64
IV. Lifetime and lifetime ratio measurements	65
6. Theoretical introduction	67
6.1. The Standard Model and discrete symmetries	67
6.2. B-mesons time development	68
6.2.1. Phenomenology	68
6.2.2. Relevant proper time distribution	74
6.3. Motivations	74
6.3.1. Indirect searches for new physics	74
6.3.2. Test of $\mathcal{CP}\mathcal{T}$	75
6.3.3. Heavy quark expansion theory	75
7. Used data sets	77
7.1. Data samples	77
7.2. Monte Carlo samples	77
8. Triggers	79
8.1. Hardware Trigger	79
8.2. High Level Trigger	80
8.3. Selected trigger lines	80
9. Event Selection	83
9.1. Selection strategy	83
9.2. Stripping and offline selections	84
9.2.1. $J/\psi(1S) \rightarrow \mu^+ \mu^-$ selection	85
9.2.2. $B^+ \rightarrow J/\psi(1S) K^+$ selection	86
9.2.3. $B^0 \rightarrow J/\psi(1S) K^{*0}$ selection	87
9.2.4. $B_s^0 \rightarrow J/\psi(1S) \phi$ selection	88
9.3. Cleaning the negative proper time tail	88
9.4. Best candidate selection	89
9.5. Selection efficiencies from Monte Carlo	91
9.5.1. Mass distributions from Monte Carlo	94
9.5.2. Proper time resolutions from Monte Carlo	96
9.6. Event yields in data	98

10. Lifetime extraction	101
10.1. Lifetime fitter	102
10.1.1. Modelling the background	102
10.1.2. Modelling the signal	103
10.2. Resolution model	103
10.3. Lifetime ratio extraction	104
10.4. Toy studies	104
11. Proper time acceptance	107
11.1. Method	107
11.2. Results	109
11.3. Conclusion	112
12. Results	115
12.1. Lifetime measurements	115
12.2. Proper time resolution	119
12.3. Lifetime ratio measurements	119
12.4. Cross-checks	120
12.5. Full fit results	120
13. Systematic uncertainties	123
13.1. Fit model	123
13.1.1. Signal mass model	123
13.1.2. Background mass model	124
13.1.3. Background time model	124
13.1.4. Time resolution model	124
13.2. Proper time acceptance correction	125
13.3. Other systematic uncertainty sources	125
13.4. Lifetime ratio systematic uncertainties	126
13.5. Summary	127
14. Conclusions	131
Appendices	132
A. Systematic uncertainty tables	133
A.1. Lifetime measurements	133

A.2. Lifetime ratio measurements	135
B. Additional plots	139
B.1. Lifetime fits	139
B.2. Lifetime ratio fits	146
C. Various mass plots	153
C.1. $B^+ \rightarrow J/\psi(1S) K^+$	153
C.2. $B^0 \rightarrow J/\psi(1S) K^{*0}$	154
C.3. $B_s^0 \rightarrow J/\psi(1S) \phi$	155
D. Resolution plots	157
Backmatter	159
Bibliography	161
List of Figures	165
List of Tables	169
Curriculum Vitae	173

Part I.

The LHCb experiment at the LHC

Chapter 1.

The Large Hadron Collider at CERN

The CERN is the European Organisation for Nuclear Research, the name comes from the french acronym for Conseil Européen pour la Recherche Nucléaire. It was created in 1954, when the twelve founding member states signed the Convention. The aims were to create a European collaboration dedicated to atomic physics, and to cope with the rising costs of instrumentation. Nowadays our understanding of matter is deeper than the nucleus and CERN is focusing on particle physics. It is now the biggest particle physics laboratory in the world, counting twenty European member states, six observers and several non-members states from all the World.

1.1. The LHC accelerator

The Large Hadron Collider [1] (LHC) at CERN is a 27 km circumference high luminosity proton-proton collider, which has a design centre of mass energy of $\sqrt{s} = 14$ TeV. Its main goal, but not the only one, is to test the Standard Model, and to reveal some ‘new physics’ (i.e. physics beyond the Standard Model).

The LHC is installed in the tunnel originally used for the Large Electron Positron collider (LEP [2]). LEP could not reach the TeV energy scale, as the synchrotron radiation losses are too high. Not only the LEP tunnel, any infrastructure existed at CERN, including the injection system (see Figure 1.1).

The LHC is the last element of a chain of different accelerators (Figure 1.2), which brings the protons to the wanted kinetic energy of 7 TeV. The protons are produced by a ion source at 100 keV, then accelerated by the *Linear Accelerator 2* (LINAC 2) to an energy of 50 MeV. They are then injected in a small synchrotron, the *Proton*

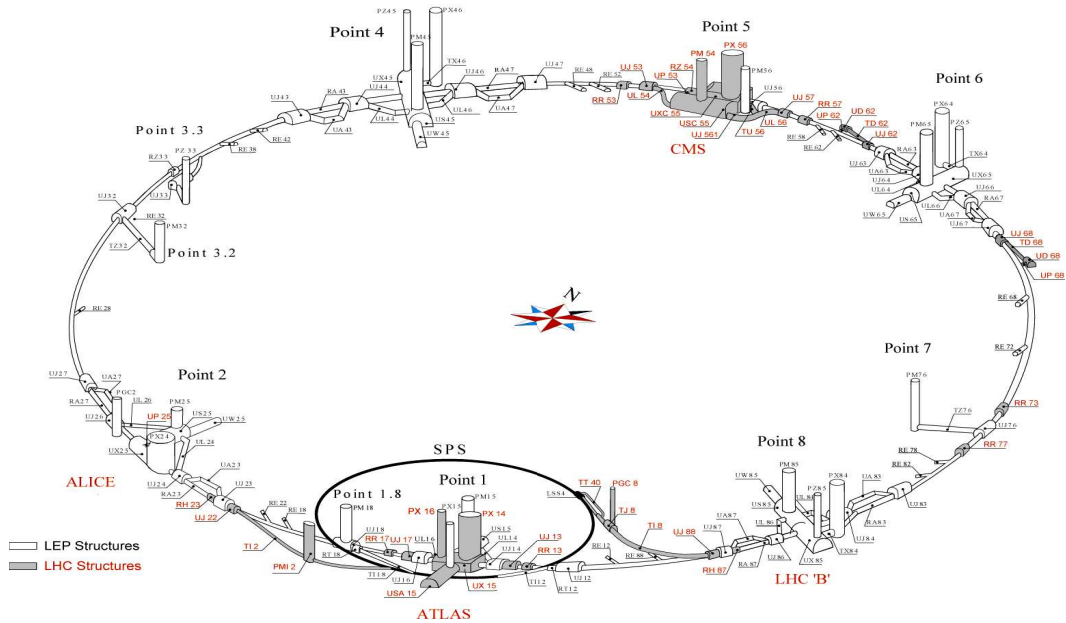


Figure 1.1.: LEP and LHC underground structures [3].

Synchrotron Booster (PSB), which increases their energy up to 1 GeV. The protons enter then the *Proton Synchrotron* (PS) and are boosted to 26 GeV before going in a third synchrotron, the *Super Proton Synchrotron* (SPS), which accelerates them up to 450 GeV. Once the beam has reached 450 GeV, it is injected in two counter-rotating directions in the LHC. The final energy of 7 TeV per beam is reached by the LHC itself, and is limited by the superconducting dipole magnetic field of 8.34 T.

The LHC is a $p\bar{p}$ collider and needs therefore one beam pipe per beam. A $p\bar{p}$ collider would require only beam pipe and might be easier to built, but the low production rate of anti-proton and the issues related to storage would not allow to get the desired luminosity. The LHC is also designed to accelerate heavy ions (Pb), for Quark Gluon Plasma (QGP) studies.

The production cross-section for a Higgs with a mass between 114 and 219 GeV in $p\bar{p}$ interactions increases with \sqrt{s} , but is still of the order of a few tens of pb at the LHC energy scale. This is why a high luminosity is required: the design value is $\mathcal{L}_0 = 10^{34} \text{ cm}^{-2} \text{ s}^{-1}$.

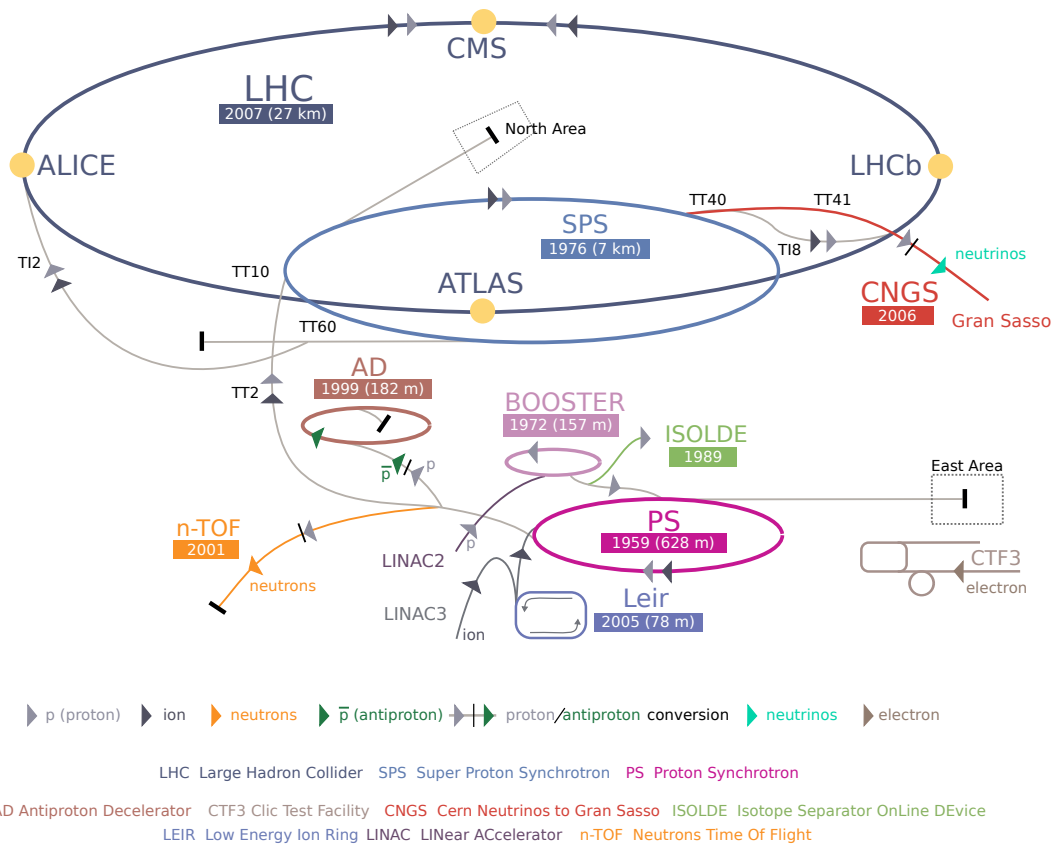


Figure 1.2.: LHC injection chain. The year when each accelerator / beam line was commissioned and the accelerator length is indicated.

1.2. Experiments at LHC

Along the LHC ring are located four main experiments: ATLAS, CMS, ALICE and LHCb, and two smaller ones: LHCf and TOTEM. Each of them is briefly described here below:

ALICE: A Large Ion Collider Experiment, dedicated to study of QGP, the state of matter appearing in ion collisions. The challenging issue is the high track multiplicity in Pb-Pb collisions.

ATLAS: A Toroidal LHC Apparatus System is a general purpose experiment, dedicated to Higgs boson search and discovery of physics beyond the Standard Model, such as supersymmetry. It is the LHC biggest detector (diameter of 25 m for a length of 44 m), and uses a toroidal magnetic field.

CMS: the Compact Muon Solenoid has a physics program similar to ATLAS. It is the heaviest LHC detector (12'500 tonnes) and has a strong magnetic field (4 T).

LHCb: the Large Hadron Collider beauty experiment is dedicated to b-hadron physics and precision measurement of \mathcal{CP} -violation in B-meson systems. It will be described with more detail in Section 2.2

LHCf: the Large Hadron Collider forward experiment is the smallest of the LHC experiments. It is meant to study particles generated in the 'forward' region of collisions. These studies are needed to check the hadronic model used to understand the ultra energetic cosmic rays. LHCf consists of two small detectors, located 140 m upstream and downstream of the ATLAS detector.

TOTEM: the TOTEM experiment will measure the total p p, elastic and inelastic cross sections. It also studies diffractive processes. It is located near the CMS interaction point, and covers the extreme forward region.

1.3. Luminosity

The luminosity at an interaction point reads:

$$\mathcal{L} = \frac{N_1 N_2 k_b f \gamma F}{4\pi \beta \varepsilon} \quad (1.1)$$

where N_i is the number of proton per bunch, k_b the number of bunch crossing at the interaction point in one revolution, f the revolution frequency at γ the relativistic factor. The normalised transverse emittance ε measures the beam compactness and the betatron function β measures the focusing power of the optics. Finally the F factor takes into account the crossing angle between the two colliding beams. An important number in the electronics design for the detectors is the colliding frequency $k_b f = 40$ MHz at an interaction point. This value determines the front-end electronic frequency. The design luminosity \mathcal{L}_0 will be reached at ATLAS and CMS interaction points. But at the LHCb interaction point the machine parameters are tuned to provide a luminosity of

$\mathcal{L}_{\text{LHCb}} = 2 \cdot 10^{32} \text{ cm}^{-2} \text{ s}^{-1}$. The reason why a smaller luminosity is used will be explained in Section 1.4.

1.4. p p interactions

CROSS-SECTIONS	
Total	$\sigma_{\text{tot}} = 100 \text{ mb}$
Inelastic	$\sigma_{\text{inel}} = 80 \text{ mb}$
c \bar{c} [4]	$\sigma_{c\bar{c}} = 6.10 \text{ mb}$
b \bar{b} [5]	$\sigma_{b\bar{b}} = 284 \text{ }\mu\text{b}$

Table 1.1.: Cross-sections at LHC at $\sqrt{s} = 7 \text{ TeV}$.

The relevant cross-sections in p p interaction at 7 TeV are given in Table 1.1. The inelastic cross-section σ_{inel} is an extrapolation based on data from UA1, CDF and D ϕ , but suffers from a large uncertainty. This cross-section defines the average number of inelastic interactions per bunch crossing:

$$\langle N_{\text{p p}} \rangle = \frac{\mathcal{L} \sigma_{\text{inel}}}{k_b f} \quad (1.2)$$

This means that the average number of p p interactions (i.e. primary vertices) in one bunch crossing is 17.4 for ATLAS and CMS (that see the nominal luminosity) and 0.37 for LHCb. This low value was chosen to avoid multiple interactions in one bunch crossing. Running at this luminosity results in an inelastic interaction in 30% of bunch crossings, meaning that the effective interaction rate is about 12 MHz. The number of p p inelastic interactions in one bunch crossing follows a Poisson distribution:

$$P(\mu, n) = \frac{\mu^n}{n!} e^{-\mu} \quad (1.3)$$

where μ is the average number of inelastic p p interactions per bunch crossing. It is linked to luminosity by the following relation:

$$\mu = \frac{\mathcal{L} \sigma_{\text{inel}}}{k_b f} \quad (1.4)$$

With $\sigma_{inel} = 80$ mb, the probability for a single inelastic interaction in one bunch crossing

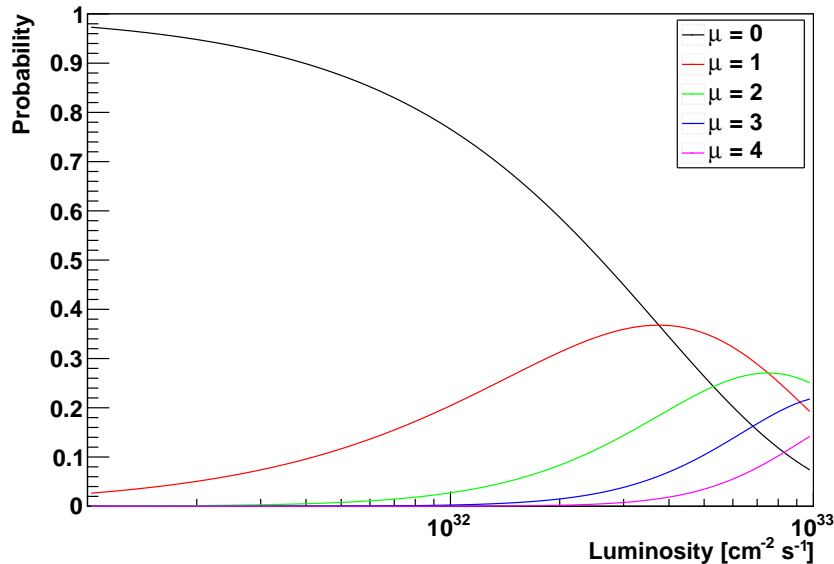


Figure 1.3.: Distribution function of number of events with 0, 1, 2, 3 and 4 interaction per bunch crossing.

reaches maximum at $\mathcal{L} = 4 \cdot 10^{32} \text{ cm}^{-2} \text{ s}^{-1}$ (see Figure 1.3). Unfortunately, the rate of multiple interactions is already too high at this luminosity. The chosen compromise is a luminosity $\mathcal{L} = 2 \cdot 10^{32} \text{ cm}^{-2} \text{ s}^{-1}$, value for which the tracking detectors occupancy is lower and radiation damages smaller. During the 2011 data taking, it was run at higher luminosities, this was possible as all subdetectors were designed to cope with a peak luminosity of $\mathcal{L} = 5 \cdot 10^{32} \text{ cm}^{-2} \text{ s}^{-1}$.

1.5. b quark production at LHC

In $p p$ interaction at high energies, $b \bar{b}$ quark pairs are produced by gluon or quark fusion (see Figure 1.4), and at the LHC energy, gluon fusion is expected to dominate. The $b \bar{b}$ production is predicted to be flat in rapidity. In the forward region, the pairs are strongly boosted longitudinally, thus both b and \bar{b} are close in rapidities. This fact motivated the geometry of the LHCb experiment, which will be described in Chapter 2.

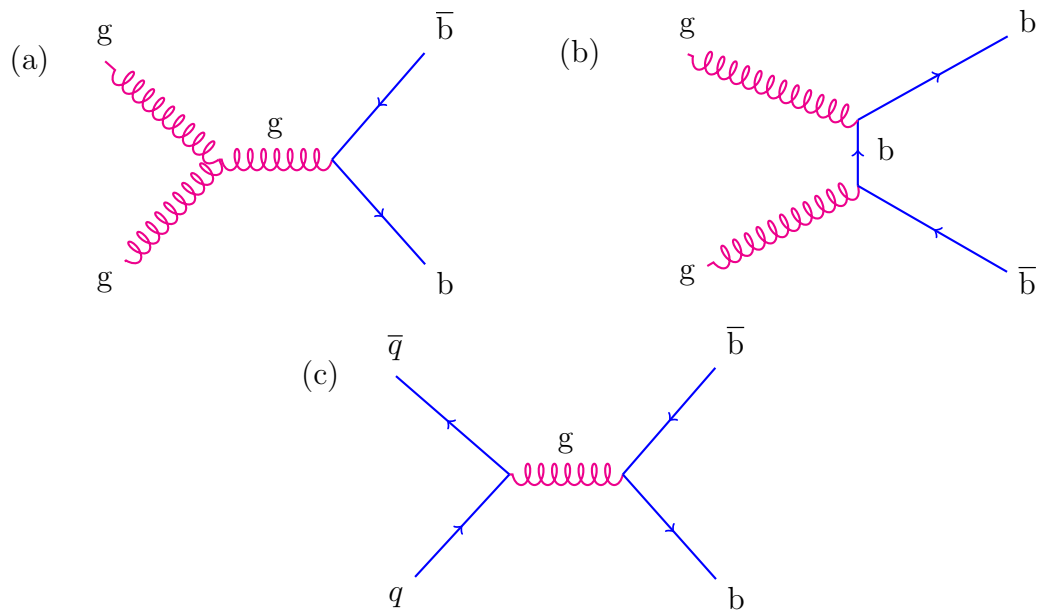


Figure 1.4.: $b\bar{b}$ production at the LHC: (a) s-channel gluon fusion, (b) t-channel gluon fusion and (c) quark fusion.

Chapter 2.

The LHCb experiment at LHC

2.1. Asymmetric detectors

The most obvious difference between LHCb and the two general purpose detectors ATLAS and CMS is their geometry: whilst ATLAS and CMS are usual 4π detectors, LHCb is a one arm spectrometer. This peculiar geometry was chosen because the produced b-hadrons are mostly produced in the same forward (or backward) cone at high energies. This is shown in Figure 2.1, where the two dimensional polar angle distribution of the $b\bar{b}$ pair is shown. The polar angle is defined with respect to the beam axis in the p p centre of mass system. Detecting both produced b-hadrons is crucial for the flavour tagging¹.

This geometry has other advantages:

- The b-hadrons produced along the beam axis have a larger boost than the ones produced in the central region. Their momentum is on average around 80 GeV/c, which corresponds to a mean flight distance of 7 mm. The high momentum tracks lead to a better vertex resolution, as the influence of multiple scattering is lower.
- The spectrometer can be built in an open geometry, meaning that the interaction region is not surrounded by all the detector elements. A vertex detector system which can be taken away from the interaction region during injection, using Roman Pot technique can be used. The sensor are positioned close to the beam during data taking, allowing to achieve a good vertex resolution.

¹Flavour tagging identifies the flavour of the quark, for instance if it is a b or a \bar{b} . It is used to know whether the produced particle was a B^0 or a \bar{B}^0 for instance.

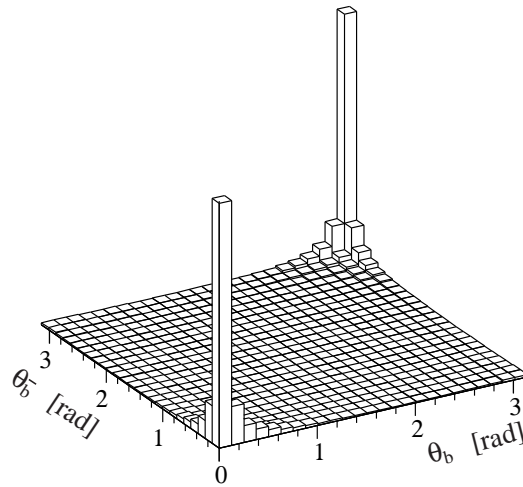


Figure 2.1.: Two dimensional polar angle distribution of produced $b \bar{b}$ pairs.

- In the forward region, the main momenta component is longitudinal, allowing to set low p_T triggers for electrons, muons and hadrons. Therefore the p_T triggers have a higher efficiency than in the central region.
- The open geometry makes installation and maintenance easier. It also allows easier upgrades of detectors.

The main drawback is that the particle density is higher in the forward region, radiation hard materials are thus required.

2.2. The LHCb experiment

LHCb is an experiment dedicated to study \mathcal{CP} -violation and rare decays in B-mesons systems. The Technical Proposal [6] was approved in 1998. The LHCb detector was built in the Delphi cavern, which has a length of about 20 meters along the beam axis. In order to accommodate the long detector, the interaction point was displaced to the edge of the experimental cavern (see Figure 2.2). A right-handed system of coordinate is used, its origin is located at the centre of the interaction region. The z axis goes along the beam direction and the y axis is vertical going upwards. The charged particles trajectories are bent in the $x - z$ plane by a dipole magnet. The angular acceptance is $10 - 300$ mrad in the $x - z$ plane and $10 - 250$ mrad in the $y - z$ plane. Around

35%² of the produced B-mesons can be studied, i.e. have their daughter particles in the acceptance.

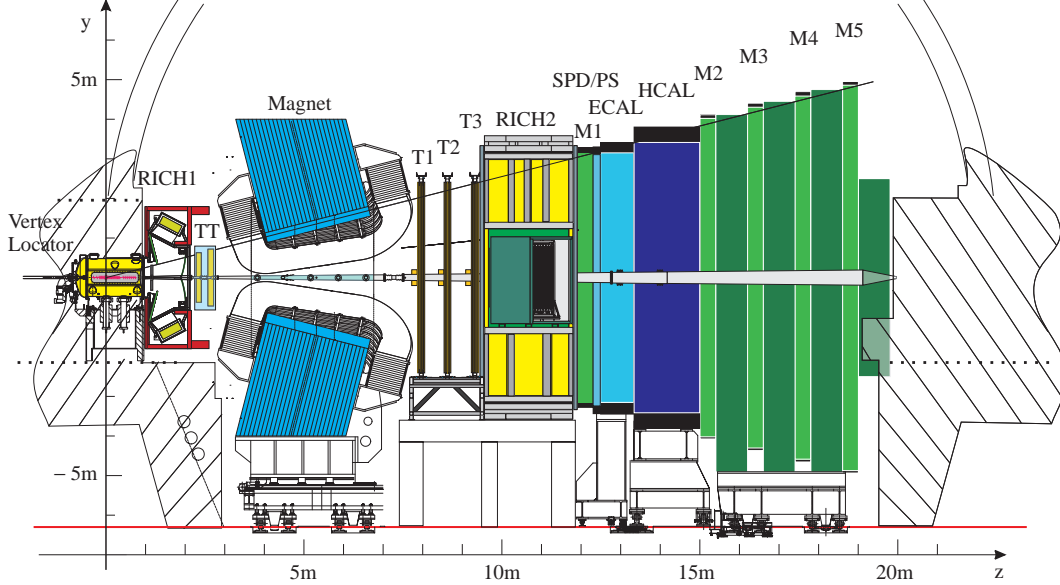


Figure 2.2.: The LHCb detector, side view. The hatched grey areas are the experimental cavern's walls.

LHCb key features are:

- **Vertex identification and decay length resolution.** An excellent proper time resolution is needed to study the B_s^0 fast oscillations, and extract the \mathcal{CP} asymmetries in the B_s^0 system. It is crucial that the primary and secondary vertices³ are precisely reconstructed, as well as the B_s^0 momentum.
- **Particle identification.** There are two key points in particle identification (PID). First π^\pm have to be distinguished from K^\pm (hadron ID) and second leptons have to be identified.
 - Hadron ID is used for flavour tagging with K^\pm or π^\pm and in the reconstruction of several decay channels, like:

* $B \rightarrow \pi^+\pi^-$ ($\mathcal{BR} = (4.8 \pm 0.5) \cdot 10^{-6}$) is polluted by $B \rightarrow K^\mp\pi^\pm$ ($\mathcal{BR} = (1.85 \pm 0.11) \cdot 10^{-5}$). The \mathcal{CP} asymmetry from $B \rightarrow \pi^+\pi^-$ is used for measuring α , corresponding to $\arg\left(-\frac{V_{td}V_{td}^*}{V_{ud}V_{ub}^*}\right)$, term coming from $b \rightarrow d$ transition.

²This value depends essentially on the B-meson flavour and on the decay channel.

³The primary vertex is the reconstructed position of the p p interaction, whilst the secondary vertex is the reconstructed position of the B decay.

* $B_s^0 \rightarrow D_s^\pm K^\mp$ has to be distinguished from $B_s^0 \rightarrow D_s^\pm \pi^\mp$, which has a 10 times larger branching ratio. The \mathcal{CP} asymmetry in $B_s^0 \rightarrow D_s^\pm K^\mp$ is used to extract $\gamma + \phi_s$, where $\gamma = \arg\left(-\frac{V_{ud}V_{ub}^*}{V_{cd}V_{cb}^*}\right)$ is the $b \rightarrow c$ transition and ϕ_s is the phase coming from interference between decay with and without oscillation of B_s^0 mesons.

– Leptons are used in various triggers and in flavour tagging.

- **A precise momentum resolution.** In order to reduce the combinatorial background in b-hadron reconstruction induced by the high number of tracks, an excellent resolution on the momentum measurement of the detected particles is required.
- **The trigger.** A high performance trigger is required to distinguish the minimum-bias events from the B-meson events. This is achieved by looking for high transverse momentum tracks and displaced vertices⁴.

LHCb subdetectors can be classified in four categories:

- **Tracking system:** consisting of the VELO, the Tracker Turicensis and three tracking stations. They are used for trigger, tracks and vertex reconstruction. The tracking system is described in Section 2.3.
- **Particle identification system:** consisting of two RICH⁵ detectors, using both aerogel and gas as radiators. The RICHes are described in Section 2.4.
- **Calorimetry:** electromagnetic (ECAL) and hadronic (HCAL) calorimeters are used to trigger on $b\bar{b}$ events and identify electrons, photons and hadrons. The calorimetry system is presented in Section 2.5.
- **Muon detector:** consisting of iron filters in between tracking chambers, it is used to identify muons, in the trigger and B-meson tagging. The muon detection is described in Section 2.6.

A more complete description is found in [7] and [8].

⁴Displaced vertices are made of tracks converging in a point different from the interaction point (called primary vertex), is equivalent to secondary vertices in the case of b-hadrons.

⁵RICH is an acronym for Ring Imaging Čerenkov.

2.3. Tracking system

The main goal of the tracking system is to achieve a relative resolution on the track momenta of $\sim 0.4\%$, resulting in a resolution of $\mathcal{O}(10 \text{ MeV}/c^2)$ on the reconstructed B-meson mass⁶. The elements contributing to this are:

- the magnet,
- the VELO, around the interaction point,
- the Tracker Turicensis (TT), located in front of the magnet,
- the three tracking stations, downstream of the magnet.

Both the VELO and TT are silicon microstrips, whilst the three tracking stations consist of two different detector technologies:

- in the inner region around the beam pipe, silicon microstrip detector is used, called the Inner Tracker (IT). It represents only 2% of the geometrical acceptance, but sees 20% of the produced tracks.
- in the outer part drift chambers are used, this detector is known as Outer Tracker (OT).

2.3.1. The magnet

The magnet geometry is determined by LHCb acceptance. The precision on the momentum measurement depends on the field value along the trajectory of the particle. The maximum value of the magnetic field is 1.1 T. The requirement of 0.4% precision of momenta up to 200 GeV/c is fulfilled with a bending power⁷ of 4 Tm for tracks coming from the interaction point region. The bending power has to be as uniform as possible, so that the track reconstruction precision is good enough, the expected deviation in acceptance is less than $\pm 5\%$. A warm magnet was chosen, for cost, mechanical resistance and construction time. It is made of 9 km aluminium wires put in a 120 kt steel yoke.

⁶This value depends on the decay channel.

⁷The bending power is given by $\int \vec{B} \cdot d\vec{l}$.

2.3.2. The vertex locator

Vertex reconstruction is a crucial point for LHCb. Due to the large boost of the produced b-hadrons, their flight distance in the detector is long enough to be measured, but a very good accuracy is required to separate the secondary vertices, i.e. where the B-meson decays, from the primary vertices, i.e. the p p interaction. The VELO designed decay time resolution for reconstructed b-hadrons is of the order of 50 fs.

The VELO plays a significant role in the High Level Trigger (HLT), because it allows to reconstruct displaced vertices, which is a signature of a B-meson decay.

These objectives are achieved by putting the detector as close as possible to the interaction point, as mentioned in Section 2.1. For this reason the detector and the electronics are in a vacuum tank. In order to protect the sensors from the beam during beam setup or ion data taking, they can be retracted.

The VELO consists of 21 stations of microstrip silicon disks. Each station is made of two silicon planes, measuring the radial and angular coordinate of the track respectively (Figure 2.3). The sensors lie in secondary vacuum ($\leq 10^{-4}$ mbar). The internal radius is constrained by the transverse beam size of LHC to 8 mm, whilst the external radius (42 mm) is given by engineering constraints. Resolution of primary vertex position is $\sim 40 \mu\text{m}$ in z and $\sim 10 \mu\text{m}$ in x and y . Spatial resolution of secondary vertices depends on the number of tracks, it varies between 150 and 300 μm in the z direction.

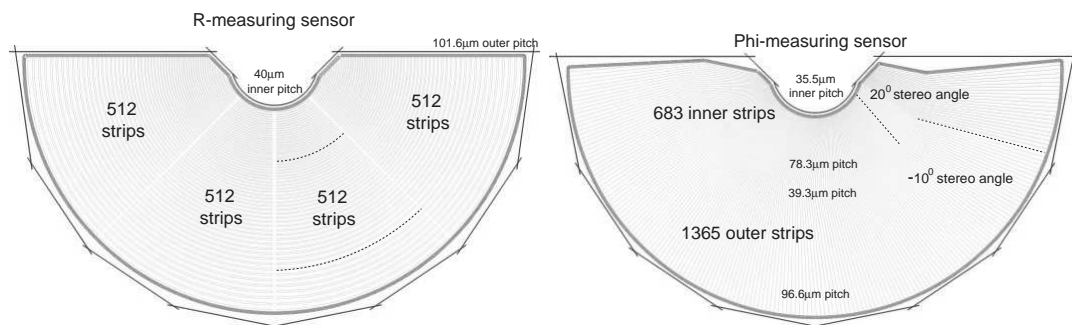


Figure 2.3.: VELO r (left) and ϕ (right) sensors.

2.3.3. The Tracker Turicensis

The TT, placed in front of the magnet, is crucial for the reconstruction of low momentum particles, since their trajectories are bent out of the detector acceptance when they pass through the magnet and are not reconstructed in the tracking stations.

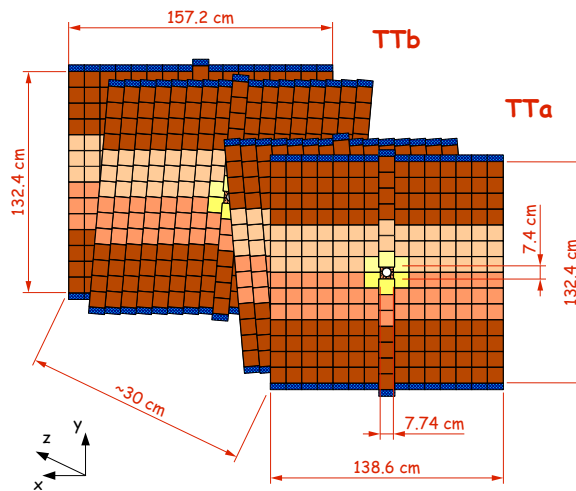


Figure 2.4.: TT layout, the four layers are shown, the dark blue parts are the readout electronics.

The TT is made of silicon microstrip detectors. It covers an area of $130 \text{ cm} \times 160 \text{ cm}$, and consists of four planes. The first and the last planes are vertical, the inner ones have stereo angles of $\pm 5^\circ$ (u or v layer respectively). There are 276 readout sectors, representing 141,312 channels.

2.3.4. The Outer Tracker

The OT, composing together with IT the T1, T2 and T3 tracking stations, measures the tracks with an angle with respect to the beam axis greater than 15 mrad. Since the particle density is low in those areas, drift chambers can be used. This allows to have a good spatial resolution with reasonable cost. The chosen gas mixture is Ar 70%, CF_4 28.5% and CO_2 1.5% in order to optimise the drift velocity.

The OT drift cells are made of straw tubes, and the signal collecting anode is located at the axis of the cylinder. In order to limit the drift time to 40 ns, the diameter of the

straw is 5 mm. Each station consists of four modules, from which the first and last are vertical (x layer) and the middle ones have stereo angles of $\pm 5^\circ$ (u or v layer).

2.3.5. The Inner Tracker

Straw tubes cannot cope with the high track density in the innermost regions of the acceptance. A dedicated detector was developed for those areas, using silicon microstrip technology. It has a cross-shape area around the beam pipe (Figure 2.5). Each station is again composed of four detecting layers, a u and a v layer in between two x layers. The station consists of four detector boxes, which contain microstrip detectors inside, named Top-, Bottom-, Access-, and Cryo-Box. The total active area is about 4.2 m^2 . There are 336 readout sectors, which represent 129,024 channels in total. The readout chain is the same as the one used for the TT, and will be briefly discussed in Section 3.1.

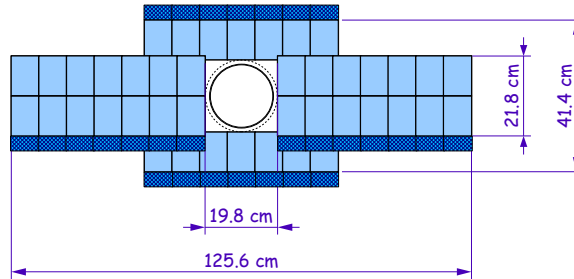


Figure 2.5.: Layout of the IT station 2 layer x . The light blue parts are the sensors, the dark blue parts are the readout electronics.

The front-end electronics is placed in the box, i.e. in the LHCb acceptance. Since the momentum resolution is dominated by multiple scattering, material budget minimisation is as important as radiation hardness.

2.4. Particle identification

As mentioned in Section 2.2, particle identification is crucial for LHCb. Measurement of \mathcal{CP} -violation parameters can only be performed if hadrons and leptons are correctly identified in a wide momentum spectrum. This identification is performed by Čerenkov detectors for π/K separation, calorimeter for electrons and photons, and the muon system for muons.

2.4.1. The RICH detectors

The Ring Imaging Čerenkov detectors allow to distinguish between pions and kaons. This is important to increase the signal to noise ratio in B-mesons decays and to get kaon tagging in \mathcal{CP} asymmetries measurements. There are two RICH detectors in LHCb, named RICH1 and RICH2. They allow to separate pions from kaons in a momentum window from 1 to 150 GeV/c, which covers around 90% of the pions and kaons produced in a B-meson decay. These particles are also used to tag the B-meson flavour.

The RICH detectors record the rings formed by Čerenkov photons emitted along the particle trajectory in the radiator. Once the particle momentum is known, the velocity determined from the measurement of the Čerenkov ring radius allows to separate particles with different mass, especially pions and kaons. The momenta and entry point in the RICH are given by the tracking system. Mirrors are focusing the photons on an array of photodetectors called *Hybrid Photon Detectors* (HPD). The HPDs are located outside of the LHCb acceptance, isolated from the magnetic field.

The only way to cover the 1 – 150 GeV/c momentum range is to use two RICHs, with three different refractive indices n . The polar angle of the particles is correlated with their momentum, and the most energetic particles have smallest angles ($20 \text{ mrad} < \theta < 50 \text{ mrad}$). For this reason the following radiators are used:

- silica aerogel, $n = 1.03$ for low momentum particles,
- C_4F_{10} , $n = 1.0015$ for intermediate range momentum particles,
- CF_4 , $n = 1.00046$ for high momentum particles.

RICH1 is located upstream of the magnet, in between the VELO and the TT. It is designed to identify particles with an momentum in the 1 – 40 GeV/c range. Its angular acceptance varies between 25 and 250 mrad in x and y axis. The RICH1 length is around 1 m, from which 5 cm are silica aerogel, the remaining 95 cm are filled with C_4F_{10} .

RICH2 is located downstream of the tracking stations. Its angular acceptance is 10 – 120 mrad in x and 10 – 100 mrad in y . The probed momentum range is 5 – 150 GeV/c. Its length is 170 cm and it uses CF_4 as radiator.

2.5. Calorimeter

The purpose of the calorimeter system is to detect and measure the total energy and impact point of hadrons, photons and electrons for analysis and Level 0 trigger. The electromagnetic calorimeter also has to identify tagging electrons for B-meson tagging, reconstruct π^0 and photons, especially if they are a B-meson decay product.

The LHCb calorimeter system consists of the *Scintillator Pad Detector* (SPD), a *PreShower* (PS), an electromagnetic calorimeter (ECAL) and a hadronic calorimeter (HCAL). Each of these devices is segmented in cells, the size of which varies depending on the detector region. The choice of the cell size is the result of a trade of between the number of readout channels, occupancy, and energy and position resolutions.

2.5.1. The SPD and PS

The SPD and the PS are located before and after a 12 mm thick lead converter (12 mm correspond to two radiation lengths⁸). They both consist of scintillator tiles, which are the same size as the corresponding ECAL module, with a thickness of 15 mm. The produced photons go first through wavelength shifter, then are guided to photo-multipliers located outside of the acceptance, below and above the detector. Minimum ionising particles (MIP) produce on average 25 photoelectrons in the scintillators. They allow to identify the beginning of electromagnetic showers by enhancing their origin with respect to the ECAL granularity.

Combination of SPD and PS allows to distinguish hadrons (or muons), electrons, and photons in the following way:

- hadrons (or muons) are seen as MIP in both SPD and PS.
- electrons are seen as MIP in SPD and showers in the PS,
- photons leave no signal in the SPD and are seen as showers in the PS.

⁸The radiation length is defined as the distance along which the energy of an electron decreases by a factor e^{-1} due to radiative losses only.

2.5.2. The ECAL

The ECAL consists of individual modules made of sixty-six 2 mm thick lead absorber in between 4 mm thick scintillator tiles. The total length of a module corresponds to 25 radiation lengths and 1.1 interaction length⁹. The total size of the ECAL is 6.3 m × 7.8 m. The photomultipliers are located at the back of the structure, to which the light is guided from the scintillators by optical fibres. The ECAL is segmented in three sections, each of them consisting of one type of module. All modules have the same cross-section, but the number of readout channel changes. At the very centre, there are 167 modules with 9 cells, in the intermediate section are 448 modules with 4 cells and finally the outer section is made of 2688 one-cell modules. The expected resolution on energy is $\frac{\sigma_E}{E} = \frac{10\%}{\sqrt{E}} \oplus 1.5\%$, where the first term represents statistical fluctuations and the second one is coming from non-uniformity of the detector and calibration uncertainties. The \oplus sign indicates that the two errors add in quadrature.

2.5.3. The HCAL

The HCAL is consisting of steel and scintillator tiles. The structure has on average 4 mm of scintillator for 16 mm of steel. The tiles are oriented along the particles trajectory. The production and extraction of the light is made in a similar way as for the ECAL. The length is 1.2 m, corresponding to 5.6 interaction lengths. The expected energy resolution is $\frac{\sigma_E}{E} = \frac{80\%}{\sqrt{E}} \oplus 10\%$.

2.6. Muon detector

The muon system consists of 5 stations (M1, M2, . . . , M5) which have a geometrical acceptance of ± 300 mrad in the x direction and ± 200 mrad in the y direction. M1 is located upstream the SPD, M2 to M5 downstream of the HCAL, and are sandwiched between iron filters. The total area is 435 m². The amount of absorber (calorimeters included) is 20 interaction lengths. The detector granularity is finer in the horizontal plane, to increase the precision of the momentum measurement. High p_T muons are used in the trigger, therefore the detector has been optimised for the information has to

⁹The interaction length is the distance that a particle travels before interacting with the medium.

be collected very fast (20 ns). The used technology is multiwire proportional chambers (MWPC).

2.7. The PVSS SCADA system

In the LHCb experiment, Prozessvisualisierungs- und Steuerungs-System (PVSSII) [9, 10] software is used to control the equipment, this is called *slow control*. PVSS is developed by the Austrian company ETM, and was chosen for its high scalability and modular design. The programmer is allowed to define their own data structure, called *datapoint types*, which are similar to C++ structures. They are not limited in complexity. Each device is then described by a *datapoint*, which is connected to the experiment.

PVSS is an event-driven software: an *Event Manager* is responsible for all communications (via TCP/IP protocol). It receives the data from the drivers and stores the current value in memory and sends them to an Oracle database via the *Database Manager*. It also distributes the information to managers that asked for it.

The user interface (UI) gets data from the database or acts on the device by sending data to the database, which is then sent to the device. The UI has read and write access to the datapoints in the database. The graphical user interfaces (GUI), called *panels*, are the objects the shift crew interacts with.

PVSS has its own scripting language for user-specific applications running in the control managers. This language is similar to C, with additional functions. PVSS allows GUI development, based on the Qt framework [11].

A cross-experiment framework was developed at CERN: the JCOP framework [12]. It provides advanced functionalities, drivers and protocols to communicate with the various pieces of hardware.

2.8. Summary

In this chapter the LHCb detector was discussed: the different subdetectors were described and the key features of LHCb were briefly presented.

The concept of slow control was introduced as well as the used software.

Part II.

Silicon Tracker calibration and configuration

Chapter 3.

TELL1 board calibration

3.1. Introduction

The Silicon Tracker (ST) consists of more than 270'000 channels, read out by about 2'000 analog front-end chips, called Beetles [13]. The data from the Beetles is digitised near the detectors and the digital signal transmitted by optical fibres to 90 TELL1 boards [14] in the counting house away from the detector, in the radiation safe area. The TELL1 boards perform the zero suppression¹ on events selected by the Level 0 trigger (L0), and then send the data to the CPU farm where events are reconstructed and selected by the High Level Trigger (HLT). The data processing in a TELL1 board is performed by *Field-Programmable Gate Arrays* (FPGAs). The FPGAs are programmable chips, allowing parallel and fast processing. Each TELL1 board has more than 18'000 parameters that need to be set for correct operation, parameters that will be discussed in Section 4.2.

Optimisation of the parameters is made using an emulator: a C++ program that has been developed in order to debug and test the TELL1 algorithms [15], briefly described in Section 3.2. The TELL1 emulator and the TELL1 boards share about 17'000 parameters², which have to be consistently set up. The chosen solution was to create a XML database, similar to the detector description (also known as DDDDB), and the detector conditions (also known as LHCBCOND). The former contains information about detector geometry, material specific masses, etc., and the latter contains alignment constants, noise levels, etc. This new database is a private *slice*, which is meant to be used by people in charge

¹This operation reduces the needed bandwidth, by not sending the signal on the strip not carrying any signal. This is developed in Section 3.2, and called *clusterisation*.

²Some of the TELL1 board parameters are not used by the TELL1 emulator, see Section 4.2.

of TELL1 algorithms or configuration, and is known as COND. The TELL1 emulator and the code to read and write the XML database run in the VETRA environment [16], which contains all the needed algorithms to read and process the data received by the TELL1 boards, and write the data used by the track reconstruction framework. The XML database is presented in Section 3.3, and is discussed in details (among other topics) in [17]. The parameters are extracted from data, the method is explained in Section 3.4.

3.2. TELL1 algorithms

The main tasks of the TELL1 are to perform the zero-suppression of the data sent by the front-end and to forward L0 selected data to the event builder. The zero-suppression is required to restrict the required bandwidth of the data to the CPU farm with a high event rate of 1 MHz. The zero-suppression is performed in four different steps (each of them performed by a dedicated algorithm):

- header correction,
- pedestal subtraction,
- common mode subtraction,
- clusterisation,

each of these algorithms and their key parameters are briefly described in the following subsections. A complete description of the algorithms is found in [18]. The TELL1 emulator performs a bit perfect emulation of the real TELL1 board, the following description is thus also valid for the TELL1 emulator algorithms. How these parameters are extracted or calculated will be developed in Section 3.4.

3.2.1. Header correction

It is observed that for a Beetle chip the noise of the first two (IT) or four (TT) channels of an analog port³ is higher than the average value of the other channels. This is understood as a crosstalk (inter-symbol crosstalk) from the header sent by the Beetle chip just before the data. The header contains an ‘event number’, called *pipeline column number*, and

³One TELL1 board reads out 24 Beetle chips, each of those having 4 analog ports, consisting in 32 channels. Thus 96 analog ports are read by a TELL1 board.

the parity of several beetle registers. It consists of four pseudo bits, pseudo meaning that it is a transmission of digital information via high and low analog values. A way of correcting this crosstalk was developed and correction values are extracted from data for each channel that needs to be corrected. These values are added to the received ADC for the corresponding channel. The TELL1 board has ninety-six analog ports. Each of these analog ports have their first six channels corrected, and the correction depends on the two last header bits (four configurations) and a parity bit from the beetle, building eight possible configurations.

3.2.2. Pedestal subtraction

The channel gain is adjusted such that the mean value of the received ADC value is around 128 (mid point of the ST dynamic range, which goes from 0 to 255). This mean value is known as the *pedestal value*. The pedestal subtraction is done by subtracting an 8-bit number from the received ADC value, before any other processing is done, and results in an ADC distribution centred at zero (with valid values between -128 and 127). The pedestal values can be fixed or updated event by event. An outlier rejection is used when updating the pedestal value, to avoid an overestimation in presence of signal. Problematic channels, such as dead or noisy channels, have to be disabled in the data (or *masked*), in order to avoid fake clusters. This means that the ADC value for those channels will always be set to zero after pedestal subtraction. Each channel can be disabled by a single bit value, called *pedestal mask*.

3.2.3. Common mode subtraction

The noise pattern in a readout sector is known to look like a banana due to common mode (which is a change of the baseline on an event by event basis): i.e. the noise⁴ is higher for the channels near the edges of the sector (see Figure 3.1). Common mode subtraction is used to reduce this effect and results in a flat noise pattern, by using linear correction on the received ADC values⁵. For each event, an average ADC value is computed and subtracted for each port (i.e. a set of 32 consecutive channels). A second average is then computed, from which the possible hits are excluded (i.e. the ADC is set

⁴The *noise* is referring to the width of the ADC distribution in absence of signal, whilst the mean of the distribution is called *pedestal*, this will be explained in Section 3.4.

⁵If the common mode was flat (i.e. independent of the channel number), such a common mode subtraction would still be applied.

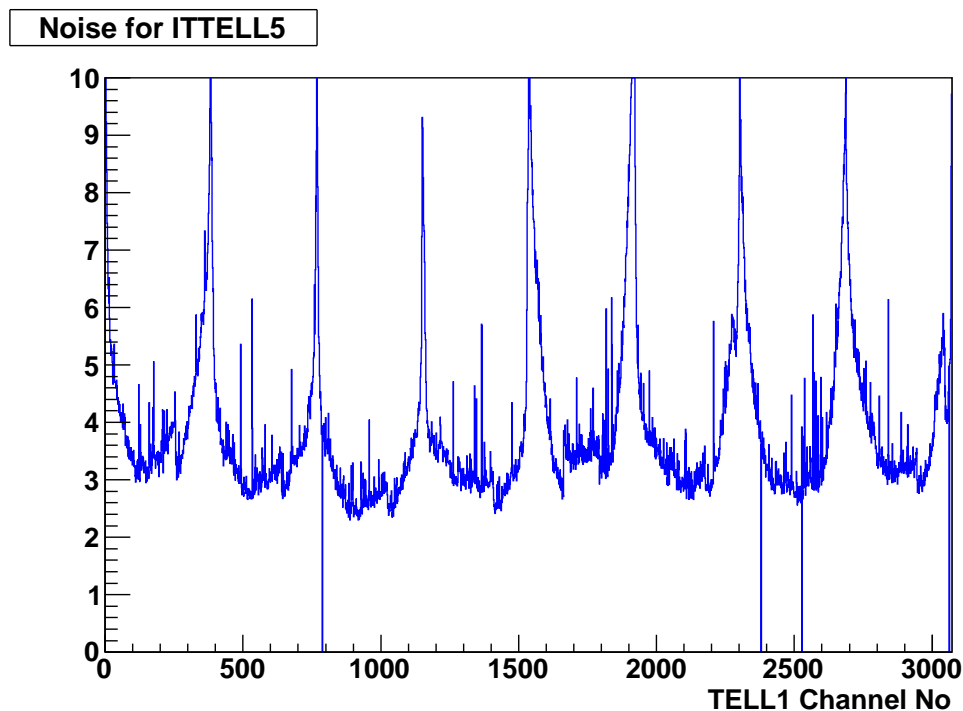


Figure 3.1.: Raw noise pattern in an IT TELL1 board. The banana shape is clearly seen for the eight readout sectors (one IT readout sector is 384 channels).

to zero). Assuming the distribution of the remaining ADC values in the port is linear against the channel number a slope is computed (using least square method and setting to zero the ADC values of possible hits). The ADC values are then modified, so that a slope computed in the exact same way would be zero. The detection of possible hits is done using a 8 bit threshold per channel, called CMS threshold, above which the readout value is considered to be signal and set to zero when computing the second average value and the slope correction. Rejecting signal is important because in presence of signal the average is overestimated, resulting in a lower signal value, and the slope would be either over- or underestimated, depending on the location (i.e. the channel number) of the signal.

3.2.4. Clusterisation

When consecutive channels have signal, they are bundled together and form a *cluster*, which was likely to be generated by a single track. The clusterisation process relies on two thresholds: an inclusion threshold (called hit threshold) and the confirmation threshold. The algorithm is quite simple: it loops over the channels and start to build a

cluster candidate if the ADC value of the channel is above the hit threshold. A cluster ends when the ADC of the channel becomes below the hit threshold or when the cluster already contains four channels. The clustering protocol is optimised for reduction of bandwidth and limits the cluster size to four channels. In order to decrease the rate of fake cluster due to noise, the total cluster charge (i.e. the sum of the ADC values) is required to be above the confirmation threshold. A third threshold, called SpillOver threshold, is used to flag the cluster for the online processing: if the cluster charge is bigger than the SpillOver threshold the SpillOver flag is set to 1. This flag can be used to discriminate between real clusters and cluster from the previous bunch crossing (called SpillOver).

3.3. The XML database

The XML database has the same structure as LHCBCOND: the file contains one element node⁶ per TELL1 board, called condition, as shown on Listing 3.1. The condition element node has two mandatory attribute nodes, the classID and the name fields. The name consists of the string ‘TELL1Board’ to which the TELL1 board source ID is appended. The classID is used when the XML file is read within GAUDI. The allowed children for a condition node are ‘param’ and ‘paramVector’, depending on how many values are stored in their data text node, i.e. if the child has only one value it’s a ‘param’, otherwise it’s a ‘paramVector’ (see small example in Listing 3.2). The tags param and paramVector have mandatory attributes: name, type and comment. The type attribute can be ‘int’ for integer values or ‘string’ for character strings or integer given in hexadecimal representation. The comment attribute is present to help the user to understand what is the information stored in the text node.

When the XML database was developed, its only purpose was to be used to configure the TELL1 emulator, therefore only thresholds, pedestal values and header correction values were present in the database (i.e. the so-called software-like parameters presented in Section 4.2.1). Then it has been extended and now each condition node has more than 270 children nodes. The IT and TT XML database files contain respectively 42 and 48 condition nodes (one per TELL1 board).

⁶For information about the XML terminology, please refer to [19].

```

<xml version="1.0" encoding="ISO-8859-1">
<!DOCTYPE DDDDB SYSTEM "conddb:/DTD/structure.dtd">
<DDDB>
<condition classID="9105" name="TELL1Board0">
<!-- ... -->
</condition>
<condition classID="9105" name="TELL1Board1">
<!-- ... -->
</condition>
<!-- ... -->
</DDDB>

```

Listing 3.1: Structure of the XML database file.

```

<condition classID="9105" name="TELL1Board0">
<param name="Tell_name" type="string"
comment="Name of the TELL1">
  ittell01
</param>
<paramVector name="ip_dest_addr" type="int"
comment="Destination IP">
  192 168 196 131
</paramVector>
<paramVector name="mac_dest_addr" type="string"
comment="Destination MAC address (hex)">
  0x00 0x01 0xE8 0x5D 0xE7 0x20
</paramVector>
<param name="detector_data_generator_enabled" type="int"
comment="Detector data generator enable">
  0
</param>
</condition>

```

Listing 3.2: Example of the four use cases of ‘param’ and ‘paramVector’, with ‘int’ or ‘string’ type.

3.4. Extraction of the parameters from data

The tracking efficiency needs a good rejection of fake clusters, since the tracking performances decreases when occupancy increases. This is why the TELL1 board has to reject as many noise clusters as possible. The different threshold values have therefore to be tuned wisely to achieve a sufficient rejection. This is why a specific package, called

STVETRAANALYSIS, was developed to extract the pedestal values, the thresholds and the header corrections.

Nomenclature: when talking about TELL1 data and TELL1 processing, a lot of jargon is used, which will be introduced here:

- *raw ADC's / raw bank* will refer to the TELL1 non-zero suppressed (NZA) input data,
- *pedestal subtracted ADC's / pedestal subtracted bank* refers to the TELL1 data after pedestal subtraction,
- *CMS ADC's (or LCMS ADC's) / CMS bank* will refer to the TELL1 data after common mode subtraction,
- the *pedestal bank* is the set of values that are subtracted from the raw data to obtain the pedestal subtracted bank,
- the *pedestal* is the mean of the distribution of the raw ADC's for one channel,
- the *noise* is the generic term for the RMS of the distribution of ADC's for one channel, if not specified refers to the *CMS noise*, i.e. the spread of the CMS ADC's distribution for one channel. The *pedestal subtracted noise* is the RMS of the pedestal subtracted ADC's for one channel, etc.

3.4.1. Extraction sequence

There are three different and unrelated operations which have to be performed to build a *calibration*. The pedestal value of each channel has to be extracted, header correction values have to be computed and the noise of each channel also needs to be extracted. Each of these steps relies on using the TELL1 emulator, which provides the pedestal subtracted bank, the pedestal bank and the CMS bank for each event.

The noise is assumed to be Gaussian, meaning that a cut on the ADC value of a channel can be converted into a probability to reject signal. This requires a good estimation of the noise, which can only be achieved if the pedestal are correctly set for each channel. In Section 3.2.1 it was mentioned that the header has an influence on the raw ADC's, influence which also impacts on the CMS ADC's. This means that the

pedestal values can be extracted only once the header correction values are correctly set. This leads to the following sequence:

1. extract the header correction values,
2. extract the pedestal values,
3. extract the noise values.

3.4.2. The **STVetraAnalysis** package

The **STVETRAANALYSIS** package contains all the algorithms needed to extract the different parameters from the data. With the exception of **STHeaderCorrection**, coded by Jeroen van Tilburg, all of the parameter extraction algorithms are my own. In general, running on at least 10'000 events is required to get meaningful results. Many scripts are present, which allow to manipulate the database, compare databases, etc. The package also contains two algorithms unrelated to calibration: **STMCThresholds**, by Matthew Needham, and **STTimeScan**, by Jeroen van Tilburg.

According to the sequence defined in Section 3.4.1, the first one to be used is **STHeaderCorrection**. It uses the pedestal subtracted bank as input and determines the 4608 header correction values per TELL1 board. It produces a XML file which contains the updated header correction values.

The next algorithm that comes into play is **STPedestalWriter**. Its input is the pedestal bank provided by the TELL1 emulator and it writes a XML file containing the new pedestal values.

The last involved algorithm is **STNoiseMonitor**. It was written to get the noise for each strip in a readout sector, values that are stored in the detector conditions database (LHCBCOND). This algorithm updates the noise values in LHCBCOND. A python script has to be run afterwards in order to update the XML file: it extracts the noise values from LHCBCOND and puts the threshold values in the XML file. All thresholds are integers, and are a multiple of the noise (which allows to cut on the signal to noise ratio).

For the sequence to produce meaningful numbers, many parameters have to be set for the used set of algorithms. In order to get the right **GaudiSequencer** with the correct options a configuration python file was created (a LHCb 'Configurable').

The package also contains an algorithm allowing to study the cluster rate, which was used to extract the optimal threshold using data without any signal. Another algorithm is used to write the XML file, adding comments on the author, a tag and a small description. Finally there are two other algorithms, the first one, **STBadLinkMasker**, allowing to mask the TELL1 channels which have a low noise, high noise, low ADC values, the second one, **STErrorMasker**, masking the analog ports or TELL1 link sending error banks. **STBadLinkMasker** was meant to detect all the faulty strips, like open strips, shorts, known from the sensor tests. The type of problems which can be seen with this algorithm are open channels and shorted pairs.

3.4.3. STVetraAnalysis achievements

The first task addressed to STVETRAANALYSIS was the analysis of the noise of the TELL1 boards for IT and TT. It showed that the noise had significant variations from one channel to the next (see Figure 3.2), which required to set the thresholds per strip. This was until then not foreseen, but fortunately allowed by the TELL1 board algorithms.

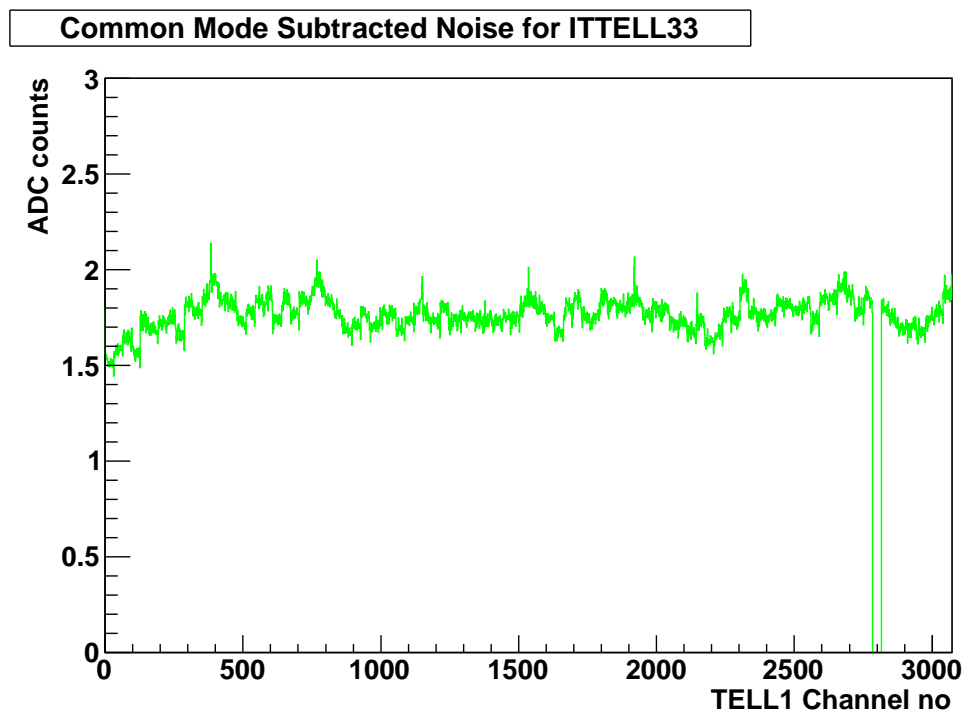


Figure 3.2.: CMS noise in an IT TELL1 board

When STVETRAANALYSIS was developed, only two header correction values per TELL1 board were implemented. Using an equivalent of **STHeaderCorrection** allowed

to show that a pair of header correction values per analog port was needed. Changes were thus implemented in the TELL1 algorithms to allow two correction values per analog port. Then the possibility to correct the first channel according to the two last bits of the pseudo-header, i.e. four values per port, was investigated within *STVETRAANALYSIS* and then implemented in the TELL1 algorithms. In the present situation the first six channels are corrected according to the two last bits of the header and the parity bit, which result in eight possible configurations.

The *STVETRAANALYSIS* package also contains a class allowing to monitor the cluster rates, **STScan**. This monitoring would allow to optimise the CMS, hit and confirmation thresholds. The studies showed that aiming at a $10^{-5} - 10^{-6}$ noise cluster rate⁷ would require a hit threshold of 3 – 4 and a confirmation threshold between 4 and 4.5. It also showed that there is almost no dependence on the CMS threshold. These values were used for data taking, but later on it was decided to put lower thresholds, to keep some more noise clusters as well, in order to monitor the status of the detectors.

The main purpose of *STVETRAANALYSIS* is to determine the TELL1 parameters, however some results of the various monitoring algorithms were used to tune the parameters and even to change the logic of the header correction algorithm. An example of by-product study was to identify the problematic channels, like open channels⁸ or shorted pairs⁹. This could in principle be deduced from the raw ADC values, the raw noise and the CMS noise, using tunable thresholds. Using the list of known problematic channels, the efficiency of the identification was studied. The conclusions were that:

1. it was not possible to identify all problematic channels,
2. the number of ‘healthy’ channels identified as problematic grew as the fraction of found problematic channels increased.

This is summarised in Table 3.1, where the fractions correspond to the ratio of found channels to the number of known problematic channels, using the aforementioned technique. The ‘False positive’ columns gives the number of healthy channels identified as problematic. This table indicates that any automatic check of the status of the channels would require a very complicated logic. This means that every appearing problem has to be investigate by looking at pedestal and noise distributions.

⁷The noise cluster rate is defined as the number of noise cluster per event and per channel.

⁸Open channels are channels which are not connected anymore to the readout chip.

⁹A shorted pair is a pair of channels which are connected, resulting in a sharing of the collected charge.

DETECTOR	SHORTED PAIRS		OPEN CHANNELS	
	Retrieved	False positive	Retrieved	False positive
IT	$\frac{33}{38}$	4	$\frac{18}{22}$	26
TT	$\frac{22}{33}$	11	$\frac{48}{82}$	11

Table 3.1.: **STBadLinkMasker** results. Fractions are indicating the ratio of found problematic to known problematic channels, the false positive indicates the number of healthy channels misidentified as problematic.

3.5. Summary

This chapter presented the TELL1 algorithms together with their key parameters. The XML file which contains all these parameters was also discussed. The package allowing to extract and manipulate those XML files, **STVETRAANALYSIS**, was described.

Chapter 4.

TELL1 board configuration with PVSS

4.1. Introduction

The TELL1 board parameters have to be calibrated in order to give meaningful data that can be used for physics. For instance if the thresholds are too low, there will be lots of clusters generated by the noise, slowing down the data taking (due to limited bandwidth in the event builder network) and increasing tremendously the timing of the track reconstruction algorithm.

In the experiment, the real TELL1 boards are configured with a PVSS *recipe*, which is a binary file that contains the name of the TELL1 registers¹ and the associated value (i.e. the register content). In order to create these recipes it was previously required to configure the board and then read back all the registers. Doing this operation required to have a direct connection to the TELL1 boards, and could not be used when LHCb was collecting data. The initial configuration is performed by an ASCII configuration file, which will be referred to as *cfg* file, read by a dedicated function from the TELL1 C-code library [20]. The writing of these *cfg* files is not very convenient, there is no standard way to read them within PVSS, and moreover the parameters are identified by a line number, which may change when the TELL1 board firmware is updated. Therefore it was decided to find a way to use the XML database to build recipes, using the same XML file to configure both the TELL1 emulator and the real TELL1 boards. This procedure would have many advantages compared to the method used previously. Since the TELL1

¹A register is a piece of memory, which in the TELL1 case is 32 bits wide, indexed by its address, which is a hexadecimal number, but aliased to a register name. For instance the register containing the maximal number of created cluster per FPGA, called `ST.CLUSTER_NUMBER.MAX.REG`, corresponds to the address `0x4003044` for the first FPGA.

emulator could only read XML files, a non trivial conversion would have been needed from the cfg to XML or the other way round. On top of that, the XML format has the advantage that it is both machine and human readable.

The developed framework is designed to work together with the general TELL1 framework component (called fwTell1 [21]). The user interface is a unique panel (see Figure 4.1), integrated in the TELL1 ‘Control Unit’ panel. Reading the XML database file uses a framework component, fwCondXML, providing wrappers around the PVSS native XML DOM parser. This library allows to perform many checks on the read file, ensuring that all the needed information is present. A complex data structure is provided, allowing to access any information from the XML database file using indices.

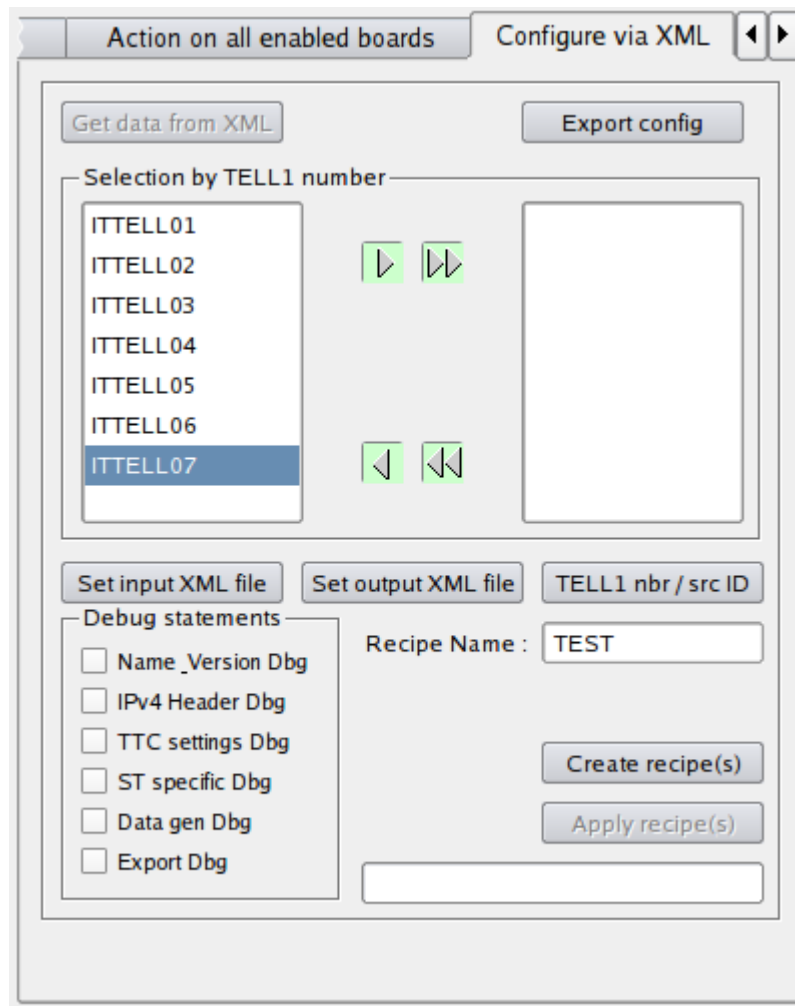


Figure 4.1.: User interface of the fwTell1XML component

A PVSS recipe is a file which links each register to the data it contains (see Section 3.1). The TELL1 registers are 32 bits wide, but the stored data can be from 1 bit (the pedestal

mask for instance) to 48 bits (the source and destination MAC addresses), which makes writing the data in the register highly non trivial. Either one single register contains several different pieces of information, or some information have to be spread over several registers. In order to know in which of the 341 TELL1 registers the data from the 270 element nodes from the XML files have to be written, a second XML file was used: the mapping file. The mapping file contains the same element nodes as the XML database file, but the data text nodes give information about the register name and the mask. The mask is a crucial information, since it prevents from overwriting, when multiples data fields have to be written in the same register (or RAM block²).

4.2. TELL1 parameters

The TELL1 parameters can be classified in two categories: the software-like and the hardware-related ones. The former set consists of the settings of the TELL1 algorithms, needed by both the emulator and the real TELL1 boards, and will be discussed in Section 4.2.1. The latter set consists of every setting that is needed for gigabit ethernet (GBE) communication, switching on/off optical receivers, controlling the throttle counters, etc. and will be discussed in Section 4.2.2. All of these parameters have to be written either in the FPGA registers (which are 32 bits wide and 1 word³ deep) or FPGA RAM (that are 32 bits wide and 128 words deep). A complete description of the parameters can be found in [22], here only a few examples are shown, presenting an overview of the number of parameters.

4.2.1. Software-like parameters

The software-like parameters are mainly thresholds for the four TELL1 algorithms, pedestal values and masks. These add up to 16'994 needed constants. On top of those there are other needed parameters for a TELL1 board to produce useful results⁴, such as

²A RAM block is a piece of memory corresponding to an array of words (which are 32 bits wide in the TELL1 case). It is indexed by a hexadecimal address, also aliased to a name, as for the TELL1 registers. The difference between registers and RAM blocks exists when reading / writing with PVSS, there is no fundamental difference at the implementation level.

³A word is a fixed size group of bits. The size is related to the natural unit of data the processor can handle. The usual size of a word is 32 or 64 bits. In this document, a words refers to a group of 32 bits.

⁴Even if the pedestal values and thresholds are incorrectly set, a TELL1 board will still send data, however it cannot be used for analysis.

‘process info’ settings, each of them enabling one of the four TELL1 algorithms. The input parameters that tune the TELL1 algorithms behaviour, with their granularity and size are described below. Knowledge of these is essential before discussing recipe building.

Header correction

As mentioned in Section 3.2.1, each of the 96 TELL1 board links have their first 6 channels corrected according the header configuration. Since there are 8 possible header configurations, the number of header correction values is 4608 per TELL1 board, to which two thresholds have to be added. These thresholds are used to determine if the received pseudo-bit is a ‘0’ or a ‘1’. The two thresholds are 8 bit integers, stored in one register per FPGA, and the header corrections are 4 bit signed integers (from -8 to 7) and are written in a 32 bits wide and 16 words deep RAM blocks (twelve blocks per FPGA).

Pedestal subtraction

Each of the TELL1 board channels have one pedestal value and a pedestal mask, making 6144 values per TELL1 board. Both the mask (1 bit) and the value (8 bit unsigned integers) are stored in the same RAM block. The used RAM blocks are 64 words deep and 32 bits wide, and there are twelve of them per FPGA.

Common mode subtraction

The common mode subtraction algorithm only parameter is the confirmation threshold, which is a 8 bit integer values. There is one of these per channel, and the 3072 values per TELL1 board are written in twelve RAM blocks per FPGA.

Clusterisation

The hit detection uses one hit threshold per channel, since the noise may vary from one channel to the next. Both the confirmation and SpillOver thresholds granularity is lower: there is only one per every set of 64 consecutive strips (called *processing channel*). This makes 3072 hit threshold values, plus 48 confirmation threshold and 48 SpillOver

threshold values, which add up to 3168 values. The 8 bit hit threshold values are stored in twelve RAM blocks per FPGA, and both confirmation and SpillOver threshold values (8 bits each) are written in the same register (twelve per FPGA).

4.2.2. Hardware-related parameters

Only the most important settings will be presented here, as there are many of them. An important subset of the hardware-related parameters is the collection of settings for the GBE ports of a TELL1 board. As an illustration of the complexity of writing into RAM blocks, the 16 words concerning the configuration of the first GBE port are given in Table 4.1. There are four ports, and the presented pattern is written four times (i.e. 64 words in total) in the same RAM block. Some very important parameters are present in there, such as source and destination MAC or IP addresses.

	31	23	15	7
0	Destination MAC address [47:16]			
1	Destination MAC address [15:0]		Source MAC address [47:32]	
2	Source MAC address [31:8]			<i>Src. addr.</i> [7:0]
3	Ethernet type		IP vers.	IHL
4	Total length		Identification	
5	Flag	Fragment offset		TTL
6	Header checksum		Source IP address [31:16]	
7	Source IP address [15:0]		Destination IP address [31:16]	
8	Dest. IP addr. [15:8]	<i>Dest. IP addr.</i> [7:0]		<i>Reserved</i>
9-15	<i>Reserved</i>			

Table 4.1.: GBE parameters, the *blue* fields are set according to the port number (0, ..., 3), the *magenta* ones are overwritten once the configuration is done. Only settings for the first GBE port are shown in the table. The reserved words are not used and thus set to zero. The numbers between square brackets indicates which bits of the data field are written where.

Another example are the bank class numbers. There is a number that identifies the bank class (error bank, pedestal bank, no zero suppressed bank, etc.) per detector type

(such as IT, TT, VELO, etc.). If these numbers are not set correctly, the event builder is unable to decode the information.

The trigger settings are also controlled by the hardware-related parameters, for example the source of the trigger has to be specified. TELL1 boards can receive triggers either from ‘Timing, Trigger and Control’ (TTC), used for standard data taking (in global or stand-alone mode), or ‘Experiment Control System’ (ECS), which only allows stand-alone data taking. If ECS trigger is used, the trigger type also has to be set, which will then determine the type of sent data (zero suppressed or non zero suppressed).

Checks on the received and processed data are performed by the TELL1 board, which require many thresholds. For instance the height of the header pseudo bits is not within an acceptable range, the TELL1 board sends an error bank together with the data.

4.3. The mapping file

As mentioned in Section 4.1, the most difficult challenge was to find a way to match each of the 270 child nodes of a TELL1 condition node from the XML database file to the corresponding register of the TELL1 board. The chosen solution was to build what is called the mapping file. This mapping file is very similar to the XML database file: it contains one condition node, whose children have the same names as the children of a condition node of the XML database file. The only difference is that the data text nodes contain information about the type (‘int’ or ‘string’), the register name and the mask. If there are more than one target register, the next register name and mask are appended:

```
data_type register_name_1 mask_1 register_name_2 mask_2 [...]
```

There is no additional complication coming from the fact that several values have to be written in the same location. The n input values are equally and automatically distributed among the m registers, in the sense that the first $\frac{n}{m}$ values goes into the first registers, the next $\frac{n}{m}$ into the second one, etc. Only 4 use cases are known:

- $m = 1$, meaning that the n values will be put together in the same register.
- $\frac{n}{m} = 1$, meaning that each of the n value will go in its corresponding register.
- $n = 1$ and $m > 1$, for which the only value will be written m times in the m different registers.

- $\frac{n}{m} = k > 1$, meaning that the data is grouped in m subsamples, each of them written in its corresponding register.

The situation is more complex with RAM blocks. Usual registers of a TELL1 board are 1 word wide (1 word is 32 bits, i.e. 4 bytes), but RAM block are 1 word wide and x word deep. It can be seen as an array of usual registers, the only difference is that it is written in one go, meaning there is only one address. The way these data are handled in fwTell1XML is to build an array containing $data_1$, $data_2$, etc. But then arises the problem that multiple information can be written in the same RAM block, and they might not appear in the desired order (i.e. the order used in the XML file and the one in the recipe may be different). That is the reason why a new syntax is introduced: an index is added, and this index represents the position of the data in the array, which is related to its position in the RAM block. For consistency the index is given in hexadecimal

```
<condition classID="9105" name="TEMPLATE">
<paramVector name="Tell_name" type="string"
comment="Name of the TELL1">
  s NULL
</paramVector>
<paramVector name="ip_dest_addr" type="string"
comment="Destination IP">
  i SL.CMNMEM.Ipv4Header 0xFFFFFFFF 0xD
</paramVector>
<paramVector name="mac_dest_addr" type="string"
comment="Destination MAC address (hex)">
  s SL.CMNMEM.Ipv4Header 0xFFFFFFFFFFFF 0x1
</paramVector>
<paramVector name="detector_data_generator_enabled"
type="string"
comment="Detector data generator enable">
  i PP0.CMNCTRL.PPCtrlReg0 0x00000040
  PP1.CMNCTRL.PPCtrlReg0 0x00000040
  PP2.CMNCTRL.PPCtrlReg0 0x00000040
  PP3.CMNCTRL.PPCtrlReg0 0x00000040
</paramVector>
</condition>
```

Listing 4.1: Example of the mapping file entries corresponding to the XML database file example shown on Listing 3.2. Note that every child node is here a ‘paramVector’, and the type is always ‘string’.

representation, as the data from the mapping file text nodes are expected to be character strings. The corresponding mapping content is thus:

```
data_type register_name mask index
```

An example, corresponding to the one presented in Listing 3.2 is shown in Listing 4.1.

4.4. Implementation

The implementation details and how to use the PVSS component are found in [17]. Here only a brief description will be presented. The PVSS component, called fwTell1XML, must do the following operations for each TELL1 board:

- get the TELL1 parameters from the XML database file,
- get the register information from the mapping file,
- write each parameter in its right place,
- save the recipe.

The parameters have to be converted from integer or string (for hexadecimal numbers) into the byte representation in PVSS and stored in an array of bytes, which order is given by what is called the recipe type. The recipe type defines how many registers have to be written, their order and their type.

The reading the parameters and the register information is performed very carefully, the presence of the element nodes is checked, the number elements in the data text node and their type is also checked. The drawback is that the description of the element nodes (i.e. the list of the names) has to be changed in five different places, but this also ensures that the XML database file, the mapping file and the component are compatible. This mechanism is implemented in the fwCondXML PVSS component, written by Kurt Rinnert. For each read XML file, a configuration file has to be written, which is an *a priori* description of the expected content.

The component consists of two libraries describing the content of the mapping file and the XML database file respectively. A third library contains the specific functions (fwTell1XML.ctl). A graphic user interface, known as panel, allows the user to select the input XML database file, the list of TELL1 boards for which a recipe will be created, etc.

For each TELL1 board, the values are read from the XML database file and stored as word arrays. The data has to be formatted, meaning that the mask is applied to check that the data width is not too large and correctly translated in to bytes. As an example, consider the ‘`orx_beetle_disable_0`’ parameter, which allows to disable any of the first twelve input links of the TELL1 board. This parameter represents two sets of six bits (one set per FPGA). The corresponding mask is `0x00003F00`, which has six active bits (bits 8 to 13), which means that the value ‘67’ ($67 = 0b1000011 = 0x43$) will first be truncated to ‘3’ ($3 = 0b11 = 0x3$), and then written as ‘768’ ($768 = 0b1100000000 = 0x300$) in the corresponding word. The writing has to preserve any value in the word for which the mask bit is zero. Once every data field from the XML database has been processed, the resulting array of words is saved into a recipe, that links the words with the name of the register in which the value has to be written. This recipe can then be used to configure the TELL1. All these width check and bit shifting is performed by custom function in the `fwTell1XML.ctl` library.

4.5. Summary

This chapter presented the need of a convenient way to create the TELL1 board recipes, and the chosen implementation was briefly described. The most important TELL1 parameters were presented. The mapping file, which allows to know where the information has to be written, was explained. Finally the PVSS component was presented.

After months of development and debugging, the `fwTell1XML` component is now installed in both IT and TT PVSS projects. After intensive tests, it was proven to be functional, and has been used as the default way to build recipes. This also allows to build recipes while the detector is running, which is a significant improvement compared to the configuration with `cfg` files. The chosen implementation is now proven to be fully justified, as several registers had to be added in the database and mapping files during the development phase, procedure that went smoothly.

Again it has to be said that there are several disconnected way to read or write the XML database. A change in one place *must* be propagated to the other ones, so that everything stays consistent. Apart from correcting possible remaining bugs, keeping the component up to date should be limited to adding / removing registers in the recipe.

Part III.

Inner Tracker studies

Chapter 5.

Efficiency study of the Inner Tracker

5.1. Introduction

At the beginning of June and October 2009, the LHC carried out several synchronisation tests. Runs were taken where a beam of 450 GeV protons extracted from the SPS was dumped on to a beam stopper (the ‘TED’) located 350 m downstream of LHCb. The subsequent spray of particles gave a clear signal in the detector that allowed time and spatial alignment of the IT to be made. It was decided to use these data to measure the efficiency of the sensors in order to check that the IT is behaving as expected. The principles of the processing are explained in this chapter.

Monte Carlo simulations indicate that the majority of the particles traversing the IT in these tests are 10 GeV muons. As can be expected given the nature of the test the environment is quite dirty: the occupancy is very high, the particles have different flight time. Typically 3000 – 4000 IT clusters are observed for each ‘shot’ on the TED, see Figure 5.1 for an example of TED event display. This is twenty times the occupancy expected in the detector during running at a luminosity $2 \cdot 10^{32} \text{ cm}^{-2} \text{ s}^{-1}$. These dataset were used to extract the efficiency of IT readout sectors.

Another TED run occurred in February 2010, which was used as a cross check. A few magnet off collision data from December 2009 were finally used to ensure the validity of the procedure for collision data. The number of events is defined by the number of ‘shots’ on the beam stopper for TED data or by the number of bunch crossings for collision data. The number of events for each data set is given in Table 5.1. The three TED data sets were taken in Time Aligned Mode (TAE), meaning there were 5 triggers sent, separated by one clock cycle (25 ns). The data contain thus 5 subsets, called ‘Spills’.

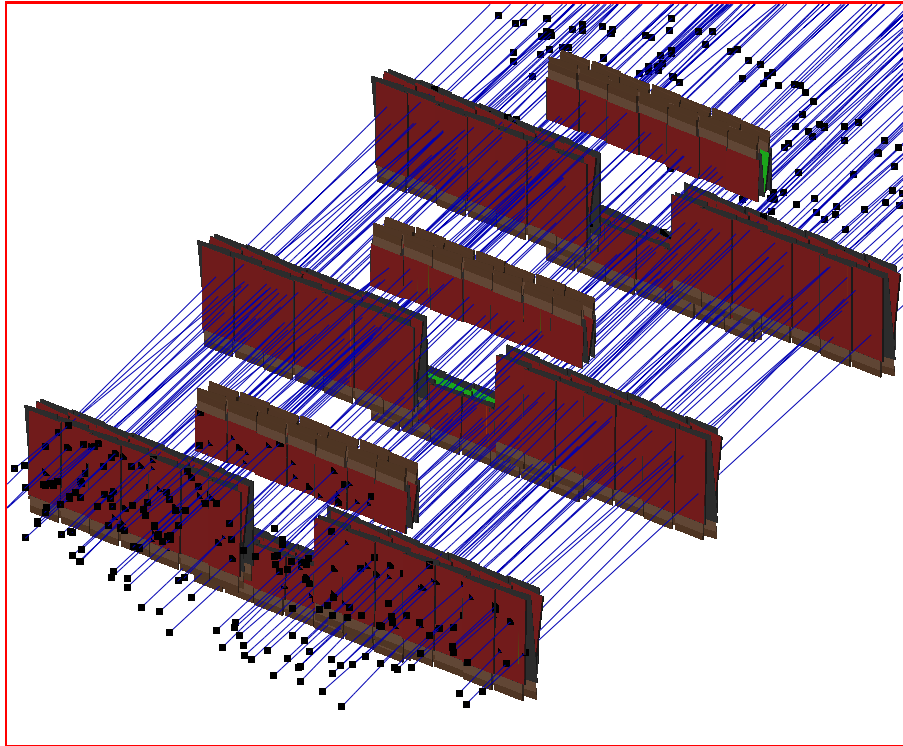


Figure 5.1.: Example of TED event in IT (from October data). The red parts are the sensors, reconstructed tracks are the blue lines.

In the data can be found the spill that triggered the detector and two preceding and following samples.

DATASET	EVENT NUMBER
June 2009's TED	534
October 2009's TED	155
February 2010's TED	715
December 2009's collisions	~ 4200

Table 5.1.: Number of events in the different datasets, used in this analysis.

5.2. Description of the method

The algorithms (described in Section 5.3) dedicated to this study are designed to be used first on TED data. This data sample has two properties which make it different from

normal collision data, namely that there are a very high number of tracks which are almost parallel and come from the muon chambers as opposed to coming from the VELO. However the general idea can also be applied to collision data, with or without magnetic field. The first step is to remove any cluster coming from ‘dead strips’¹. This is needed because the TELL1 processing can create fake clusters from strips that do not send any signal: assuming a dead strip sends a very small signal, it may become smaller than -128 after pedestal and common mode subtraction, which would then be converted into a high positive number. Then the tracks are reconstructed and fitted. The main problem in this study was to reduce the ghost² level as much as possible. In the TED data a tight cut on the track fit χ^2 was applied, and an isolation criteria was used. This latter cut rejected tracks having too many surrounding hits. These data were taken without magnetic field, which results in a huge number of ghost tracks when using the standard pattern recognition, that is why another algorithm, **ITGenericTracking** [23], was used to reconstruct the tracks, which were then fitted with LHCb usual Kalman filter.

For each track, the detector geometry description gives information about which readout sectors should contain a hit. This is performed by the **HitExpectation** [24] tool, which gives a list of readout sectors through which the track travels. To ensure that the track traversed the three IT stations a cut is applied on the expected number of hits. A number of expected hits is obtained for every track. Then the real hits have to be found. A tool is dedicated to cluster finding in any fraction of the IT (stations, boxes, layers³, sectors): **STClusterCollector**. It allows to get all the clusters located at a given distance from the track trajectory: it basically collects all clusters in a cylinder around the track. It is possible that several hits can be found in a readout sector in the chosen window. Therefore, to avoid double counting, only a single hit is considered. Since the efficiency is given by the number of found hits, the choice of the hit does not matter. The efficiency is then defined as the ratio of found hits to expected ones. This efficiency varies with the size of the collection window, as it can be seen on Figure 5.2. From Monte Carlo studies, 10 GeV muons have a resolution of $\sim 80 \mu\text{m}$ for x layers and $\sim 140 \mu\text{m}$ for u and v layers [25]⁴. Based on these typical values, it was decided to compute the efficiency cutting at 0.5 mm for the vertical sectors and 0.7 mm for the

¹Dead strip is the generic name for strips that either do not give meaningful signal or cannot be read. This list contains open strips, shorted pairs and strips suffering from other readout problems.

²A ghost is a track which is reconstructed from random hits, that can be either noise or hits from another real track.

³A layer is a set of seven sectors, lying in the same box and in the same plane: e.g. the x layer.

⁴With their larger effective pitch size due to the stereo angle, the stereo sensors have a lower resolution than the vertical sensors.

stereo ones, corresponding to 5σ of the unbiased residual distribution. Since the counted hits are not excluded from the pattern recognition, the results may be biased. However, studies with the TED data indicate that this bias is at the per mille level and can safely be ignored. This bias could be reduced by excluding the hits from the pattern recognition, running the track reconstruction and fitting the track again. But this requires to run the pattern recognition and track fitting once per readout sector, which is not acceptable in terms of computing time.

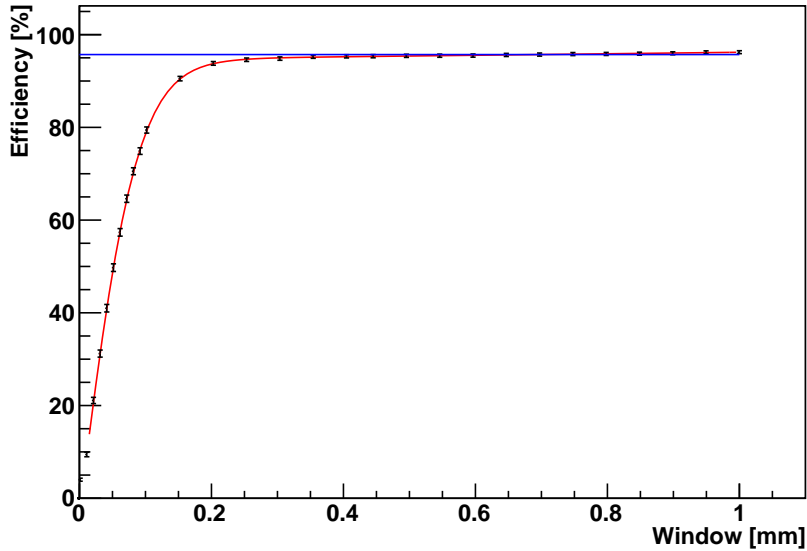


Figure 5.2.: Efficiency vs. window size for IT2CSideU layer. The red curve is a fit to the data points, the blue line indicates the efficiency for a 0.7 mm window, no isolation criteria applied.

The given efficiency values are obtained by choosing a window size. In order to check these values, the following fitting model was used: a Gaussian signal and a flat background are assumed, leading to an error function plus a linear component:

$$\int_0^x e^{-\frac{(y-\mu)^2}{\sigma^2}} + a \, dy \sim \text{erf}(x) + a x \quad (5.1)$$

where x is the collection window size. Figure 5.2 shows that the efficiency curve is well described by Equation (5.1).

5.3. Implementation

As mentioned in Section 5.2, the key feature of the track selection is to select isolated tracks. A dedicated tool was developed (**ITIsolatedTrackSelector**), which is able to get the hits *on* and *around* the track. A cut on the number of found hits is applied to accept or reject the track. The tool uses several instances of **STClusterCollector** and provides a parametrisable interface allowing to set a search window, an absolute number of hits above which the track is rejected and the possibility to set a maximum number of additional hits (i.e. the track is rejected if the total number of surrounding hits is greater than the number of expected ones plus some arbitrary number).

The fitting model from Equation (5.1) was also used to check the validity of the isolation cut: tracks in a clean environment are less prone to be background, leading to a smaller slope in the plateau region of the plot (Figure 5.3).

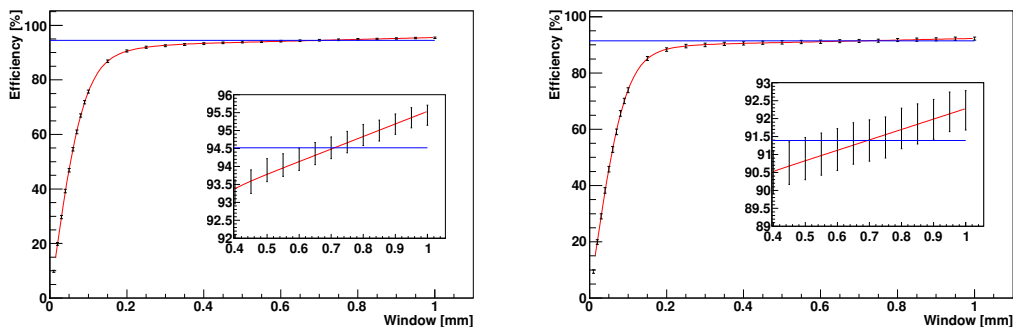


Figure 5.3.: Comparison of efficiency curve without (left) and with (right) isolation criteria applied, for IT2CSideU. A zoom on the plateau region is made to see the difference of slope.

Once the track selection is applied, the data are processed by another specialised algorithm **SEfficiency**, designed to extract efficiency either for IT or TT. This algorithm again uses multiples instances of **STClusterCollector**, and computes efficiency for each readout sector, layer and a ‘mean value’ for the whole detector. The tunable options allow to set the two collection windows (the first one for x layers, the second one for stereo layers), the minimum number of expected hits on a track and the considered track types. An additional cut on the clusters’ charge can be applied, also tunable via **SEfficiency** options. This allows to study the clustering performances versus threshold and spillover.

When the algorithm was designed, the LHCb tracker alignment was not as accurate as it is after one year of data taking. Therefore some inefficiency could arise from hits that would have been expected on the edge of the sensor, where the track passes through the inactive material. This is why an option has been implemented which allows hits near the edge of any sensor to be ignored. An exclusion region is then built with a tunable width. Another feature that used to be was a tunable exclusion width around $y = 0$: the two-sensor readout sectors are made of two sensors, with a gap between them. In their *local* reference frame, the gap should be at $y = 0$.

5.4. Results

The algorithm computes the efficiency of all readout sectors and layers: curves such as those presented on Figure 5.2 and Figure 5.3 are produced for each of these. A view of the whole detector is also produced, which summarises the readout sector efficiencies. It also allows to easily correlate low efficiency values with known other problems (like misalignment). Such a plot is shown on Figure 5.4. The relevant statistical indication is not the number of events, but the number of selected tracks, given on Table 5.2. Since the uncertainty depends on the number of expected and found hits, the precision increases with the number of selected tracks. Each TED event containing up to a hundred tracks, the achieved precision is better than the collision data, in which a few tracks per events are selected, despite a much higher number of events.

DATASET	NBR OF SELECTED TRACKS
June 2009's TED	24'500
October 2009's TED	7'500
February 2010's TED	31'500
December 2009's collisions	8'500

Table 5.2.: Number of selected tracks for each used data set. Note that TED events have on average around 45 selected tracks per events, whilst the collision data have on average 2 selected tracks per event.

5.4.1. Detector efficiency

In general x layers have a higher efficiency than u and v layers. This is caused by worse alignment of the stereo layers. The effect of the alignment quality is also seen on external sectors (i.e. sectors 1 and 7). Efficiencies are not 100% (Figure 5.4) for two reasons. First, in the TED runs the ghost rate is up to 5.4%⁵ [23]. Therefore, there is a non negligible chance that fake tracks are selected for this study. Monte Carlo studies indicate that this reduce the measured efficiency by 1%. The second reason is the non optimal alignment. Its effect has not been quantified but is expected to explain a majority of the remaining inefficiency. A piece of evidence about non optimal alignment is the fact that the efficiency of the readout sectors increases as the hit exclusion region grows, this was tested with a y band exclusion width up to 10 mm. This was diagnosed as a scarce knowledge of the y position of the readout sectors, for the gap design position is at $y = 0$

⁵This value is obtained ignoring the isolation criteria.

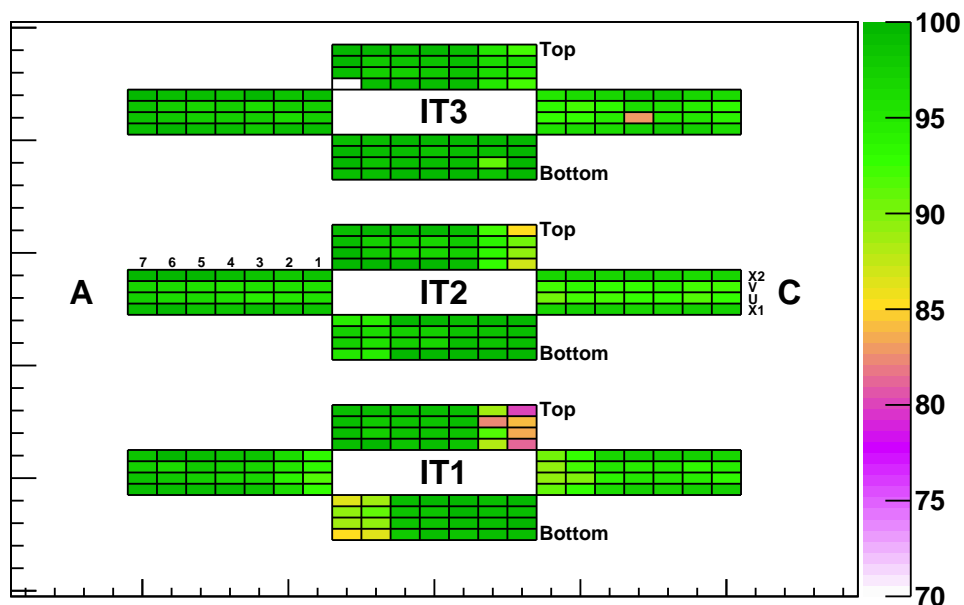


Figure 5.4.: Efficiencies from June 2009's TED run. One sector is disabled (IT3TopX1Sector7), one sector appearing in orange (IT3CryoSector4) is known to have a large common mode noise, decreasing the efficiency. The alignment effect can clearly be seen, for instance in the first station, sectors 6 and 7 in all layers of the Bottom box have an efficiency below 95%, the same is seen for the Top box, sectors 1 and 2 in all layers.

in the local reference frame. Any deviation should in principle be corrected for by the alignment, however the increase of efficiency with the exclusion growing shows that the spread of the corrected vertical position of the gap is of the order of 1 cm.

The obtained efficiencies are given on Table 5.3. The presented values have an exclusion region of 2 mm (both in x and y), this shows a systematic increase of the efficiency value for collision data with respect to TED data. This shift is consistent with the 1% inefficiency due to ghost rate, according to Monte Carlo studies. Apart from Table 5.3, all the presented results were obtained with June 2009's data. More detailed results can be found in [26].

DATASET	DETECTOR EFF.	LAYER EFF.		SECTOR EFF.	
		Mean	RMS	Mean	RMS
June 2009's TED	97.62 ± 0.02 %	97.71 %	1.41 %	97.59 %	3.67 %
October 2009's TED	97.47 ± 0.05 %	97.56 %	2.05 %	97.00 %	4.83 %
February 2010's TED	97.14 ± 0.04 %	97.22 %	3.37 %	97.28 %	5.98 %
December 2009's collisions	98.29 ± 0.04 %	98.32 %	1.19 %	98.21 %	2.00 %

Table 5.3.: Summary of efficiency values. The detector efficiency is obtained by considering the whole detector as one element. Mean and RMS values are given for layers and sectors: they come from the histograms having one entry per layer (sector).

5.4.2. Spillover efficiency

The 40 MHz nominal crossing rate of the LHC together with the behaviour of the front-end shaper (see Figure 5.5) means that in normal running there is a non-negligible chance to detect particles from crossing prior to the trigger. This is called *spillover*.

STEfficiency can also be used to study spillover efficiency. As mentioned in Section 5.1 the TED data were taken in TAE mode. If the clusters are searched in the sample 25 ns after the triggered event, the obtained efficiencies are a measurement of the spillover efficiency. Here the cut on the cluster charge can be used to study the spillover dependence on the confirmation threshold⁶.

The layer efficiency plot clearly shows two populations (see Figure 5.6). This is expected, since there are long ladders (two sensors sectors) in the Access and Cryo

⁶The confirmation threshold used here is the same as the confirmation threshold defined in Section 3.2.4.

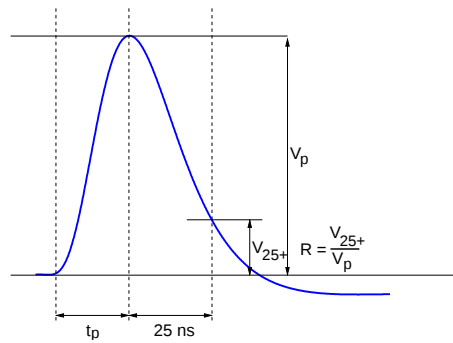


Figure 5.5.: Beetle pulse shape, from the beetle manual [13]. The pulse shape is characterised by the peaking time t_p , the peaking voltage V_p and the remainder R , defined as the ratio between the signal voltage after 25 ns (V_{25+}) and V_p .

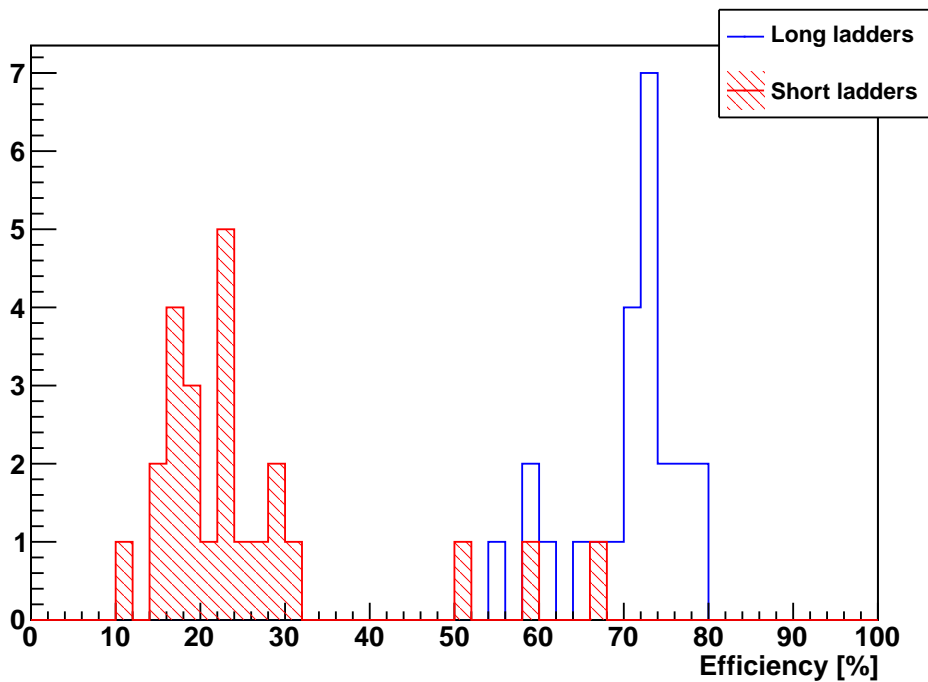


Figure 5.6.: Layer spillover efficiencies, in blue are the long ladders, in red (and hatched) are the short ones.

boxes and short ones (one sensor sectors) in the Top and Bottom boxes. These different lengths give different capacitance, which cause different remainder. The long ladders are expected to have more spillover. A small subset of the short ladders are thicker than the other ones: the long ladders are mainly composed of $320 \mu\text{m}$ thick ladders, but some of them are $410 \mu\text{m}$ thick. The latter has a larger signal than the former, but the relative signal fraction (i.e. remainder) is the same, which means a higher absolute fraction hence

a higher spillover efficiency. On Figure 5.6 can be seen the three layers containing short thick ladders.

5.4.3. Efficiency vs. confirmation threshold

The **STEfficiency** class can apply an additional cut on the cluster charge as mentioned in Section 5.3. This allows to study the efficiency versus the confirmation threshold.

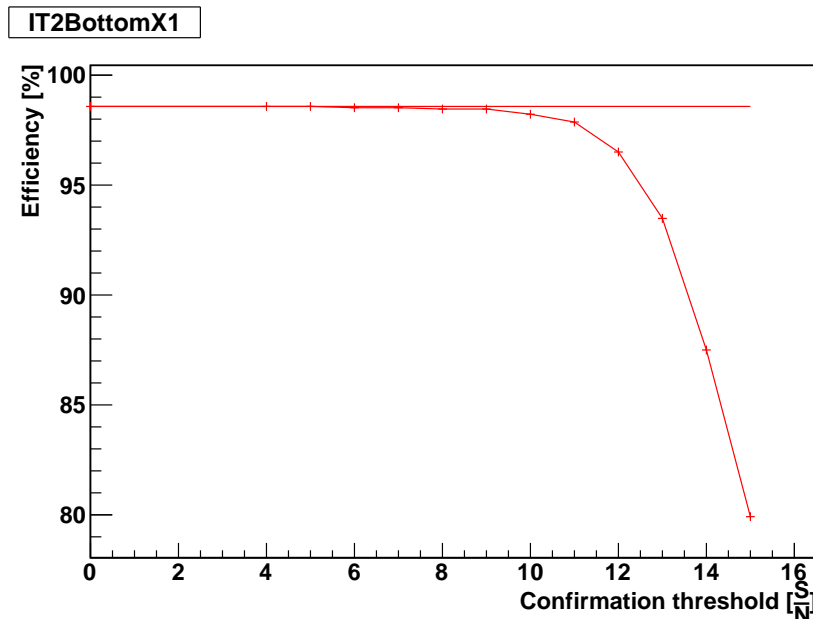


Figure 5.7.: Efficiency vs confirmation threshold, **IT2BottomX1**. The horizontal line is the quoted value.

As shown on Figure 5.7, the efficiency is almost constant for a signal to noise ratio of nine, and then starts to drop. This indicates that we could in principle put a higher confirmation threshold (present value is 4), allowing to reject more spillover. Unfortunately this is not the case for all the layers. For instance **IT3CSideU** contains the sector that developed a HV problem between June and October 2009 and is now disabled, on Figure 5.8 it can be seen that this layer efficiency is much more sensitive to the threshold: it starts dropping at six, this could be due to a poorer depletion. On the plots shown on Figure 5.7 and Figure 5.8 the confirmation threshold goes from four (the cut applied online) to fifteen. Since the TELL1 board only deals with integer values (ADCs and thresholds) and **STEfficiency** uses floating point values, there could be discrepancies when the online cut value (i.e. a signal to noise ratio of 4) is used within **STEfficiency**. This is why a point at $\frac{S}{N} = 0$ is computed as well.

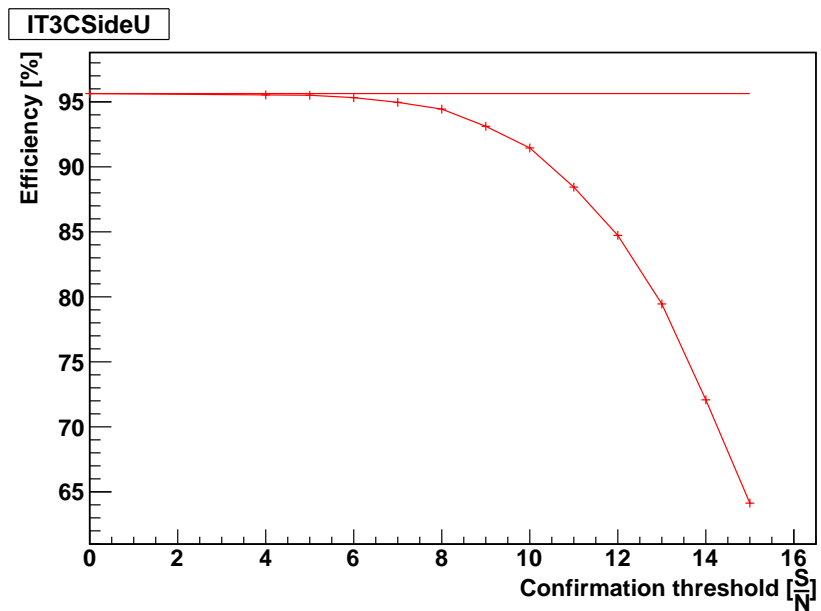


Figure 5.8.: Efficiency vs confirmation threshold, **IT3CSideU**. The efficiency drops earlier (6 instead of 10) and more rapidly ($\sim 64\%$ instead of $\sim 80\%$ at $\frac{S}{N} = 15$) than **IT2BottomX1** in Figure 5.4. The horizontal line is the quoted value.

5.4.4. Spillover efficiency vs. confirmation threshold

The evolution of the spillover efficiency with the confirmation threshold has also been studied. As expected the spillover efficiency falls more steeply as the confirmation threshold is increased. Figure 5.9 (Figure 5.10) shows an example for a typical short (long) layer. As mentioned in Section 5.4.2, the long ladders have a larger remainder because of the increased capacitance. This combined to the increased thickness is the reason why the spillover efficiency is higher for long ladders.

Putting a higher confirmation threshold, the chosen example here is 5, makes the long and short ladders closer in terms of efficiency, as can be seen on the layer spillover efficiency plot on Figure 5.11 (that should be compared to Figure 5.6).

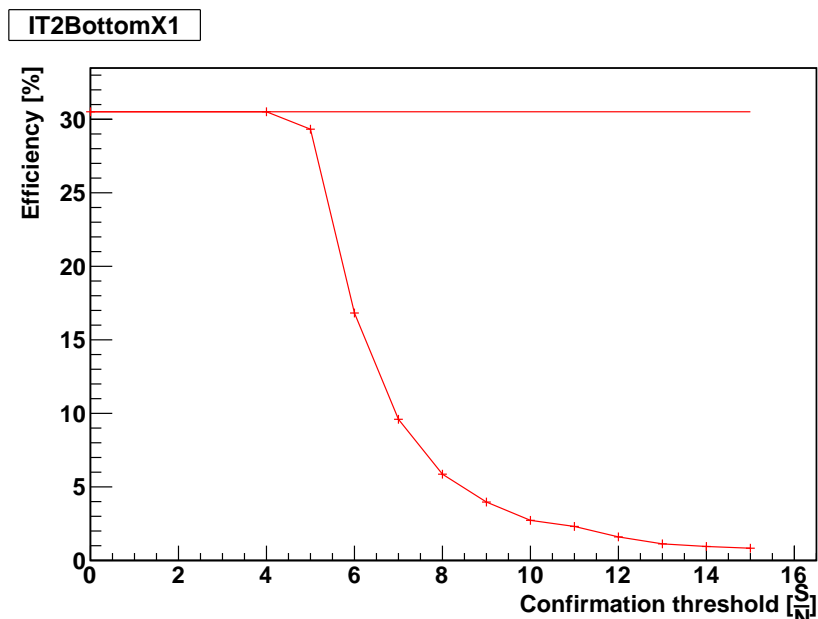


Figure 5.9.: Efficiency for spillover vs confirmation threshold, **IT2BottomX1**. The horizontal line is the quoted value.

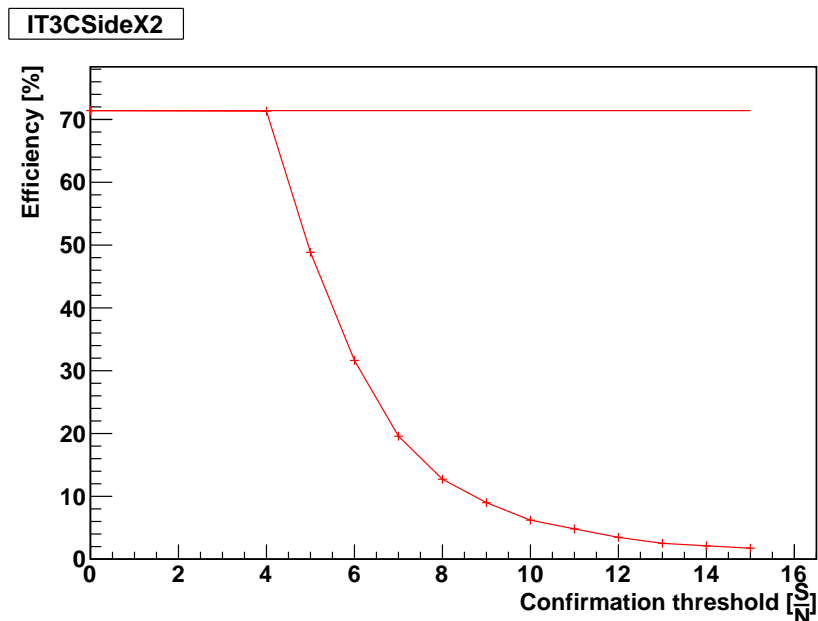


Figure 5.10.: Efficiency for spillover vs confirmation threshold, IT3CSideX2. The horizontal line is the quoted value.

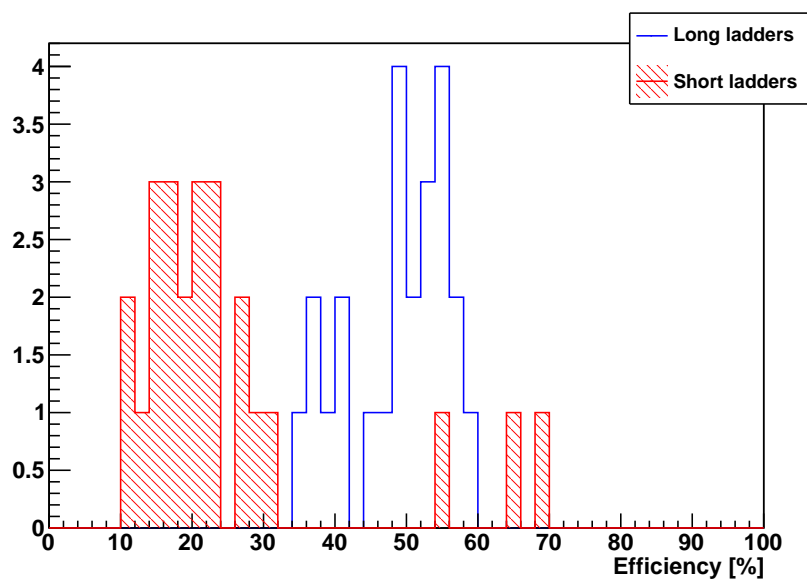


Figure 5.11.: Layer spillover efficiencies, in blue are the long ladders, in red (and hatched) are the short ones. A cut at 5 is applied on the clusters signal to noise ratio.

5.5. Summary

This chapter presented a method to extract the IT efficiency. This method can in principle be applied to TT. It has been shown that the efficiency values are sensitive to alignment precision and can thus be used to cross-check the validity of the alignment constants. The studies has also allowed some problematic areas of the detector to be identified. The obtained results will improve with the high statistics and cleaner environment available in collision data taking.

Spillover has been studied, the efficiency for spillover cluster finding has been measured to be 70.5 % and 24.5 % (means of the sector's efficiencies) for the long and short ladders respectively with the threshold of 4 in terms of $\frac{S}{N}$. The spillover efficiency shows a clear dependence on the thickness of the sensor.

Study of efficiency versus the confirmation threshold has shown that there is no strong dependence in the interval [4, 9] (in terms of $\frac{S}{N}$). However the known faulty sectors do have a stronger dependence. From these results it is concluded that it is possible to use a confirmation threshold of $\sim 5 \frac{S}{N}$. The mean of the sectors' efficiency decreases only by 0.02 %, whilst the spill over efficiency decreases from 24.5 % to 23.6 % for short ladders and from 70.5 % to 47.7 % for the long ladders. Based on this the 2010 configuration has the confirmation threshold set to $5 \frac{S}{N}$. From the track reconstruction point of view, this spillover efficiency of almost 50% is not a problem, even for the future 25 ns running: the TELL1 board tags the created clusters using the SpillOver threshold, currently set to 10 (in terms of $\frac{S}{N}$), allowing to discriminate online clusters which are likely to be spillover.

Part IV.

Lifetime and lifetime ratio measurements

Chapter 6.

Theoretical introduction

The theory of elementary particles is called the *Standard Model*, which is based on a relativistic quantum field theory. It results from the combination of the *Standard Model of electro-weak interactions* [27–29] and *Quantum Chromodynamics* (QCD). The Standard Model is a very successful theory: at present its predictions are consistent with experiments. However some questions remain unanswered by the Standard Model: for instance the origin of the neutrino mass, mixing and electro-weak symmetry breaking.

Section 6.1 discusses the Standard Model and fundamental symmetries, then in Section 6.2 is presented the B-mesons time evolution. Finally in Section 6.3 are discussed the motivation for measuring the B-mesons lifetimes and lifetime ratios.

6.1. The Standard Model and discrete symmetries

The Standard Model is a gauge theory based on the $SU(3)_C \otimes SU(2)_L \otimes U(1)_Y$ group, describing the strong, weak and electromagnetic interactions. These interactions are mediated by gauge bosons: 8 gluons and 1 photon, all massless, for the strong and electromagnetic interaction respectively, and 3 massive bosons (W^\pm and Z^0) for the weak interaction. Strong interactions are described by the $SU(3)_C$ and the C index stands for the colour charge, whilst $SU(2)_L \otimes U(1)_Y$ is the unified description of the electro-weak interactions where the L index stands for left-handed and the Y one for the hypercharge.

In particle physics some discrete symmetries have a significant relevance, they are described here below by their effect on the quantum state $|\psi(\vec{p}, h)\rangle$ of a particle with momentum \vec{p} and helicity $h = \vec{s} \cdot \hat{p}$, \vec{s} being the particle spin and \hat{p} the direction of propagation.

- Particle - antiparticle exchange, described by the charge conjugation operator \mathcal{C} :

$$\mathcal{C}|\psi(\vec{p}, h)\rangle = \eta_C|\bar{\psi}(\vec{p}, h)\rangle$$

- Spatial inversion, described by the parity operator \mathcal{P} :

$$\mathcal{P}|\psi(\vec{p}, h)\rangle = \eta_P|\psi(-\vec{p}, h)\rangle$$

- Time reversal, described by operator \mathcal{T} :

$$\mathcal{T}|\psi(\vec{p}, h)\rangle = \eta_T|\psi(-\vec{p}, h)\rangle^*$$

η_C is a phase factor, η_P is the intrinsic parity of the particle and η_T is another phase factor depending on the spin.

The Hamiltonian describing strong and electromagnetic interactions is invariant under \mathcal{C} , \mathcal{P} and \mathcal{T} transformation and under any combination of them. However observations show violation of the parity and charge conjugation in weak interactions. This is also seen when studying the combined symmetry \mathcal{CP} .

The combination of those three symmetries, \mathcal{CPT} , however has been checked to always be conserved. Without \mathcal{CPT} conservation the quantum field theory cannot be built. Selected consequences of \mathcal{CPT} conservation are the fact that the mass and the lifetime of a particle and its anti-particle are equal, as demonstrated in Section 6.2.1.

6.2. B-mesons time development

6.2.1. Phenomenology

The studied B-mesons in this analysis are B^+ , B^0 and B_s^0 , which quark content is $\bar{b}u$, $\bar{b}d$ and $\bar{b}s$ respectively, their antiparticle are B^- , \bar{B}^0 and \bar{B}_s^0 , which quark content is $b\bar{u}$, $b\bar{d}$ and $b\bar{s}$.

The following paragraph, inspired by [30], recalls some basics on B-mesons time evolution. The $|B_q\rangle$ and $|\bar{B}_q\rangle$ states are eigenstates of strong (\mathcal{H}_s), electromagnetic (\mathcal{H}_{em}) interaction and the flavour (\mathcal{F}). They represent the particles B_q and \bar{B}_q (with $q = u, d$,

s) at rest.

$$\begin{aligned}
(\mathcal{H}_s + \mathcal{H}_{em})|B_q\rangle &= m_q|B_q\rangle \\
(\mathcal{H}_s + \mathcal{H}_{em})|\bar{B}_q\rangle &= \bar{m}_q|\bar{B}_q\rangle \\
\mathcal{F}|B_q\rangle &= +|B_q\rangle \\
\mathcal{F}|\bar{B}_q\rangle &= -|\bar{B}_q\rangle
\end{aligned}$$

The \mathcal{CP} transformation links these two states:

$$\mathcal{CP}|B_q\rangle = \eta_{CP}|\bar{B}_q\rangle \qquad \mathcal{CP}|\bar{B}_q\rangle = \eta_{CP}^*|B_q\rangle \qquad (6.1)$$

where ξ is an arbitrary phase. And \mathcal{T} acts as:

$$\mathcal{T}|B_q\rangle = \eta_T|B_q\rangle \qquad \mathcal{T}|\bar{B}_q\rangle = \bar{\eta}_T|\bar{B}_q\rangle \qquad (6.2)$$

If the strong and electromagnetic interactions conserve \mathcal{CPT} (which is always assumed):

$$\overrightarrow{(\mathcal{CPT})}(\mathcal{H}_s + \mathcal{H}_{em})\overrightarrow{(\mathcal{CPT})}^\dagger = \mathcal{H}_s + \mathcal{H}_{em} \qquad (6.3)$$

then the the mass of the particle is equal to the mass of its anti-particle:

$$\begin{aligned}
m_q &= \langle B_q | \mathcal{H}_s + \mathcal{H}_{em} | B_q \rangle \\
&= \langle B_q | \overrightarrow{(\mathcal{CPT})}^\dagger \overrightarrow{(\mathcal{CPT})} (\mathcal{H}_s + \mathcal{H}_{em}) \overrightarrow{(\mathcal{CPT})}^\dagger \overrightarrow{(\mathcal{CPT})} | B_q \rangle \\
&= \langle B_q | \overrightarrow{(\mathcal{CPT})}^\dagger (\mathcal{H}_s + \mathcal{H}_{em}) \overrightarrow{(\mathcal{CPT})} | B_q \rangle \\
&= \langle B_q | \overleftarrow{(\mathcal{CPT})}^\dagger (\mathcal{H}_s + \mathcal{H}_{em}) \overrightarrow{(\mathcal{CPT})} | B_q \rangle^* \\
&= \langle \bar{B}_q | \mathcal{H}_s + \mathcal{H}_{em} | \bar{B}_q \rangle \\
&= \bar{m}_q
\end{aligned} \qquad (6.4)$$

At $t = 0$ only strong and electromagnetic interaction are involved, then for $t > 0$ the weak interaction (\mathcal{H}_w) comes into play and the B_q (\bar{B}_q) starts to decay, into a $|f\rangle$ final state, eigenstate of the strong and electromagnetic interactions:

$$(\mathcal{H}_s + \mathcal{H}_{em})|f\rangle = E_f|f\rangle$$

The general state $|\Psi(t)\rangle = a(t)|\mathbb{B}_q\rangle + b(t)|\overline{\mathbb{B}}_q\rangle + \sum_f c_f(t)|f\rangle$ is obtained by solving the Schrödinger equation:

$$i\frac{\partial}{\partial t}|\Psi(t)\rangle = (\mathcal{H}_s + \mathcal{H}_{em} + \mathcal{H}_w)|\Psi(t)\rangle \quad (6.5)$$

where $|a(t)|^2 + |b(t)|^2 + \sum_f |c_f(t)|^2 = 1$. Introducing the Dirac representation operators and wave function:

$$\begin{aligned} |\Psi(t)\rangle &= e^{-i(\mathcal{H}_s + \mathcal{H}_{em})t} |\Psi(t)\rangle_D \\ V(t) &= e^{i(\mathcal{H}_s + \mathcal{H}_{em})t} |\Psi(t)\rangle \mathcal{H}_w e^{-i(\mathcal{H}_s + \mathcal{H}_{em})t} \end{aligned}$$

Equation (6.5) reads:

$$i\frac{\partial}{\partial t}|\Psi(t)\rangle_D = V(t)|\Psi(t)\rangle_D \quad (6.6)$$

Operating $\langle\mathbb{B}_q|$, $\langle\overline{\mathbb{B}}_q|$ or $\langle f|$ from the left and using the Wigner-Weisskopf approximation (i.e. neglecting $\langle f|\mathcal{H}_w|f'\rangle$) the equation describing the time evolution of $a(t)$ and $b(t)$ reads:

$$i\frac{\partial}{\partial t} \begin{pmatrix} a(t) \\ b(t) \end{pmatrix} = \mathbf{\Lambda} \begin{pmatrix} a(t) \\ b(t) \end{pmatrix} \quad (6.7)$$

where $\mathbf{\Lambda}$ is given by

$$\mathbf{\Lambda} = \mathbf{M} + \frac{i}{2}\mathbf{\Gamma}, \quad (6.8)$$

\mathbf{M} and $\mathbf{\Gamma}$ are 2×2 hermitian matrices, but $\mathbf{\Lambda}$ is not hermitian, i.e. $|a(t)|^2 + |b(t)|^2 \neq 1$. The mass matrix elements are:

$$\mathbf{M}_{11} = m_q + \langle\mathbb{B}_q|\mathcal{H}_w|\mathbb{B}_q\rangle + \sum_f \mathbf{P} \left(\frac{\langle\mathbb{B}_q|\mathcal{H}_w|f\rangle \langle f|\mathcal{H}_w|\mathbb{B}_q\rangle}{m_0 - E_f} \right) \quad (6.9)$$

$$\mathbf{M}_{22} = m_q + \langle\overline{\mathbb{B}}_q|\mathcal{H}_w|\overline{\mathbb{B}}_q\rangle + \sum_f \mathbf{P} \left(\frac{\langle\overline{\mathbb{B}}_q|\mathcal{H}_w|f\rangle \langle f|\mathcal{H}_w|\overline{\mathbb{B}}_q\rangle}{m_0 - E_f} \right) \quad (6.10)$$

$$\mathbf{M}_{12} = \langle\mathbb{B}_q|\mathcal{H}_w|\overline{\mathbb{B}}_q\rangle + \sum_f \mathbf{P} \left(\frac{\langle\mathbb{B}_q|\mathcal{H}_w|f\rangle \langle f|\mathcal{H}_w|\overline{\mathbb{B}}_q\rangle}{m_0 - E_f} \right) \quad (6.11)$$

where $|f\rangle$ are real and virtual possible final states for B_q and \bar{B}_q , and E_f is the energy of the final state. The decay matrix elements are:

$$\Gamma_{11} = 2\pi \sum_f |\langle B_q | \mathcal{H}_w | f \rangle|^2 \delta(m_0 - E_f) \quad (6.12)$$

$$\Gamma_{22} = 2\pi \sum_f |\langle \bar{B}_q | \mathcal{H}_w | f \rangle|^2 \delta(m_0 - E_f) \quad (6.13)$$

$$\Gamma_{12} = 2\pi \sum_f \langle B_q | \mathcal{H}_w | f \rangle \langle f | \mathcal{H}_w | \bar{B}_q \rangle \delta(m_0 - E_f) \quad (6.14)$$

where $|f\rangle$ are real final states, common to B_q and \bar{B}_q . The invariance of \mathcal{H}_w under \mathcal{CPT} implies that:

$$\begin{aligned} \mathbf{M}_{11} &= m_q + \langle B_q | \mathcal{H}_w | B_q \rangle + \sum_f \mathbf{P} \left(\frac{\langle B_q | \mathcal{H}_w | f \rangle \langle f | \mathcal{H}_w | B_q \rangle}{m_0 - E_f} \right) \\ &= m_q + \langle B_q | \overrightarrow{(\mathcal{CPT})}^\dagger \mathcal{H}_w \overrightarrow{(\mathcal{CPT})} | B_q \rangle \\ &+ \sum_f \mathbf{P} \left(\frac{\langle B_q | \overrightarrow{(\mathcal{CPT})}^\dagger \mathcal{H}_w \overrightarrow{(\mathcal{CPT})} | f \rangle \langle f | \overrightarrow{(\mathcal{CPT})}^\dagger \mathcal{H}_w \overrightarrow{(\mathcal{CPT})} | B_q \rangle}{m_0 - E_f} \right) \\ &= m_q + \langle \bar{B}_q | \mathcal{H}_w | \bar{B}_q \rangle + \sum_f \mathbf{P} \left(\frac{\langle \bar{B}_q | \mathcal{H}_w | f \rangle \langle f | \mathcal{H}_w | \bar{B}_q \rangle}{m_0 - E_f} \right) \\ &= \mathbf{M}_{22} \end{aligned} \quad (6.15)$$

and

$$\begin{aligned} \Gamma_{11} &= 2\pi \sum_f |\langle B_q | \mathcal{H}_w | f \rangle|^2 \delta(m_0 - E_f) \\ &= 2\pi \sum_f \left| \langle B_q | \overrightarrow{(\mathcal{CPT})}^\dagger \mathcal{H}_w \overrightarrow{(\mathcal{CPT})} | f \rangle \right|^2 \delta(m_0 - E_f) \\ &= 2\pi \sum_f |\langle f | \mathcal{H}_w | \bar{B}_q \rangle|^2 \delta(m_0 - E_f) \\ &= \Gamma_{22} \end{aligned} \quad (6.16)$$

In the case of charged particles (i.e. B^+ and B^-), $\mathbf{M}_{12} = \mathbf{M}_{21} = 0$ and $\Gamma_{12} = \Gamma_{21} = 0$ and $\mathbf{\Lambda}$ is therefore diagonal, because there are no common final states. The solution of Equation (6.7) is two decaying exponential with the *same* lifetime (since $\Gamma_{11} = \Gamma_{22}$).

For neutral particles (i.e. $B^0-\bar{B}^0$ and $B_s^0-\bar{B}_s^0$), oscillations are allowed, since there are final states $|f\rangle$ common to both B_q and \bar{B}_q (from now onwards $q = d, s$). The effective Hamiltonian $\mathbf{\Lambda}$ is no longer diagonal, and there are two mass eigenstates:

$$|B_L\rangle = p|B_q\rangle + q|\bar{B}_q\rangle \quad (6.17)$$

$$|B_H\rangle = p|B_q\rangle - q|\bar{B}_q\rangle \quad (6.18)$$

called *light* and *heavy*. They have a mass $m_L < m_H$ and width $\Gamma_H < \Gamma_L$ in the Standard Model. The complex coefficients p and q are such that $|p|^2 + |q|^2 = 1$. The eigenvalues of \mathbf{M} and $\mathbf{\Gamma}$ define the mass difference Δm_q and the width difference $\Delta\Gamma_q$:

$$\Delta m_q = M_{Hq} - M_{Lq} \quad \Delta\Gamma_q = \Gamma_{Lq} - \Gamma_{Hq} \quad (6.19)$$

The average mass and width read:

$$M_{B_q} = \frac{M_{Hq} + M_{Lq}}{2} \quad \Gamma_q = \frac{\Gamma_{Lq} + \Gamma_{Hq}}{2} \quad (6.20)$$

The effective Hamiltonian $\mathbf{\Gamma}$ allows to link the values of Δm_q , $\Delta\Gamma_q$ and $\frac{p}{q}$ to the matrix elements M_{12} and Γ_{12} , and defines the time evolution of the B_q and \bar{B}_q mesons.

The instantaneous decay amplitudes are defined:

$$A_f = \langle f | \mathcal{H}_w | B_q \rangle \quad \bar{A}_{\bar{f}} = \langle \bar{f} | \mathcal{H}_w | \bar{B}_q \rangle \quad (6.21)$$

$$\bar{A}_f = \langle \bar{f} | \mathcal{H}_w | B_q \rangle \quad A_{\bar{f}} = \langle f | \mathcal{H}_w | \bar{B}_q \rangle \quad (6.22)$$

The most general expression of the proper time distribution has four expressions, expressing the decay rate of the B_q (\bar{B}_q) into the final state f (or \bar{f}) [30]:

$$\begin{aligned} \Gamma(B_q(t) \rightarrow f) &= \frac{|A_f|^2}{2} e^{-\Gamma_q t} (g_+(t) + g_-(t)) \\ \Gamma(\bar{B}_q(t) \rightarrow f) &= \frac{|A_f|^2}{2} \left| \frac{p}{q} \right|^2 e^{-\Gamma_q t} (g_+(t) - g_-(t)) \\ \Gamma(B_q(t) \rightarrow \bar{f}) &= \frac{|\bar{A}_{\bar{f}}|^2}{2} e^{-\Gamma_q t} (\bar{g}_+(t) + \bar{g}_-(t)) \\ \Gamma(\bar{B}_q(t) \rightarrow \bar{f}) &= \frac{|\bar{A}_{\bar{f}}|^2}{2} \left| \frac{q}{p} \right|^2 e^{-\Gamma_q t} (\bar{g}_+(t) + \bar{g}_-(t)) \end{aligned} \quad (6.23)$$

the time dependent parts, where the (+) and (−) indices indicates that the flavour conservation (+) or change (−), are defined as:

$$g_+(t) = (1 + |\lambda_f|^2) \cosh\left(\frac{1}{2} \Delta\Gamma_q t\right) - 2 \Re\{\lambda_f\} \sinh(\Delta m_q t) \quad (6.24)$$

$$g_-(t) = (1 - |\lambda_f|^2) \cos(\Delta m_q t) - 2 \Im\{\lambda_f\} \sin(\Delta m_q t) \quad (6.25)$$

$$\bar{g}_+(t) = \left(1 + |\bar{\lambda}_f|^2\right) \cosh\left(\frac{1}{2} \Delta\Gamma_q t\right) - 2 \Re\{\bar{\lambda}_f\} \sinh(\Delta m_q t) \quad (6.26)$$

$$\bar{g}_-(t) = \left(1 - |\bar{\lambda}_f|^2\right) \cos(\Delta m_q t) - 2 \Im\{\bar{\lambda}_f\} \sin(\Delta m_q t) \quad (6.27)$$

with the two complex quantities have been defined:

$$\lambda_f = \frac{q \bar{A}_f}{p A_f} \quad \bar{\lambda}_f = \frac{p A_{\bar{f}}}{q \bar{A}_{\bar{f}}} \quad (6.28)$$

For a flavour specific decay, i.e. when B_q can only decay to f and \bar{B}_q to \bar{f} , Equations (6.24) to (6.27) can be simplified. The proper time distribution is made even simpler when there is no initial tag (i.e. when initial B_q and \bar{B}_q are not distinguished), it reads:

$$\Gamma\left((B_q + \bar{B}_q)(t) \rightarrow f\right) \propto e^{-\Gamma_q t} \cosh\left(\frac{1}{2} \Delta\Gamma_q t\right) \quad (6.29)$$

with an initial tag (i.e. the initial flavour of the B-meson is known), Equation (6.29) reads:

$$\begin{aligned} \Gamma(B_q(t) \rightarrow f) &\propto e^{-\Gamma_q t} \left(\cosh\left(\frac{1}{2} \Delta\Gamma_q t\right) + \cos(\Delta m_q t) \right) \\ \Gamma(B_q(t) \rightarrow \bar{f}) &\propto e^{-\Gamma_q t} \left(\cosh\left(\frac{1}{2} \Delta\Gamma_q t\right) - \cos(\Delta m_q t) \right) \end{aligned} \quad (6.30)$$

For flavour non-specific decays, i.e. when both B_q and \bar{B}_q can decay into f , the untagged proper time distribution is:

$$\Gamma(B_q(t) \rightarrow f) \propto e^{-\Gamma_q t} \left((1 + |\lambda_f|^2) \cosh\left(\frac{1}{2} \Delta\Gamma_q t\right) + 2 \Re\{\lambda_f\} \sinh\left(\frac{1}{2} \Delta\Gamma_q t\right) \right) \quad (6.31)$$

whilst the tagged proper time distribution reads:

$$\begin{aligned} \Gamma(B_q(t) \rightarrow f) &\propto e^{-\Gamma_q t} \left((1 + |\lambda_f|^2) \cosh\left(\frac{1}{2} \Delta\Gamma_q t\right) + 2 \Re\{\lambda_f\} \sinh\left(\frac{1}{2} \Delta\Gamma_q t\right) \right. \\ &\quad \left. - 2 \Im\{\lambda_f\} \sin(\Delta m_q t) \right) \end{aligned} \quad (6.32)$$

6.2.2. Relevant proper time distribution

In this study the proper time distributions are modelled by a single exponential, as in Equation (6.33). It is exact for B^\pm , which is charged and cannot oscillate. For B^0 , the decay of interest is flavour specific, there is no initial tag, but $\Delta\Gamma_d$ is measured to be almost 0, so Equation (6.29) reads again like Equation (6.33). B_s^0 has a non-zero width difference, but it is small and the measurement of the width requires initial tag to be extracted, this is why the same proper time distribution function is used.

$$\Gamma(B_q(t) \rightarrow f) \propto e^{-\frac{t}{\tau_{B_q}}} \quad (6.33)$$

6.3. Motivations

6.3.1. Indirect searches for new physics

The $B_s^0 \rightarrow J/\psi(1S) (\mu^+ \mu^-) \phi (K^+ K^-)$ decay is one of the golden channels to observe new physics in the B_s^0 system. A \mathcal{CP} violating phase, called ϕ_s arises due to interference between decay amplitudes with or without oscillation (ϕ_s is closely related to the phase of the parameter λ_f mentioned in Section 6.2.1). In the Standard Model this phase is equal to $-2\beta_s = -0.036$ rad [31], but can be dramatically increased in presence of new physics. The decay width difference ($\Delta\Gamma_s$) in B_s^0 system has also some sensitivity to new physics. Previous measurement of ϕ_s from CDF and $D\phi$ experiments are not accurate enough to tightly constrain these parameters [32]. LHCb was able to measure $\phi_s \in [-2.7, -0.5]$ rad at 68% confidence level [33] already using the same data set as in this study.

Extracting ϕ_s from the $B_s^0 \rightarrow J/\psi(1S) \phi$ decay requires a flavour tagged time-dependent analysis. For this complicated analysis, the flavour tagging algorithms have to be calibrated and tuned to achieve optimal performances and to have a good estimate of the mistag fraction. The proper time resolution and acceptance also need to be well understood. Monte Carlo simulation gives some information. However it is known that an analysis cannot rely on simulation only. This is why it is chosen to study several $b \rightarrow J/\psi(1S) X$ (X standing for K , K^{*0} or ϕ) decays, with a similar trigger and selection, in order to use them as control channel for $B_s^0 \rightarrow J/\psi(1S) \phi$. The proper time calibration and the flavour tagging optimisation and calibration use data from $B^+ \rightarrow J/\psi(1S) K^+$ and $B^0 \rightarrow J/\psi(1S) K^{*0}$.

6.3.2. Test of \mathcal{CPT}

The lifetimes can also be used to test \mathcal{CPT} symmetry, which is the fundamental symmetry in quantum field theory and therefore in the Standard Model. As described in Section 6.2.1, the \mathcal{CPT} symmetry forces the lifetime and mass of the particle and its anti-particle to be the same. It has been thoroughly tested many times, and no indication of violation has been seen so far. Since it is such a fundamental question, it should be kept testing as much as possible. The B lifetime measurements done in this study allow to perform this test in the B-meson system. For B^+ / B^- there is no major difficulty, but for B^0 / \bar{B}^0 and B_s^0 / \bar{B}_s^0 , the measurement is much harder. Since the neutral B-mesons can oscillate to their antiparticle and no tagging information is used in this study, their flavour is deduced from the final state. $B^0 \rightarrow J/\psi(1S) K^{*0}$ is flavour specific, but a B^0 oscillating to \bar{B}^0 before its decay will be reconstructed as \bar{B}^0 and therefore wrongly taken into account in the ratio. The fraction of B^0 (\bar{B}^0) oscillating before decay is $18.63 \pm 0.023\%$ [34]. In the $B_s^0 \rightarrow J/\psi(1S) \phi$ case, it is even worse: the final state is not flavour specific, and therefore 50%¹ of the reconstructed B_s^0 are actually \bar{B}_s^0 . In this study a \mathcal{CPT} test is made with B^+ / B^- only.

6.3.3. Heavy quark expansion theory

The Heavy Quark Effective Theory (HQET) [35] is a theory which describes the phenomenology of QCD involving heavy quarks. In this model, the heavy quark is assumed to be at rest and to be the source of the gluon field. The typical corrections are $\mathcal{O}\left(\frac{1}{m}\right)$, where m is the mass of the heavy quark. In this approximation, mesons are the QCD equivalent of the hydrogen atom.

HQET can for instance predict the masses of b-hadrons and B-mesons lifetimes. This is why precise measurements of B-mesons lifetimes are important. Using HQET the following lifetime ratios can be predicted [36]:

$$\frac{\tau(B^-)}{\tau(B^0)} = 1 + \mathcal{O}\left(\frac{\Lambda_{\text{QCD}}}{m_b^3}\right) \quad (6.34)$$

$$\frac{\tau(B_s^0)}{\tau(B^0)} = (1.00 \pm 0.01) + \mathcal{O}\left(\frac{\Lambda_{\text{QCD}}}{m_b^3}\right) \quad (6.35)$$

¹Assuming no production asymmetry.

where m_b is the mass of the b quark and $\Lambda_{\text{QCD}} \simeq 200$ MeV the QCD energy scale. Unknown $SU(3)$ -violating effects are responsible for the error on the $\tau(B_s^0)/\tau(B^0)$ ratio [36]. These predictions assume the spectator quark has no influence on the lifetime. But there are two effects which cause the lifetime of the charged meson (B^\pm) to be larger than the neutral (B^0): destructive interference, called ‘Pauli interference’, and differences in the non-spectator diagrams, involving V_{ub} and V_{cb} for B^\pm and B^0 respectively [37]. More recent predictions [38] give the ratios following ratios:

$$\frac{\tau(B^\pm)}{\tau(B^0)} = 1.06 \pm 0.02 \quad (6.36)$$

$$\frac{\tau(B_s^0)}{\tau(B^0)} = 1.00 \pm 0.01 \quad (6.37)$$

Present results [39] on B-mesons lifetimes and lifetime ratios are summarised in Table 6.1 and Table 6.2 respectively. It should be noted that the measured τ_{B^\pm}/τ_{B^0} ratio from Table 6.2 is compatible with the prediction from Equation (6.36), whilst the $\tau_{B_s^0}/\tau_{B^0}$ is marginally compatible with Equation (6.37).

PARTICLE	LIFETIME [ps]
B^\pm	1.641 ± 0.008
B^0	1.516 ± 0.007
B_s^0	$1.477^{+0.021}_{-0.022}$

Table 6.1.: B-meson lifetimes. Note that the B_s^0 lifetime is defined here as Γ_s^{-1} , and cannot be compared to the value we extract from our fit (this will be developed in Chapter 10), from [39].

LIFETIME RATIO	MEASURED VALUE
τ_{B^\pm}/τ_{B^0}	1.081 ± 0.006
$\tau_{B_s^0}/\tau_{B^0}$	0.973 ± 0.015

Table 6.2.: B-meson lifetime ratios. Again, note that the $\tau_{B_s^0}/\tau_{B^0}$ ratio uses Γ_s^{-1} as the value of the B_s^0 lifetime, fom [39].

Chapter 7.

Used data sets

7.1. Data samples

During LHC first year of data taking at $\sqrt{s} = 7$ TeV (2010), LHCb recorded approximately 37 pb^{-1} of data. This data set was used to measure ϕ_s [33]. The data has been reconstructed with BRUNEL [40] v37r8p4 and stripped with DAVINCI [41] v26r3 (Reco08-Stripping12) using the DIRAC [42] production management system. The stripping is a procedure that extracts from the global data set events with a specific signature, for instance the presence of a dimuon. This allows to reduce the size of the data set which has to be used for an analysis. When the small data sets (called stripped data) are produced, the candidates are reconstructed and saved. In this study each considered channel has a dedicated ‘stripping line’, all of them starting from a reconstructed J/ψ . ROOT [43] ntuples were then produced from an additional offline selection step, starting from the B-mesons candidates reconstructed at the stripping level. The fitting to extract the lifetimes and lifetime ratios was performed on these ntuples.

7.2. Monte Carlo samples

The study of the $B^+ \rightarrow J/\psi(1S) K^+$, $B^0 \rightarrow J/\psi(1S) K^{*0}$ and $B_s^0 \rightarrow J/\psi(1S) \phi$ channels used the latest “MC10” Monte Carlo data, which were generated with an average number of p p interactions per bunch crossing $\nu = 2.5$. The parameter ν is related to the mean number of visible interactions¹ per bunch crossing in the LHC (μ), and it is assumed that $\mu = 0.699 \nu$. This value of ν was chosen to correspond to the condition of the majority

¹The number of visible interaction is the number of reconstructed p p interactions.

of events collected by LHCb during 2010. The samples were generated by the LHCb collaboration at the beginning of 2011, using GAUSS v39r0 and BRUNEL v37r8p5. The generation parameters, such as cross sections, lifetimes, beam energy, etc., were tuned to be as close as possible to the running condition, and the reconstruction algorithms, triggers and trigger emulations were very similar to the ones used on collected data. For the three decay modes $B^+ \rightarrow J/\psi(1S) K^+$, $B^0 \rightarrow J/\psi(1S) K^{*0}$ and $B_s^0 \rightarrow J/\psi(1S) \phi$, event were generated with two different configuration of the spectrometer dipole magnet field: one is the field points upward (Up) and the other reversed (Down). The number of generated events is given in Table 7.1.

SAMPLE	DOWN POLARITY	UP POLARITY
$B^+ \rightarrow J/\psi(1S) K^+$	1.0	1.0
$B^0 \rightarrow J/\psi(1S) K^{*0}$	1.2	5.2
$B_s^0 \rightarrow J/\psi(1S) \phi$	1.0	1.0

Table 7.1.: Number of events for each Monte Carlo sample (given in millions of events), for the up and down polarities.

Chapter 8.

Triggers

The LHCb triggers are split into three levels, called Level 0, High Level Trigger 1 and 2. An overview with the corresponding output rates is presented on Figure 8.1, the output rates are taken from [44].

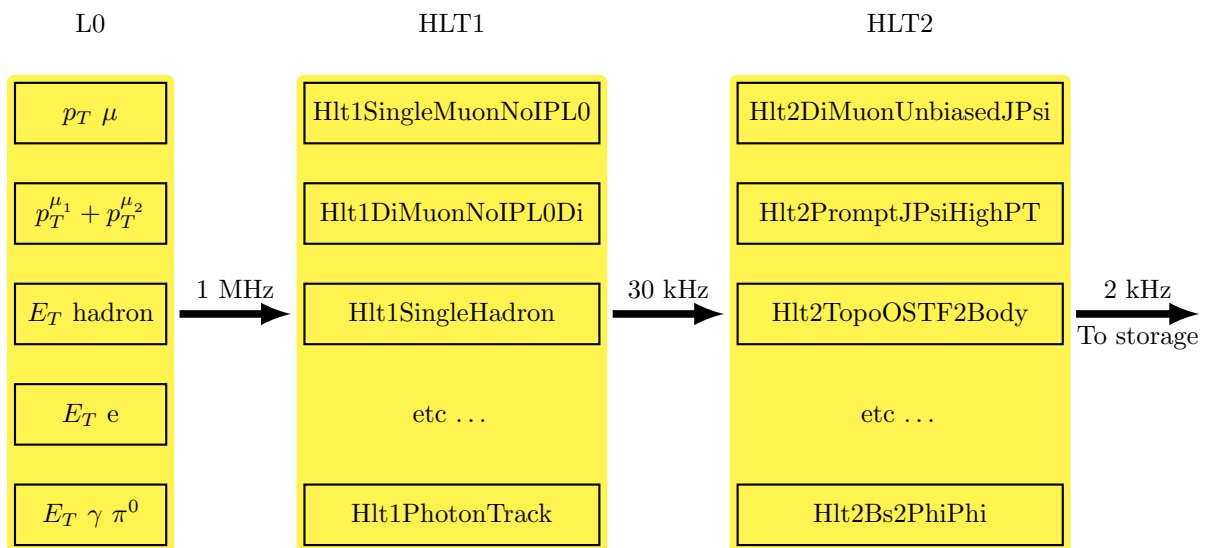


Figure 8.1.: Triggers flowchart. The list of L0 triggers corresponds to all physics L0 triggers, whilst for HLT1 and HLT2 only small subsets are shown.

8.1. Hardware Trigger

The nominal bunch crossing rate of 40 MHz is too high for reading out the full detector, this is why this rate is reduced to 1 MHz by a hardware trigger, called Level-0 (L0). The L0 main inputs are the calorimeter and muon triggers. Since the studied B-meson

decays contain muons in the final state, only L0-muon triggers are used. There are two of them : the single-muon line, looking for at least one muon candidate with hits in all muon stations and a transverse momentum (p_T) above threshold, and the dimuon line, looking the two highest p_T muons with a summed p_T above threshold.

8.2. High Level Trigger

The events accepted by L0-muon triggers are processed by the High Level Trigger (HLT), divided into Hlt1 and Hlt2. The HLT is a software trigger, running on a large CPU farm. Both Hlt1 and Hlt2 contain trigger lines causing a proper time bias, i.e. no cuts are applied on quantities which introduces a distortion of the proper time distribution, such as the impact parameter¹ or the separation of the J/ψ vertex and the primary vertex, and trigger lines which do not. In this study only the non-biasing lines are considered. The former are called lifetime unbiased trigger lines and the latter lifetime biased trigger lines. The lifetime unbiased Hlt1 lines must confirm the L0 decision, checking whether a track can be reconstructed from the hits in the tracking system, using the L0 object (which can be an electron, a muon or a hadron) as seed, then cuts on p_T and on the momentum (p) are applied. A Hlt1 accepted event is then fully reconstructed in Hlt2, using algorithms as close as possible to the ones used during offline reconstruction, and a set of inclusive and exclusive selections is applied.

8.3. Selected trigger lines

In this analysis only a few trigger lines are taken into account. This simplifies the computation of efficiencies and proper time acceptance studies. The lines of interest are again muon lines.

The Hlt1 line with highest efficiency for $b \rightarrow J/\psi(1S) X$ signal is the single muon line without impact parameter cut (Hlt1SingleMuonNoIPL0). Starting from the L0 object, it tries to reconstruct a track from hits in the tracking stations. Any found seed is matched to the L0 object, combined and then matched to a reconstructed VELO track. This last two operations mean that the muon track segment (reconstructed from hits in the muon system) is associated to a track segment in the tracking stations, and then the obtained

¹The impact parameter is defined for a particle with respect a the primary vertex: it is the distance of closest approach of the particle trajectory to the primary vertex.

track is associated to a VELO track. The other line used in this analysis is the dimuon line starting from a L0 dimuon (Hlt1DiMuonNoIPL0Di). The tracks are reconstructed and fitted in the same way, but instead of a cut on the tracks p_T , a cut on the sum of the p_T of the two muons is applied. The distance of closest approach (DOCA) of the two tracks is used to determine whether the two muons are coming from the same point of origin.

The used Hlt2 line is the lifetime unbiased J/ψ line (Hlt2DiMuonUnbiasedJPsi). For events passing Hlt1, the tracks are fitted and the combinations are selected based on their mass and the χ^2 of the formed vertex.

Only events categorised as TOS (trigger on signal) are used in this study. This means that the signal B candidate caused the trigger to accept the event, more precisely either one or the two muons. The TOS requirement is made at Hlt1 and Hlt2 stage.

Chapter 9.

Event Selection

Once the reconstruction is done, several candidates per event are reconstructed, and for such rare decays (see Table 9.1 for the relevant cross sections for the $B^+ \rightarrow J/\psi(1S) K^+$, $B^0 \rightarrow J/\psi(1S) K^{*0}$ and $B_s^0 \rightarrow J/\psi(1S) \phi$ decay modes) most of these candidates are background. The selection needs therefore to increase the final sample purity (i.e. proportion of signal events) by rejecting background. This procedure is often a trade-off between purity and efficiency. In this chapter the two selections used in this analysis are presented. The different steps of the signal selection are presented in Sections 9.1 to 9.4. Selections efficiencies are shown in Section 9.5 and signal yields on data are presented in Section 9.6.

9.1. Selection strategy

The strategy used to select events, used together with the lifetime unbiased trigger lines described in Chapter 8, is meant to select B candidates without distortion of the proper time distributions. This strategy also selects a huge component of prompt background, peaking at $t \simeq 0$, which is understood to be combinations of tracks from the PV. However this background harms neither the lifetime nor the \mathcal{CP} asymmetry measurements, since the large proper time region is clean. The presented results are obtained with two different selections, the first optimised to maximise the sensitivity on ϕ_s , and described in [45]. The second, developed by me, was meant to minimise the proper time bias, by cutting as little as possible on kinematics variable but tightening the particle ID and vertex quality cuts to reject background. From now onwards, the first selection will be referred to as the ‘standard’ (or std.) selection, the second one as the ‘alternative’ (or alt.) selection.

BRANCHING FRACTION	PDG	MC10
$\mathcal{BR}(J/\psi(1S) \rightarrow \mu^+ \mu^-)$	$(5.93 \pm 0.06) \cdot 10^{-2}$	$5.930 \cdot 10^{-2}$
$\mathcal{BR}(K^{*0} \rightarrow K^+ \pi^-)$	2/3	$66.57 \cdot 10^{-2}$
$\mathcal{BR}(\phi \rightarrow K^+ K^-)$	$(48.9 \pm 0.5) \cdot 10^{-2}$	$49.20 \cdot 10^{-2}$
$\mathcal{BR}(B^+ \rightarrow J/\psi(1S) K^+)$	$(1.013 \pm 0.034) \cdot 10^{-3}$	$1.008 \cdot 10^{-3}$
$\mathcal{BR}(B^0 \rightarrow J/\psi(1S) K^{*0})$	$(1.33 \pm 0.06) \cdot 10^{-3}$	$1.330 \cdot 10^{-3}$
$\mathcal{BR}(B_s^0 \rightarrow J/\psi(1S) \phi)$	$(1.4 \pm 0.5) \cdot 10^{-3}$	$1.35 \cdot 10^{-3}$
$\mathcal{BR}_{\text{vis}}(B^+ \rightarrow J/\psi(1S) (\mu^+ \mu^-) K^+)$	$(6.01 \pm 0.21) \cdot 10^{-5}$	$5.98 \cdot 10^{-5}$
$\mathcal{BR}_{\text{vis}}(B^0 \rightarrow J/\psi(1S) (\mu^+ \mu^-) K^{*0} (K^+ \pi^-))$	$(5.25 \pm 0.24) \cdot 10^{-5}$	$5.25 \cdot 10^{-5}$
$\mathcal{BR}_{\text{vis}}(B_s^0 \rightarrow J/\psi(1S) (\mu^+ \mu^-) \phi (K^+ K^-))$	$(4.1 \pm 1.4) \cdot 10^{-5}$	$3.94 \cdot 10^{-5}$
f_u [%]	40.3 ± 1.1	41
f_d [%]	40.3 ± 1.1	41
f_s [%]	11.0 ± 1.2	10.5

Table 9.1.: Branching fraction for all decays and B-meson production fractions. Values from PDG [34] and from the Monte Carlo simulation are indicated.

The main difference between the two selections is that the kinematical cuts for the alt. selection are mostly the same as for the stripping, and that cuts on χ^2 variables are tuned such that the fit probabilities are equal in the three channels¹.

9.2. Stripping and offline selections

The stripping, as mentioned in Section 7.1, is designed to reconstruct the three channels $B^+ \rightarrow J/\psi(1S) K^+$, $B^0 \rightarrow J/\psi(1S) K^{*0}$ and $B_s^0 \rightarrow J/\psi(1S) \phi$ using lifetime unbiased cuts. This is performed after the full reconstruction, reducing the needed bandwidth and the size of the dataset to acceptable values.

Once the decay is fully reconstructed, a kinematic decay tree fitter [46] is used. This tool performs a fit on the whole decay tree, using constraints derived from physics to improve the experimental resolution. This kinematic decay tree fitter allows to put mass constraints on any particle in the tree, i.e. the fit will try to get the particle's mass as close as possible to its nominal value. Another constraint can also be used: the candidate can be required to come from a given PV, allowing the flight distance of the particle

¹Since the number of degrees of freedom varies from one decay to the other, a constant cut on $\chi^2/n\text{DoF}$ does not result in the same probability to reject signal events.

to be extracted. Two important quantities are obtained from the kinematic decay tree fitter: the mass of the B candidate using a J/ψ mass constrain and no constraint on the PV and the B proper time is computed with a constraint on the PV, but no J/ψ mass constraint. The former fit allows to improve the resolution on the B mass, whilst the latter fit improves the decay length resolution without introducing correlations between the background proper time and mass distributions.

A final selection is applied offline to enhance the dataset purity. A brief description of these stripping lines is given below, a more complete one can be found in [45].

9.2.1. $J/\psi(1S) \rightarrow \mu^+\mu^-$ selection

The cuts applied for J/ψ selection in the stripping and offline analysis are summarised in Table 9.2. The ‘Stripping value’ column shows the values of the cut at the stripping level, and are thus applied to each reconstructed J/ψ candidate. The selected J/ψ candidates have then their mass constrained to the PDG value ($M(J/\psi) = 3096.916$ MeV) before any other processing. The ‘Std. value’ is the value of the cut for the ϕ_s sensitivity optimised selection, and the ‘Alt. value’ is the value of the cut for the alternative selection. The muon candidates are selected by track quality ($\chi^2_{\text{track}}/\text{nDoF}(\mu)$ is the reduced χ^2 of the track fit), separation from the pion hypothesis ($\Delta \ln \mathcal{L}(\mu/\pi)$) and p_T . Cuts on the χ^2 of the $(\mu^+ - \mu^-)$ vertex ($\chi^2_{\text{vtx}}(J/\psi)$) and on the J/ψ candidate reconstructed mass ($M_{\text{reco}}(J/\psi)$) are applied.

CUT	STRIPPING VALUE	STD. VALUE	ALT. VALUE
$\chi^2_{\text{track}}/\text{nDoF}(\mu)$	< 5	< 4	< 5
$\Delta \ln \mathcal{L}(\mu/\pi)$	> 0	> 0	–
$\Delta \ln \mathcal{L}(\mu/e)$	–	–	> 4
$p_T(\mu)$	–	> 500 MeV/c	> 500 MeV/c
$\chi^2_{\text{vtx}}(J/\psi)$	< 16	< 11	< 10
$ M_{\text{reco}}(J/\psi) - M(J/\psi) $	80 MeV/c ²	80 MeV/c ²	80 MeV/c ²
$ M_{\text{reco}}(J/\psi) - M(J/\psi) /\sigma_{M_{J/\psi}}$	–	< 1.4 · 3	–

Table 9.2.: $J/\psi(1S) \rightarrow \mu^+\mu^-$ selection. A ‘–’ indicates that no such cut was applied for the corresponding selection step. The reconstructed J/ψ at the stripping level is used for all the exclusive $B \rightarrow J/\psi(1S) X$ lines. The std. and alt. values are the values of the cut used offline to enrich the sample for the two selections.

In the std. selection, an additional cut is applied on the J/ψ mass pull. In the std. selection the muons are additionally required to be separated from the electron hypothesis by applying an additional cut on $\Delta \ln \mathcal{L}(\mu/e)$.

9.2.2. $B^+ \rightarrow J/\psi(1S) K^+$ selection

The selection for $B^+ \rightarrow J/\psi(1S) K^+$ is described here and summarised in Table 9.3. In the alt. selection, the p cut from the std. selection is replaced by asking a much better separation from the pion and proton hypothesis, cutting on $\Delta \ln \mathcal{L}(K/\pi)$ and $\Delta \ln \mathcal{L}(K/p)$. The cut for the χ^2 value in the vertex fit with $(\mu^+ - \mu^- - K)$ ($\chi_{\text{vtx}}^2/\text{nDoF}(B)$) corresponds to a fit probability greater than $1.4 \cdot 10^{-6}$ (i.e. $\chi^2/\text{nDoF} < 10$ with 3 degrees of freedom). This value of the fit probability will be used to get the cut value for the χ^2 in the B vertex fit for the other channels. Cuts on the K track quality $\chi_{\text{track}}^2/\text{nDoF}(K)$ and on the track p_T are applied. The mass window is $5139 \leq M_{\text{reco}}(B^\pm) \leq 5419 \text{ MeV}/c^2$. In the std. selection, a cut on the χ^2 of the determination of the IP wrt the PV ($\chi_{\text{IP}}^2/\text{nDoF}(B)$) is applied.

CUT	STRIPPING VALUE	STD. VALUE	ALT. VALUE
$\Delta \ln \mathcal{L}(K/\pi)$	> -2	> 0	> 3
$\Delta \ln \mathcal{L}(K/p)$	–	> -2	> 1
$\chi_{\text{track}}^2/\text{nDoF}(K)$	< 5	< 4	< 5
$p_T(K)$	$> 1 \text{ GeV}/c$	$> 1 \text{ GeV}/c$	$> 1 \text{ GeV}/c$
$p(K)$	–	$> 10 \text{ GeV}/c$	–
$M(B)$	$\in [5100, 5550] \text{ MeV}/c^2$	$\in [5100, 5450] \text{ MeV}/c^2$	$\in [5139, 5419] \text{ MeV}/c^2$
$\chi_{\text{vtx}}^2/\text{nDoF}(B)$	< 10	< 10	< 10
$\chi_{\text{IP}}^2/\text{nDoF}(B)$	–	< 5	–
$\chi_{\text{DTF}}^2/\text{nDoF}(B)$	–	< 5	< 5

Table 9.3.: $B^+ \rightarrow J/\psi(1S) K^+$ selection. A ‘–’ indicates that no such cut was applied for the corresponding selection step. The std. and alt. values are the values of the cut used offline to enrich the sample for the two selections.

In both cases, a cut on the kinematic decay tree fit quality, fit performed with no constraint on the J/ψ mass and a constraint on the PV, is applied ($\chi_{\text{DTF}}^2/\text{nDoF}(B)$).

9.2.3. $B^0 \rightarrow J/\psi(1S) K^{*0}$ selection

The selection for $B^0 \rightarrow J/\psi(1S) K^{*0}$ is described here and summarised in Table 9.4. Cuts on the pion and kaon track quality ($\chi_{\text{track}}^2/\text{nDoF}(K, \pi)$), on the kaon PID ($\Delta \ln \mathcal{L}(K/\pi)$ and $\Delta \ln \mathcal{L}(K/p)$), on $K^{*0} p_T$ and reconstructed mass $M_{\text{reco}}(K^{*0})$ are applied. A cut on the $B^0 p_T$ is applied at the stripping level to reduce the data sample size and the needed bandwidth. A cut on the kinematic decay tree fit quality is applied ($\chi_{\text{DTF}}^2/\text{nDoF}$). The main differences between the std. and alt. selections are the PID cuts on the pion, asking for a separation from the kaon and electron hypothesis ($\Delta \ln \mathcal{L}(\pi/K)$ and $\Delta \ln \mathcal{L}(\pi/e)$).

CUT	STRIPPING VALUE	STD. VALUE	ALT. VALUE
$\Delta \ln \mathcal{L}(K/\pi)$	> -2	> 0	> 3
$\Delta \ln \mathcal{L}(K/p)$	–	> -2	> -5
$\chi_{\text{track}}^2/\text{nDoF}(K, \pi)$	< 5	< 4	< 5
$\Delta \ln \mathcal{L}(\pi/K)$	–	–	> -5
$\Delta \ln \mathcal{L}(\pi/e)$	–	–	> 0
$p_T(K^{*0})$	$> 1 \text{ GeV}/c$	$> 1 \text{ GeV}/c$	$> 1 \text{ GeV}/c$
$ M_{\text{reco}}(K^{*0}) - M(K^{*0}) $	$< 90 \text{ MeV}/c^2$	$< 70 \text{ MeV}/c^2$	$< 90 \text{ MeV}/c^2$
$\chi_{\text{vtx}}^2/\text{nDoF}(K^{*0})$	< 16	< 16	< 10
$M(B^0)$	$\in [5100, 5550] \text{ MeV}/c^2$	$\in [5100, 5450] \text{ MeV}/c^2$	$\in [5139, 5419] \text{ MeV}/c^2$
$p_T(B^0)$	$> 2 \text{ GeV}/c$	$> 2 \text{ GeV}/c$	$> 2 \text{ GeV}/c$
$\chi_{\text{vtx}}^2/\text{nDoF}(B^0)$	< 10	< 10	< 7
$\chi_{\text{DTF}}^2/\text{nDoF}$	–	< 5	< 5
$\chi_{\text{IP}}^2/\text{nDoF}(B^0)$	–	< 25	–

Table 9.4.: $B^0 \rightarrow J/\psi(1S) K^{*0}$ selection. A ‘–’ indicates that no such cut was applied for the corresponding selection step. The std. and alt. values are the values of the cut used offline to enrich the sample for the two selections.

In the alt. selection, the vertex fit of $(K^+ - \pi^-)$ forming the K^{*0} the cut value for $\chi_{\text{vtx}}^2/\text{nDoF}$ is identical to that applied for the J/ψ vertex reconstruction, while the $\chi_{\text{vtx}}^2/\text{nDoF}(B^0)$ one corresponds to the same fit probability as for the B^+ . The mass window is $5139 \leq M_{\text{reco}}(B^0) \leq 5419 \text{ MeV}/c^2$.

An additional cut is used in the std. selection on the χ^2 of the IP determination of the B^0 wrt its PV ($\chi_{\text{IP}}^2/\text{nDoF}$).

9.2.4. $B_s^0 \rightarrow J/\psi(1S) \phi$ selection

The selection for $B_s^0 \rightarrow J/\psi(1S) \phi$ is described here and summarised in Table 9.5. Cuts on the kaon track quality ($\chi_{\text{track}}^2/\text{nDoF}$), kaon PID ($\Delta \ln \mathcal{L}(K/\pi)$), ϕ p_T and reconstructed mass $M_{\text{reco}}(\phi)$ are applied, as well as a cut on the kinematic decay tree fit quality ($\chi_{\text{DTF}}^2/\text{nDoF}$). The main differences between the std. and alt. selections are the in PID cuts on the kaon, asking for a separation from the proton hypothesis and the size of the ϕ mass window.

In the alt. selection, the vertex fit of $(K^+ - K^-)$ forming the ϕ cut value for $\chi_{\text{vtx}}^2/\text{nDoF}$ is the same to that applied for the J/ψ vertex fit. The $\chi_{\text{vtx}}^2/\text{nDoF}(B_s^0)$ cut value corresponds to the same fit probability as for the B^\pm and B^0 . The mass window is $5226 \leq M_{\text{reco}}(B_s^0) \leq 5506 \text{ MeV}/c^2$.

For the std. selection, a cut on the the χ^2 of the IP determination is additionally applied.

CUT	STRIPPING VALUE	STD. VALUE	ALT. VALUE
$\Delta \ln \mathcal{L}(K/\pi)$	> -2	> 0	> 3
$\Delta \ln \mathcal{L}(K/p)$	–	–	> -5
$\chi_{\text{track}}^2/\text{nDoF}(K)$	< 5	< 4	< 5
$p_T(\phi)$	$> 1 \text{ GeV}/c$	$> 1 \text{ GeV}/c$	$> 1 \text{ GeV}/c$
$M(\phi)$	$\in [980, 1050] \text{ MeV}/c^2$	$\in [1008, 1032] \text{ MeV}/c^2$	$\in [990, 1050] \text{ MeV}/c^2$
$\chi_{\text{vtx}}^2/\text{nDoF}(\phi)$	< 16	< 16	< 10
$M(B_s^0)$	$\in [5100, 5550] \text{ MeV}/c^2$	$\in [5200, 5550] \text{ MeV}/c^2$	$\in [5226, 5506] \text{ MeV}/c^2$
$\chi_{\text{vtx}}^2/\text{nDoF}(B_s^0)$	< 10	< 10	< 7
$\chi_{\text{DTF}}^2/\text{nDoF}(B_s^0)$	–	< 5	< 5
$\chi_{\text{IP}}^2/\text{nDoF}(B_s^0)$	–	< 25	–

Table 9.5.: $B_s^0 \rightarrow J/\psi(1S) \phi$ selection. A ‘–’ indicates that no such cut was applied for the corresponding selection step. The std. and alt. values are the values of the cut used offline to enrich the sample for the two selections.

9.3. Cleaning the negative proper time tail

It was first observed [45] that the selected events have a proper time distribution with a large negative tail. Part of it is known to come from the proper time resolution, but this

cannot explain all. The tail of the distribution is events where the signal is associated to the wrong primary vertex. In order to reduce this effect the selections (both std. and alt.) require that the B candidate is *not* compatible with the second best PV, when multiple PVs are present in an event. This is achieved by requiring the χ^2_{IP} of the second best to be more than 50. As shown in Figure 9.1, the events rejected by this additional cut have a peaked flight distance distribution, which tends to be more symmetric than the distribution of accepted events. For [45] a bug was present in the computation of this χ^2 : the vertices were not refitted when the IP and χ^2 were computed. As a consequence, tracks used to reconstruct the candidate could be taken into account when fitting the vertices, which could result in a value of the IP which is too low. This bug was corrected for the results presented in this study.

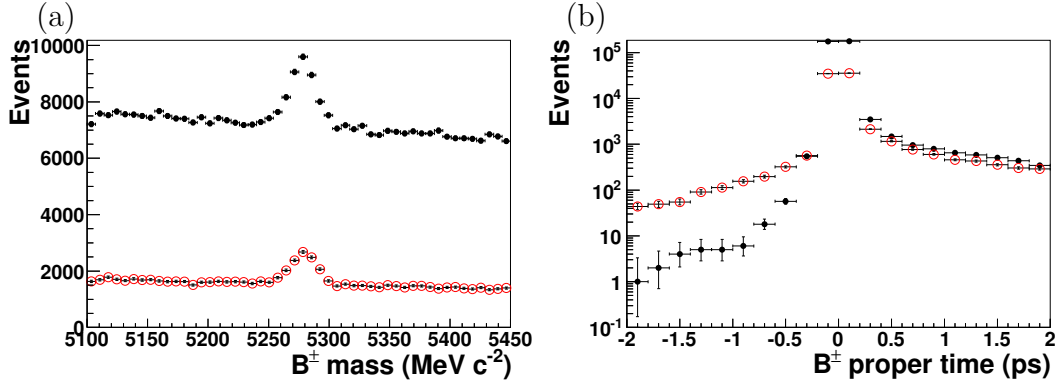


Figure 9.1.: Mass (a) and proper time (b) distributions of events rejected (red circles) and accepted (black points) by the cut on χ^2_{IP} of the second best PV. B^\pm candidate passing the std. selection are shown.

9.4. Best candidate selection

Once the whole selection procedure is applied, there are still some events containing more than one selected candidate. The numbers are given in Table 9.6 for $B^+ \rightarrow J/\psi(1S) K^+$, $B^0 \rightarrow J/\psi(1S) K^{*0}$ and $B_s^0 \rightarrow J/\psi(1S) \phi$.

When multiple candidates are present, the one with the best kinematic decay tree fit quality (i.e. with lowest $\chi^2_{\text{D,TF}}/\text{nDoF}$) is chosen and all the other candidates are dropped. This results in only one B candidate per event used for measurements. The B candidate mass distribution of rejected events is flat, as seen in Figure 9.2. Studies have shown that the dropped candidates are mainly clones, sharing the same J/ψ , which allows to safely ignore them.

CHANNEL	STD. SELECTION	ALT. SELECTION
$B^+ \rightarrow J/\psi(1S) K^+$	1.07	1.05
$B^0 \rightarrow J/\psi(1S) K^{*0}$	1.45	1.34
$B_s^0 \rightarrow J/\psi(1S) \phi$	1.09	1.12

Table 9.6.: Number of candidates per event passing the offline selections. The proper time range is $[-2, 14]$ ps. The B mass ranges are $[5150, 5400]$ MeV/c^2 (B^\pm), $[5150, 5400]$ MeV/c^2 (B^0) and $[5200, 5550]$ MeV/c^2 (B_s^0) for the std. selection and $[5139, 5419]$ MeV/c^2 (B^\pm and B^0), and $[5126, 5506]$ MeV/c^2 (B_s^0) for the alt. selection. As mentioned in [45] the average number of candidates per event is highly independent of the mass range.

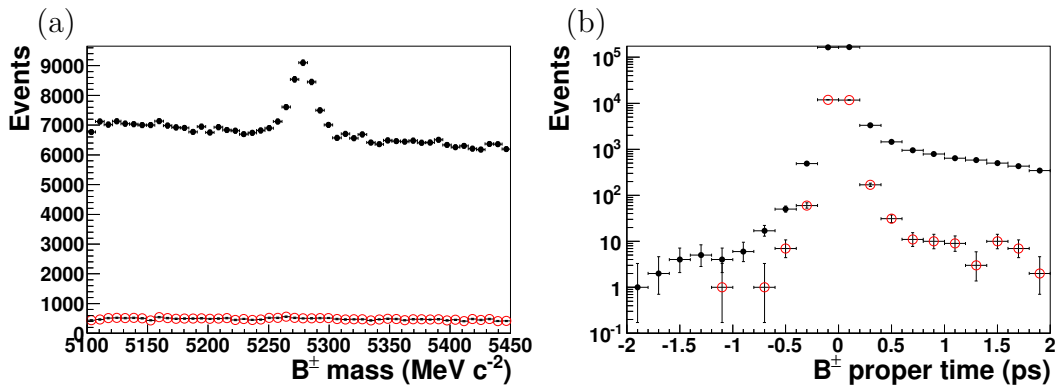


Figure 9.2.: Mass (a) and proper time (b) distributions of events rejected (red circles) and accepted (black points) by the best candidate selection. B^\pm candidate passing the std. selection are shown.

9.5. Selection efficiencies from Monte Carlo

In this section are presented the Monte Carlo efficiencies for the two selections, evaluated on *truth-matched*² candidates passing the stripping selection. Truth-matching efficiency is around 95% and flat, meaning that possible bias are negligible. For each cut, the efficiency is quoted relative to the events passing the previous set of cuts. The cuts for which the efficiency is 100% for both selections are not shown. The efficiencies for $B^+ \rightarrow J/\psi(1S) K^+$ are shown on Table 9.7, the $B^0 \rightarrow J/\psi(1S) K^{*0}$ ones on Table 9.8, and the $B_s^0 \rightarrow J/\psi(1S) \phi$ ones on Table 9.9. All the cut variables were described in Sections 9.2 to 9.4.

CUT	STD. [%]	ALT. [%]
$\chi_{\text{track}}^2 / \text{nDoF} (\mu)$	99.70 ± 0.01	100
$\Delta \ln \mathcal{L} (\mu/e)$	-	97.27 ± 0.02
$p_T (\mu)$	96.70 ± 0.02	96.70 ± 0.02
$\chi_{\text{vtx}}^2 (J/\psi)$	99.40 ± 0.01	99.13 ± 0.01
$ M_{\text{reco}}(J/\psi) - M(J/\psi) / \sigma_{M_{J/\psi}}$	97.84 ± 0.02	-
$\Delta \ln \mathcal{L} (K/\pi)$	97.90 ± 0.02	92.71 ± 0.04
$\Delta \ln \mathcal{L} (K/p)$	94.31 ± 0.03	86.05 ± 0.05
$\chi_{\text{track}}^2 / \text{nDoF} (K)$	99.71 ± 0.01	100
$p (K)$	89.60 ± 0.04	-
$M (B)$	99.99 ± 0.00	99.87 ± 0.01
$\chi_{\text{IP}}^2 / \text{nDoF} (B)$	98.53 ± 0.02	-
$\chi_{\text{DTF}}^2 / \text{nDoF} (B)$	99.27 ± 0.01	96.25 ± 0.03
$\chi_{\text{IP}}^2 / \text{nDoF}$ next best PV	96.64 ± 0.03	96.97 ± 0.03
TOS requirement	58.57 ± 0.08	58.29 ± 0.08

Table 9.7.: Efficiencies on Monte Carlo data for $B^+ \rightarrow J/\psi(1S) K^+$, evaluated on truth-matched candidate passing the stripping selection. A ‘-’ indicates that the cut is not applied.

²A truth-matched candidate is a reconstructed candidate which is checked to be the same as the generated decay.

CUT	STD. [%]	ALT. [%]
$\chi^2_{\text{track}}/\text{nDoF} (\mu)$	99.71 ± 0.01	100
$\Delta \ln \mathcal{L} (\mu/e)$	–	97.51 ± 0.02
$p_T (\mu)$	96.20 ± 0.02	96.20 ± 0.02
$\chi^2_{\text{vtx}} (J/\psi)$	99.34 ± 0.019	99.05 ± 0.01
$ M_{\text{reco}}(J/\psi) - M(J/\psi) /\sigma_{M_{J/\psi}}$	97.88 ± 0.02	–
$\Delta \ln \mathcal{L} (K/\pi)$	98.64 ± 0.01	95.13 ± 0.02
$\Delta \ln \mathcal{L} (K/p)$	90.33 ± 0.03	97.03 ± 0.02
$\chi^2_{\text{track}}/\text{nDoF} (K)$	99.66 ± 0.01	100
$\Delta \ln \mathcal{L} (\pi/K)$	–	96.22 ± 0.02
$\Delta \ln \mathcal{L} (\pi/e)$	–	97.53 ± 0.02
$\chi^2_{\text{track}}/\text{nDoF} (\pi)$	99.37 ± 0.01	100
$ M_{\text{reco}}(K^{*0}) - M(K^{*0}) $	94.52 ± 0.03	100
$\chi^2_{\text{vtx}}/\text{nDoF} (K^{*0})$	100	98.73 ± 0.01
$M (B^0)$	99.99 ± 0.00	99.88 ± 0.00
$\chi^2_{\text{vtx}}/\text{nDoF} (B^0)$	100	98.87 ± 0.01
$\chi^2_{\text{DTF}}/\text{nDoF}$	98.33 ± 0.02	97.38 ± 0.02
$\chi^2_{\text{IP}}/\text{nDoF} (B^0)$	98.77 ± 0.01	–
$\chi^2_{\text{IP}}/\text{nDoF}$ next best PV	98.35 ± 0.02	98.50 ± 0.02
TOS requirement	63.06 ± 0.06	62.89 ± 0.06

Table 9.8.: Efficiencies on Monte Carlo data for $B^0 \rightarrow J/\psi(1S) K^{*0}$, evaluated on truth-matched candidate passing the stripping selection. A ‘–’ indicates that the cut is not applied.

CUT	STD. [%]	ALT. [%]
$\chi_{\text{track}}^2 / \text{nDoF} (\mu)$	99.69 ± 0.01	100
$\Delta \ln \mathcal{L} (\mu/e)$	–	95.25 ± 0.04
$p_{\text{T}} (\mu)$	96.62 ± 0.03	96.62 ± 0.03
$\chi_{\text{vtx}}^2 (\text{J}/\psi)$	99.35 ± 0.01	99.08 ± 0.02
$ M_{\text{reco}}(\text{J}/\psi) - M(\text{J}/\psi) / \sigma_{M_{\text{J}/\psi}}$	97.85 ± 0.02	–
$\Delta \ln \mathcal{L} (\text{K}/\pi)$	98.24 ± 0.02	94.43 ± 0.04
$\Delta \ln \mathcal{L} (\text{K}/\text{p})$	–	92.84 ± 0.05
$\chi_{\text{track}}^2 / \text{nDoF} (\text{K})$	99.14 ± 0.02	100
$ M_{\text{reco}}(\phi) - M(\phi) $	92.44 ± 0.05	99.90 ± 0.01
$\chi_{\text{vtx}}^2 / \text{nDoF} (\phi)$	100	98.48 ± 0.02
$M (\text{B}_s^0)$	99.99 ± 0.00	99.96 ± 0.00
$\chi_{\text{vtx}}^2 / \text{nDoF} (\text{B}_s^0)$	100	98.68 ± 0.02
$\chi_{\text{DTF}}^2 / \text{nDoF}$	98.23 ± 0.02	97.19 ± 0.03
$\chi_{\text{IP}}^2 / \text{nDoF} (\text{B}_s^0)$	97.67 ± 0.03	–
$\chi_{\text{IP}}^2 / \text{nDoF}$ next best PV	97.13 ± 0.03	97.48 ± 0.03
TOS requirement	59.17 ± 0.09	59.30 ± 0.10

Table 9.9.: Efficiencies on Monte Carlo data for $\text{B}_s^0 \rightarrow \text{J}/\psi(1\text{S}) \phi$, evaluated on truth-matched candidate passing the stripping selection. A ‘–’ indicates that the cut is not applied.

9.5.1. Mass distributions from Monte Carlo

The mass distribution of selected truth-matched events for $B^+ \rightarrow J/\psi(1S) K^+$ can be found in Figure 9.3, $B^0 \rightarrow J/\psi(1S) K^{*0}$ can be found in Figure 9.4 and $B_s^0 \rightarrow J/\psi(1S) \phi$ can be found in Figure 9.5. The mass distributions are fitted with two Gaussians with a common mean, and the parameters are summarised in Table 9.10 and Table 9.11 for the std. and alt. selection respectively.

Both plots from Figure 9.4 show an asymmetric tail: this is due to a poorer momentum resolution on slow pions from the K^{*0} . A more recent analysis uses a Crystal Ball function to model the B mass distribution, which width depends on the per event mass error.

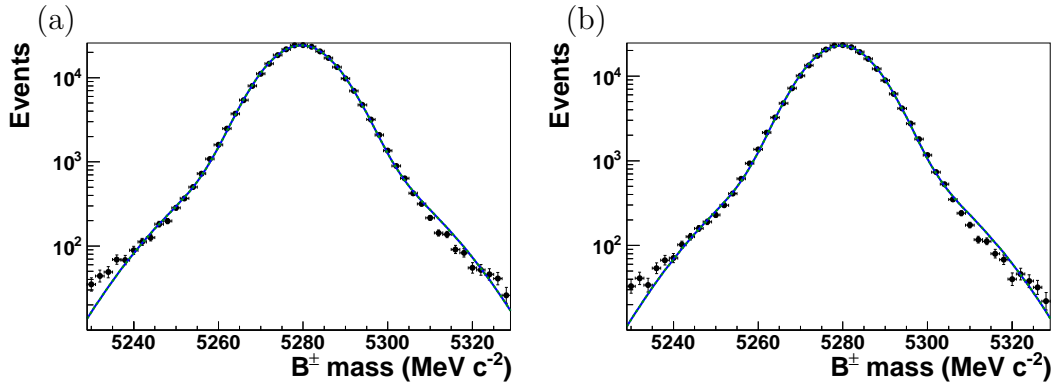


Figure 9.3.: Mass distribution of truth-matched selected $B^+ \rightarrow J/\psi(1S) K^+$ events, the mass shape is fitted with two Gaussian with a common mean, (a) is the std. selection and (b) the alt. selection.

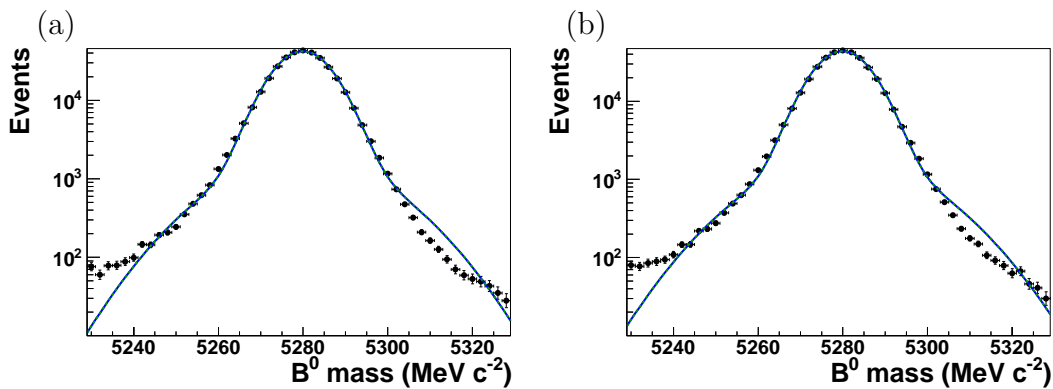


Figure 9.4.: Mass distribution of truth-matched selected $B^0 \rightarrow J/\psi(1S) K^{*0}$ events, the mass shape is fitted with two Gaussian with a common mean, (a) is the std. selection and (b) the alt. selection. In both cases, the model fits poorly the distribution tails. A recent analysis uses a Crystal Ball function, and the per event mass error as the width to model the asymmetric tail.

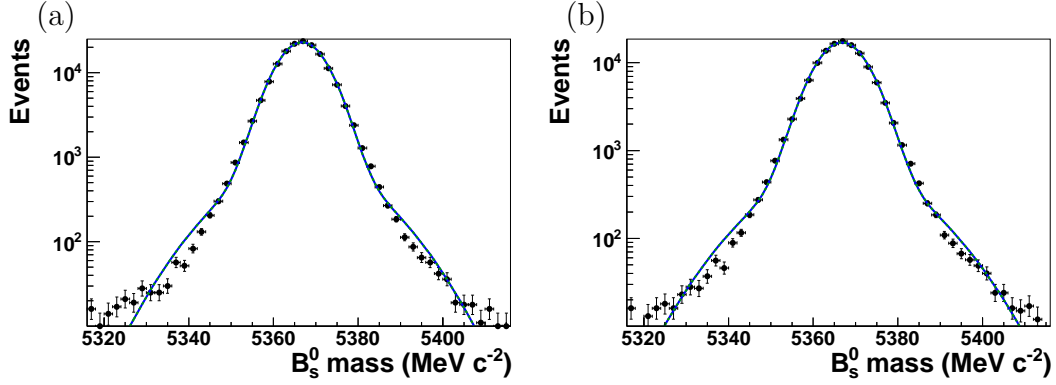


Figure 9.5.: Mass distribution of truth-matched selected $B_s^0 \rightarrow J/\psi(1S) \phi$ events, the mass shape is fitted with two Gaussian with a common mean, (a) is the std. selection and (b) the alt. selection.

CHANNEL	σ_{core} [MeV/ c^2]	σ_{wide} [MeV/ c^2]	f_{core}
$B^+ \rightarrow J/\psi(1S) K^+$	7.573 ± 0.025	16.66 ± 0.19	$(8.825 \pm 0.041) \cdot 10^{-1}$
$B^0 \rightarrow J/\psi(1S) K^{*0}$	6.357 ± 0.015	15.99 ± 0.14	$(9.032 \pm 0.023) \cdot 10^{-1}$
$B_s^0 \rightarrow J/\psi(1S) \phi$	5.348 ± 0.015	13.73 ± 0.17	$(9.150 \pm 0.030) \cdot 10^{-1}$

Table 9.10.: Mass PDF parameters from Monte Carlo data, for the std. selection. The two widths are σ_{core} and σ_{wide} , f_{core} is the fraction of the narrow Gaussian.

CHANNEL	σ_{core} [MeV/ c^2]	σ_{wide} [MeV/ c^2]	f_{core}
$B^+ \rightarrow J/\psi(1S) K^+$	7.400 ± 0.025	16.48 ± 0.19	$(8.875 \pm 0.040) \cdot 10^{-1}$
$B^0 \rightarrow J/\psi(1S) K^{*0}$	6.256 ± 0.014	16.29 ± 0.13	$(9.014 \pm 0.021) \cdot 10^{-1}$
$B_s^0 \rightarrow J/\psi(1S) \phi$	5.608 ± 0.021	14.74 ± 0.20	$(9.153 \pm 0.021) \cdot 10^{-1}$

Table 9.11.: Mass PDF parameters from Monte Carlo data, for the alt. selection. The two widths are σ_{core} and σ_{wide} , f_{core} is the fraction of the narrow Gaussian.

9.5.2. Proper time resolutions from Monte Carlo

The proper time resolution for $B^+ \rightarrow J/\psi(1S) K^+$ is shown in Figure 9.6, $B^0 \rightarrow J/\psi(1S) K^{*0}$ and $B_s^0 \rightarrow J/\psi(1S) \phi$ resolutions in Figure 9.7 and Figure 9.8 respectively. The resolution presented here is extracted from truth-matched selected candidates, for which the difference between the reconstructed and the generated proptime is plotted ($t_{\text{reco}} - t_{\text{true}}$). The fitted function is the sum of three Gaussians with a common mean, which will be discussed in Section 10.2. The fitted values of the parameters are summarised in Table 9.12 and Table 9.13 for the std. and alt. selection respectively.

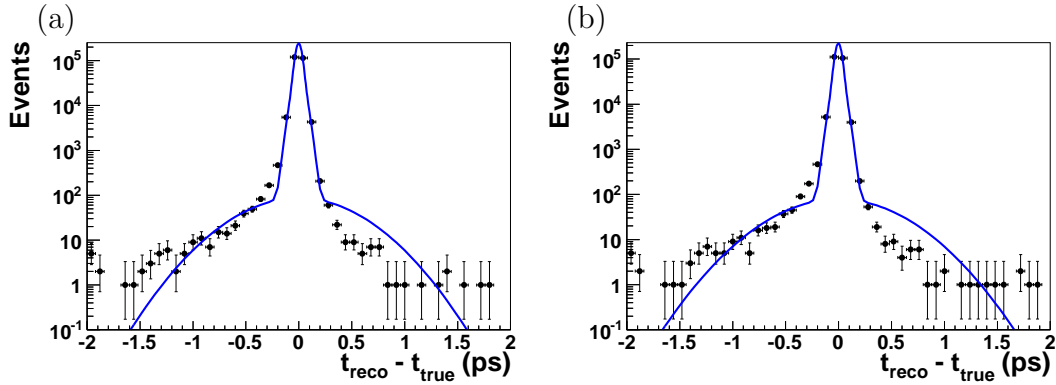


Figure 9.6.: Proper time resolution of truth-matched selected $B^+ \rightarrow J/\psi(1S) K^+$ events, the distribution is fitted with three Gaussians with a common mean, (a) is the std. selection and (b) the alt. selection.

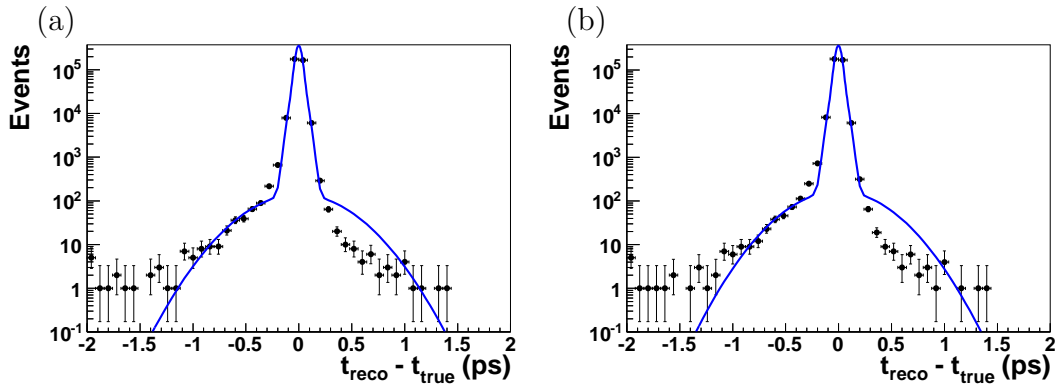


Figure 9.7.: Proper time resolution of truth-matched selected $B^0 \rightarrow J/\psi(1S) K^{*0}$ events, the distribution is fitted with three Gaussians with a common mean, (a) is the std. selection and (b) the alt. selection. The seen asymmetry is related to the tail seen on Figure 9.4.

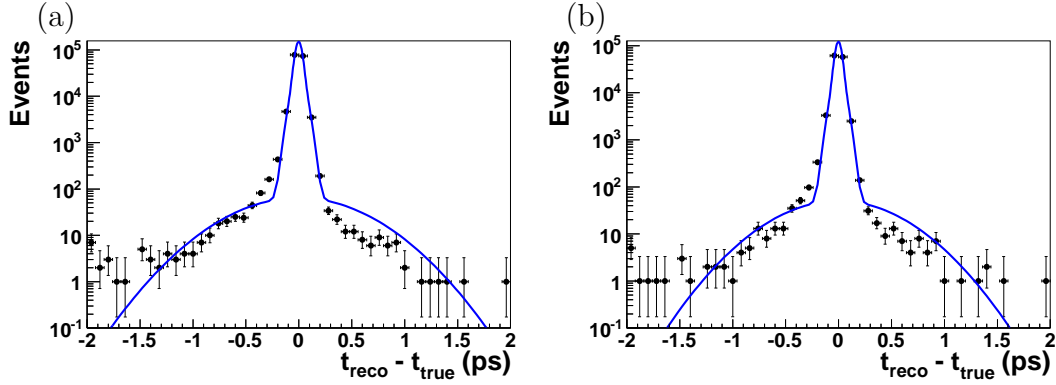


Figure 9.8.: Proper time resolution of truth-matched selected $B_s^0 \rightarrow J/\psi(1S) \phi$ events, the distribution is fitted with three Gaussians with a common mean, (a) is the std. selection and (b) the alt. selection.

VARIABLE	$B^+ \rightarrow J/\psi(1S) K^+$	$B^0 \rightarrow J/\psi(1S) K^{*0}$	$B_s^0 \rightarrow J/\psi(1S) \phi$
Δ [fs]	-1.271 ± 0.071	-1.322 ± 0.085	-1.592 ± 0.093
σ_1 [fs]	28.60 ± 0.16	27.89 ± 0.14	29.89 ± 0.23
σ_2 [fs]	56.64 ± 0.59	55.20 ± 0.47	60.42 ± 0.77
σ_3 [fs]	$(4.32 \pm 0.11) \cdot 10^2$	$(3.631 \pm 0.083) \cdot 10^2$	$(4.96 \pm 0.14) \cdot 10^2$
f_2	$(2.395 \pm 0.082) \cdot 10^{-1}$	$(2.573 \pm 0.072) \cdot 10^{-1}$	$(2.58 \pm 0.10) \cdot 10^{-1}$
f_3	$(4.12 \pm 0.21) \cdot 10^{-3}$	$(4.45 \pm 0.18) \cdot 10^{-3}$	$(6.13 \pm 0.29) \cdot 10^{-3}$

Table 9.12.: Proper time resolution parameters from Monte Carlo data, for the std. selection. The common mean is Δ , the three widths are σ_1 , σ_2 and σ_3 . The fraction of the second and third Gaussian is f_2 and f_3 respectively.

VARIABLE	$B^+ \rightarrow J/\psi(1S) K^+$	$B^0 \rightarrow J/\psi(1S) K^{*0}$	$B_s^0 \rightarrow J/\psi(1S) \phi$
Δ [fs]	-1.451 ± 0.074	-1.413 ± 0.057	-1.55 ± 0.10
σ_1 [fs]	29.00 ± 0.17	28.20 ± 0.14	28.77 ± 0.23
σ_2 [fs]	57.93 ± 0.64	55.96 ± 0.50	59.44 ± 0.87
σ_3 [fs]	$(4.55 \pm 0.12) \cdot 10^2$	$(3.499 \pm 0.076) \cdot 10^2$	$(4.59 \pm 0.15) \cdot 10^2$
f_2	$(2.263 \pm 0.082) \cdot 10^{-1}$	$(2.465 \pm 0.071) \cdot 10^{-1}$	$(2.52 \pm 0.11) \cdot 10^{-1}$
f_3	$(4.99 \pm 0.20) \cdot 10^{-3}$	$(4.45 \pm 0.18) \cdot 10^{-3}$	$(5.72 \pm 0.33) \cdot 10^{-3}$

Table 9.13.: Proper time resolution parameters from Monte Carlo data, for the alt. selection. The common mean is Δ , the three widths are σ_1 , σ_2 and σ_3 . The fraction of the second and third Gaussian is f_2 and f_3 respectively.

9.6. Event yields in data

In order to compare the two selections on data, a fit is performed to the mass distribution of selected events in the proper time range $[0.3, 14]$ ps. The used fit function is a double Gaussian with a common mean for the signal and a linear function for the background, as will be discussed in Chapter 10. The signal and background yields are summarised in Table 9.14. The plots are shown in Figure 9.9 for B^\pm , Figure 9.10 for B^0 and Figure 9.11 for B_s^0 .

For each selection, the number of signal divided by its error squared (S/σ_S^2), i.e. the purity, for the two selections is quoted, this is shown in Table 9.15. The purities are comparable, even if the alt. selection seems to have a slightly higher purity than the std. one for $B^0 \rightarrow J/\psi(1S) K^{*0}$.

The mass plots of the J/ψ , K^{*0} and ϕ are found in Appendix C.

CHANNEL	# SIGNAL EVENTS		# BACKGROUND EVENTS	
	Std. sel.	Alt. sel.	Std. sel.	Alt. sel.
$B^+ \rightarrow J/\psi(1S) K^+$	7394 ± 90	6291 ± 83	1428 ± 46	1284 ± 43
$B^0 \rightarrow J/\psi(1S) K^{*0}$	2839 ± 62	2964 ± 62	2627 ± 60	2692 ± 60
$B_s^0 \rightarrow J/\psi(1S) \phi$	624 ± 26	670 ± 27	236 ± 17	373 ± 21

Table 9.14.: Signal and background yields in the proper time range $[0.3, 14]$ ps. The B^\pm mass range is $[5150, 5400]$ MeV/c^2 for the std. selection and $[5139, 5419]$ MeV/c^2 for the alt. selection. The B^0 mass range is $[5200, 5400]$ MeV/c^2 for the std. selection and $[5179, 5379]$ MeV/c^2 for the alt. selection. The B_s^0 mass range is $[5200, 5550]$ MeV/c^2 for the std. selection and $[5226, 5506]$ MeV/c^2 for the alt. selection.

CHANNEL	S/σ_S^2	
	Std. sel.	Alt. sel.
$B^+ \rightarrow J/\psi(1S) K^+$	0.91	0.91
$B^0 \rightarrow J/\psi(1S) K^{*0}$	0.74	0.77
$B_s^0 \rightarrow J/\psi(1S) \phi$	0.92	0.92

Table 9.15.: Signal purities, extracted from Table 9.14.

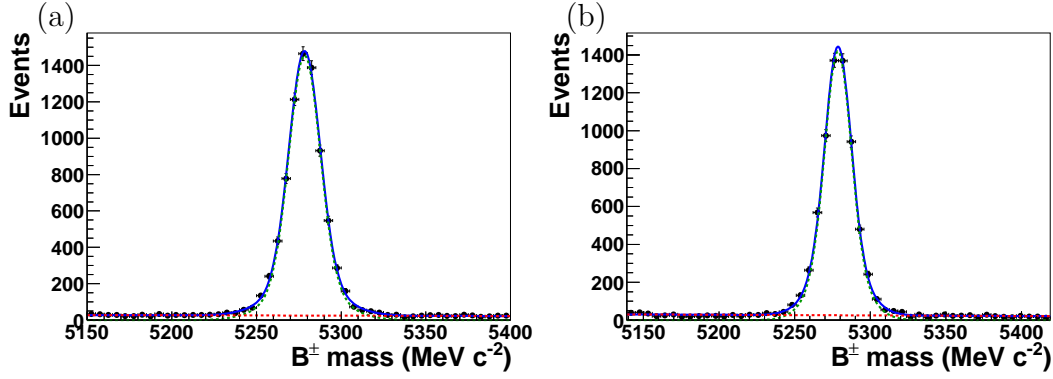


Figure 9.9.: Fit to the mass distribution of $B^\pm \rightarrow J/\psi(1S) K^\pm$ candidates in the proper time range $[0.3, 14]$ ps, (a) for the std. selection and (b) for the alt. selection. In blue is the total PDF, dotted green the signal PDF and in red the background PDF.

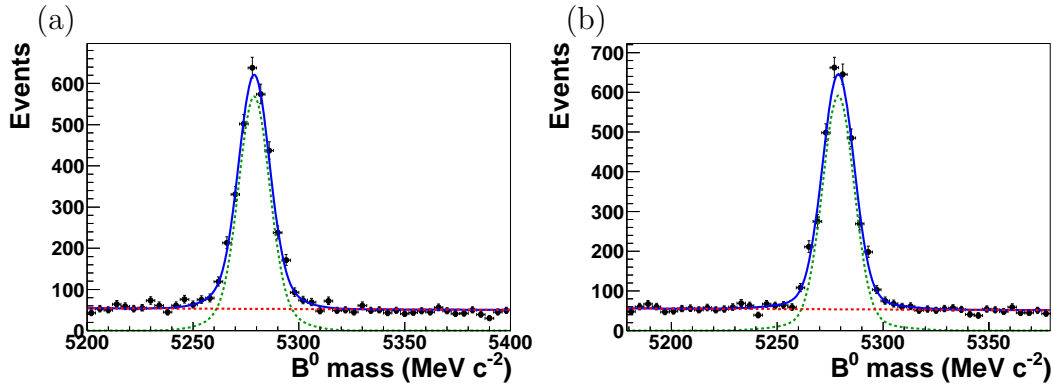


Figure 9.10.: Fit to the mass distribution of $B^0 \rightarrow J/\psi(1S) K^{*0}$ candidates in the proper time range $[0.3, 14]$ ps, (a) for the std. selection and (b) for the alt. selection. In blue is the total PDF, dotted green the signal PDF and in red the background PDF.

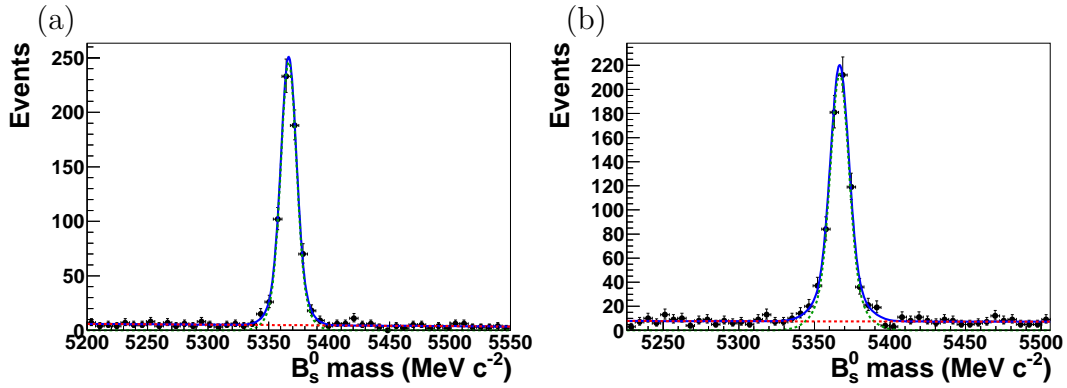


Figure 9.11.: Fit to the mass distribution of $B_s^0 \rightarrow J/\psi(1S) \phi$ candidates in the proper time range $[0.3, 14]$ ps, (a) for the std. selection and (b) for the alt. selection. In blue is the total PDF, dotted green the signal PDF and in red the background PDF.

Chapter 10.

Lifetime extraction

The strategy for extracting the B lifetime is to fit an exponential to the B proper time distribution on the selected data set, as discussed in Section 6.2.2. For the B_s^0 mode, the obtained ‘lifetime’, noted $\tau_{B_s^0}^{\text{single}}$ is extracted from fitting the proper time distribution of untagged $B_s^0 \rightarrow J/\psi(1S) \phi$ decays with a single exponential function. This does not correspond to Γ_s^{-1} (with $\Gamma_s = \frac{1}{2}(\Gamma_{Ls} + \Gamma_{Hs})$). The expected value of $\tau_{B_s^0}^{\text{single}}$ is 1.430 ps [45], and is computed by:

$$\tau_{B_s^0}^{\text{single}} = \frac{A \tau_{B_{sH}^0}^2 + B \tau_{B_{sL}^0}^2}{A \tau_{B_{sH}^0} + B \tau_{B_{sL}^0}} \quad (10.1)$$

where A and B depend on ϕ_s ¹:

$$\begin{aligned} A &= \left((1 - \cos \phi_s) \frac{|A_0(0)|^2}{2} + (1 - \cos \phi_s) \frac{|A_{\parallel}(0)|^2}{2} + (1 + \cos \phi_s) \frac{|A_{\perp}(0)|^2}{2} \right) \\ B &= \left((1 + \cos \phi_s) \frac{|A_0(0)|^2}{2} + (1 + \cos \phi_s) \frac{|A_{\parallel}(0)|^2}{2} + (1 - \cos \phi_s) \frac{|A_{\perp}(0)|^2}{2} \right) \end{aligned} \quad (10.2)$$

The three angular decay amplitudes $|A_0(0)|^2$, $|A_{\parallel}(0)|^2$ and $|A_{\perp}(0)|^2$ correspond the final states with angular momentum $L = 0, 1, 2$, resulting from the decay of the pseudo scalar B-meson into two vector mesons.

The fit procedure used in this study, described in Section 10.1, is very similar to the one used in [45]. Toy Monte Carlo studies have been performed, to check that there is no bias coming from the fitter on the measured quantities, namely the B lifetime and mass, this is discussed in Section 10.4.

¹Assuming a negligible $B_s^0\text{-}\bar{B}_s^0$ production asymmetry.

10.1. Lifetime fitter

The performed unbinned extended maximum likelihood fit uses two observables: the B mass (m_B) and the B proper time (t_B). This assumes the mass and proper time are uncorrelated, this assumption is checked to be true by comparing the upper and lower mass sidebands (shown in Appendix B). As in [45], the following likelihood is constructed:

$$\mathcal{L} = \prod_{i=0}^N \mathcal{P}(\vec{x}_i | \vec{\theta}) \quad (10.3)$$

where N is the number of selected candidates, $\vec{x} = (m_B \ t_B)$ and $\vec{\theta}$ represent the fitted physics and detector parameters. The total PDF \mathcal{P} is built out of two components:

$$\mathcal{P} = N_{\text{sig}} \cdot \mathcal{P}_{\text{sig}} + N_{\text{bkg}} \cdot \mathcal{P}_{\text{bkg}} \quad (10.4)$$

where the indices ‘sig’ and ‘bkg’ represent the signal and background components of the total PDF, which will be described later. The two \mathcal{P}_κ components read:

$$\mathcal{P}_\kappa(\vec{x}_i | \vec{\theta}) = \mathcal{P}_\kappa(m_B) \cdot \mathcal{P}_\kappa(t_B) \quad (10.5)$$

where $\mathcal{P}_\kappa(m_B)$ is the mass PDF and $\mathcal{P}_\kappa(t_B)$ is the proper time PDF, which will be described below.

10.1.1. Modelling the background

The background PDF is modelled by a linear function for the mass distribution (noted $\mathcal{P}_{\text{bkg}}(m_B)$) and the proper time distribution consists of two exponential functions describing the long tail, and a δ distribution describing the peak around $t \simeq 0$, which represents the candidates reconstructed using tracks from the PV. The resulting PDF for the background proper time distribution is given by Equation (10.6), and the total background PDF is shown in Equation (10.7). The resolution model $R(t_B, t)$ will be discussed in Section 10.2.

$$\mathcal{P}_{\text{bkg}}(t) = f_{\text{LL},1} e^{-\frac{t}{\tau_{\text{LL},1}}} + f_{\text{LL},2} e^{-\frac{t}{\tau_{\text{LL},2}}} + (1 - f_{\text{LL},1} - f_{\text{LL},2}) \delta(0) \quad (10.6)$$

$$\mathcal{P}_{\text{bkg}}(\vec{x}_i | \vec{\theta}) = \mathcal{P}_{\text{bkg}}(m_B) \cdot [\mathcal{P}_{\text{bkg}}(t) \otimes R(t_B, t)] \quad (10.7)$$

10.1.2. Modelling the signal

The signal component in the B mass is modelled using a double Gaussian sharing with a common mean μ_B and two width $\sigma_{B,1}$ and $\sigma_{B,2}$, noted $\mathcal{P}_{\text{sig}}(m_B)$, this choice is justified by the mass plots on Monte Carlo data presented in Section 9.5. The proper time distribution is modelled by a single exponential multiplied by the acceptance function $\varepsilon(t)$, as shown in Equation (10.8). Equation (10.9) shows the total signal PDF.

$$\mathcal{P}_{\text{sig}}(t) = e^{-\frac{t}{\tau_B}} \cdot \varepsilon(t) \quad (10.8)$$

$$\mathcal{P}_{\text{sig}}(\vec{x}_i | \vec{\theta}) = \mathcal{P}_{\text{sig}}(m_B) \cdot [\mathcal{P}_{\text{sig}}(t) \otimes R(t_B, t)] \quad (10.9)$$

The acceptance function $\varepsilon(t)$ will be described in Chapter 11. The total PDF is the sum of Equation (10.7) and Equation (10.9). To extract the B-mesons lifetime, an extended unbinned log-likelihood fit to the data is performed using this model.

10.2. Resolution model

The used resolution model [45] consists of three Gaussians with separate widths and a common mean Δ . It was shown that a more complex model, for instance using the per-event proper time error, does not improve the measurement of the lifetime. Once the cleaning of the tails in the negative proper time region described in Section 9.3, the remaining tail is due to the resolution, which can be used to extract the resolution parameters. Although the fit is performed over -2 to 14 ps, the resolution parameters are sensitive to the negative tail and prompt peak region. The mathematical expression of $R(t)$ is given in Equation (10.10).

$$R(t) = \sum_{i=1}^3 f_i \frac{1}{\sqrt{2\pi}\sigma_i} e^{-\frac{(t-\Delta)^2}{2\sigma_i^2}} \quad (10.10)$$

where $\sum_{i=1}^3 f_i = 1$. The six independent parameters of the resolution model, namely f_2 , f_3 , Δ , σ_1 , σ_2 and σ_3 , are floated in the fit.

10.3. Lifetime ratio extraction

The extraction of the lifetime ratio is performed by fitting simultaneously two data sets $A = \{\vec{x}_i^A\}$ and $B = \{\vec{x}_j^B\}$, with two PDFs $\mathcal{P}^A(\vec{x}_i^A | \vec{\theta}^A)$ and $\mathcal{P}^B(\vec{x}_i^B | \vec{\theta}^B)$. These two PDFs have the same mathematical form, and they are linked by a parameter r in the following way: \mathcal{P}^A models the proper time distribution with

$$\mathcal{P}_{\text{sig}}^A(t) = e^{-\frac{t}{\tau^A}} \cdot \varepsilon^A(t),$$

whilst \mathcal{P}^B uses

$$\mathcal{P}_{\text{sig}}^B(t) = e^{-\frac{t}{\tau^A r}} \cdot \varepsilon^B(t).$$

This allows to extract the lifetime τ^A from data set A and the lifetime ratio r from data set B . All parameters (of both PDFs) are floated.

10.4. Toy studies

The fitter is validated by running toy experiments where the same PDF is used for generation and fitting. As the fitter is almost the same as the one used in [45], biases on the B-meson lifetime and mass are not expected. The performed toy study checked that there is no bias on the aforementioned variables for a low statistics sample, corresponding to the number of B_s^0 events. Difficulties when using the full proper time range (i.e. $t_B \in [-2, 14]$ ps) caused the check to be performed on the region where the prompt background is absent: $t_B \in [0.3, 14]$ ps. Figure 10.1 shows the distributions for the lifetime τ_B value, error and pull. The pull distribution is fitted with a Gaussian, which has a mean and a width compatible with 0 and 1 respectively. Figure 10.2 shows similar plots for the B mass.

A similar study was performed with the lifetime ratio fitter. The used statistics was similar to the one in the B^- / B^+ ratio. Table 10.1 summarises the parameters of the pull distributions for the two B masses, the lifetime and the lifetime ratio. The ratio is affected by a 2σ bias, meaning that an additional systematic uncertainty as to be taken into account, this will be discussed in Section 13.4. The errors are thought well estimated, since all the widths are compatible with one.

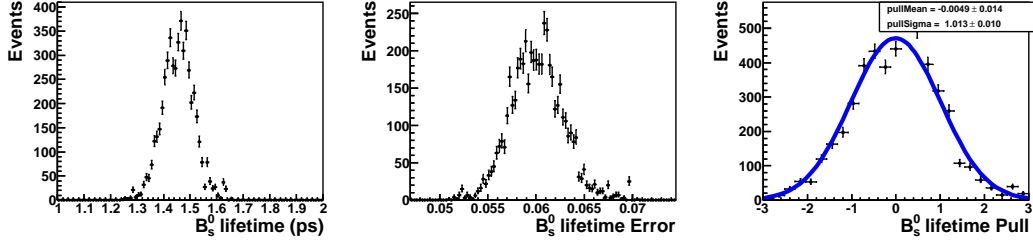


Figure 10.1.: Toy study results for τ_B . Left: τ_B distribution from the toys, centre: τ_B error distribution, right: τ_B pull distribution, fitted with a Gaussian. The mean is $(-0.5 \pm 1.4) \cdot 10^{-2}$ and the width is 1.013 ± 0.010 .

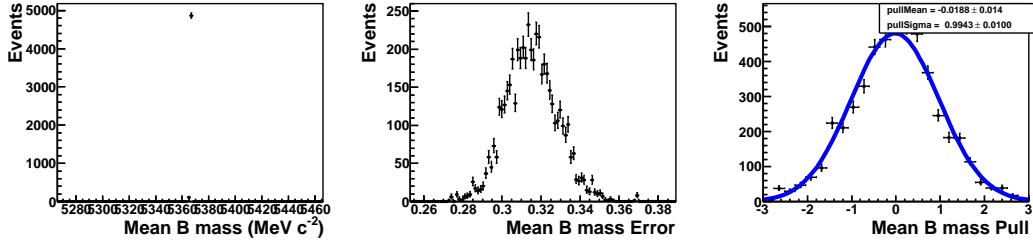


Figure 10.2.: Toy study results for m_B . Left: m_B distribution from the toys, centre: m_B error distribution, right: m_B pull distribution, fitted with a Gaussian. The mean is $(-1.9 \pm 1.4) \cdot 10^{-2}$ and the width is 0.994 ± 0.010 .

PARAMETER	PULL MEAN	PULL SIGMA
Mass of B_1	-0.007 ± 0.014	1.011 ± 0.011
Mass of B_2	0.027 ± 0.014	0.988 ± 0.010
Lifetime	-0.060 ± 0.014	0.992 ± 0.011
Ratio	0.037 ± 0.015	1.025 ± 0.012

Table 10.1.: Toy study results for the lifetime ratio fitter

Chapter 11.

Proper time acceptance

In this chapter the origin of the proper time acceptance will be discussed. A way to extract a correction from Monte Carlo data will be presented and the obtained correction values for the three decay channels and the two selection will be shown.

11.1. Method

Figure 11.1 shows how the generated exponential distribution could be distorted into the measured distribution, for a simplified acceptance function. The true proper time distribution $f_0(t_{\text{true}})$ follows an exponential function. The detector geometry and cuts in the triggers and selection cause the probability to detect the B-meson not to be flat across the considered proper time range. Finally reconstruction effects smear the distribution into $f_{\text{rec}}(t_{\text{rec}})$. In this approach it is clear that the acceptance as a function of the *true* proper time has to be used.

A strategy to study this effect and get a correction was developed using the simulated samples. All the selections are applied on those events and the acceptance function is obtained by comparing the accepted events with all the generated ones. In order not to be disturbed by misreconstructed events or combinatorial background, only truth-matched selected events are taken into account. The acceptance curve is obtained using the ROOFIT class **RooEfficiency**, which is able to evaluate the conditional probability of the event to be selected. An example of the resulting efficiency curve is shown in Figure 11.2, which also shows that the acceptance can be described by a linear function.

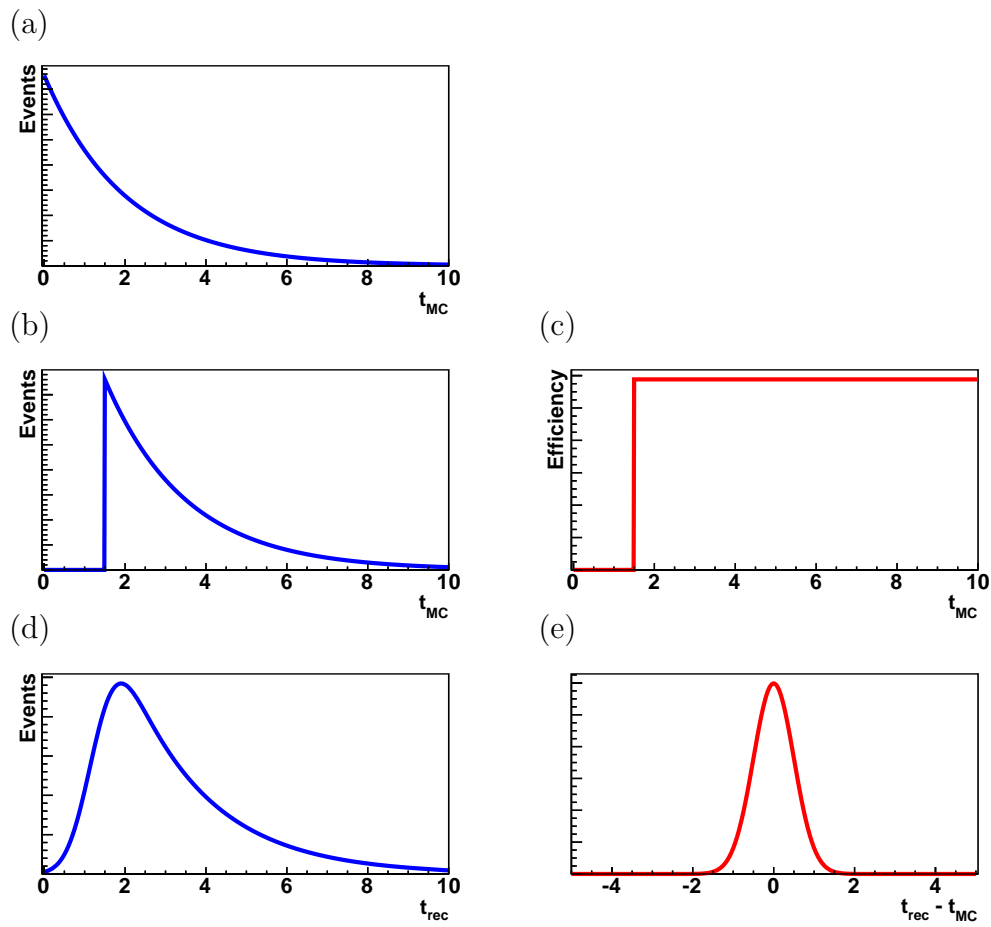


Figure 11.1.: Generated proper time distribution distorted into reconstructed distribution. Subfigure (a) shows the generated proper time distribution $f_0(t_{\text{true}})$, subfigure (b) shows the proper time distribution once the acceptance function $f_{\text{acc}}(t_{\text{true}})$, shown on subfigure (c), is applied. Subfigure (d) shows the reconstructed proper time distribution $f_{\text{reco}}(t_{\text{reco}})$, which obtained by convoluting $f_{\text{rec}}(t_{\text{rec}})$ with the resolution function $f_{\text{res}}(t_{\text{true}}, t_{\text{rec}})$, shown on subfigure (e). Units are arbitrary.

11.2. Results

As can be seen in Figure 11.2 for $B^+ \rightarrow J/\psi(1S) K^+$, the acceptance is rather well described by a linear function with a slope parameter β (the overall scale is irrelevant). Both the std. and alt. selections have a β value of $\mathcal{O}(10^{-2} \text{ ps}^{-1})$, which translates into a $\mathcal{O}(2\%)$ bias on the measured lifetime. The results are summarised in Table 11.1, the plots for B^0 and B_s^0 are shown on Figure 11.3 and Figure 11.4 respectively.

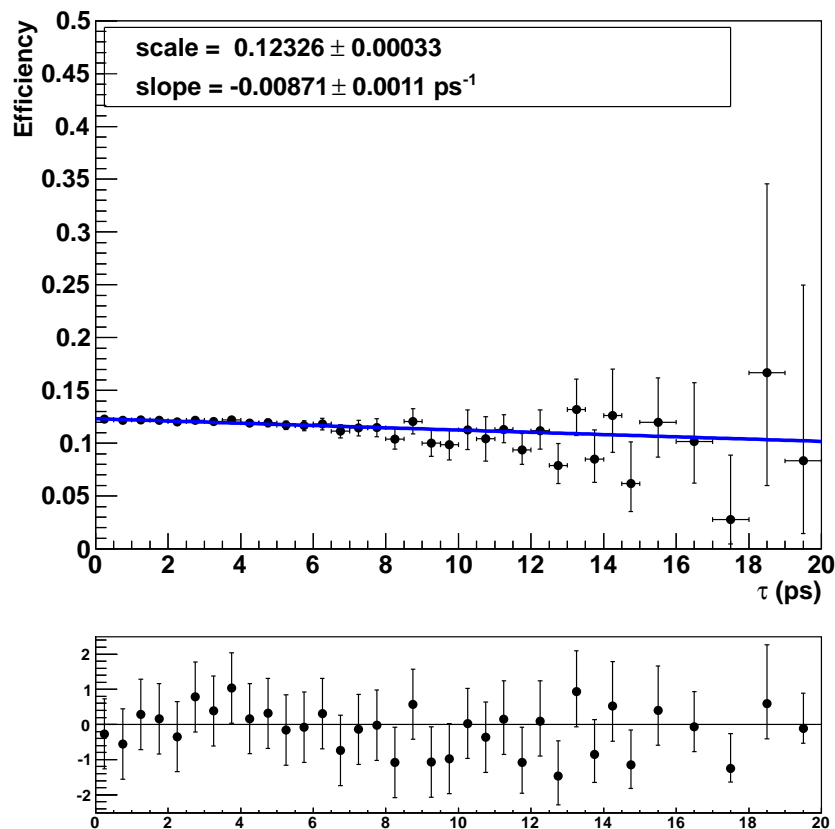


Figure 11.2.: Top plot: fitted acceptance for $B^+ \rightarrow J/\psi(1S) K^+$ for the alt. selection, the slope parameter is the β correction. The scale corresponds to the efficiency for $t = 0$. The selected (and truth-matched) events are normalised to *all* generated events. The fit reduced χ^2 is 0.45. Bottom plot: the pull distribution.

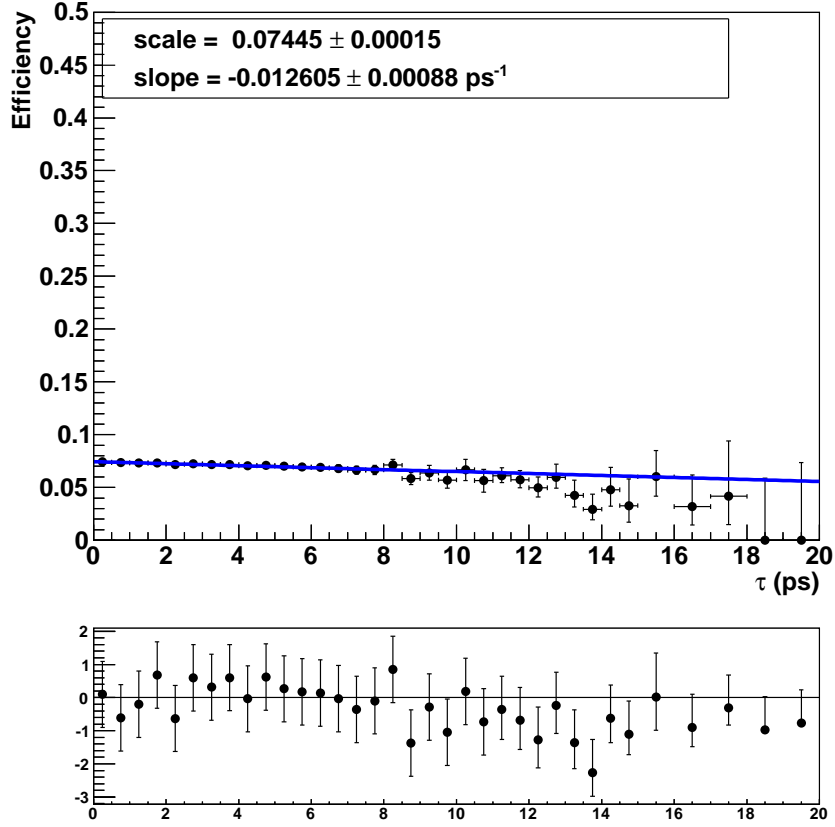


Figure 11.3.: Top plot: fitted acceptance for $B^0 \rightarrow J/\psi(1S) K^{*0}$ for the alt. selection. The scale corresponds to the efficiency for $t = 0$. The selected (and truth-matched) events are normalised to *all* generated events. The fit reduced χ^2 is 0.51. Bottom plot: the pull distribution.

CHANNEL	VALUE OF β [ps^{-1}]	
	Std selection	Alt. selection
$B^+ \rightarrow J/\psi(1S) K^+$	$(-1.05 \pm 0.11) \cdot 10^{-2}$	$(-0.87 \pm 0.11) \cdot 10^{-2}$
$B^0 \rightarrow J/\psi(1S) K^{*0}$	$(-1.220 \pm 0.089) \cdot 10^{-2}$	$(-1.260 \pm 0.088) \cdot 10^{-2}$
$B_s^0 \rightarrow J/\psi(1S) \phi$	$(-1.05 \pm 0.14) \cdot 10^{-2}$	$(-0.98 \pm 0.15) \cdot 10^{-2}$

Table 11.1.: Acceptance correction values for the three samples.

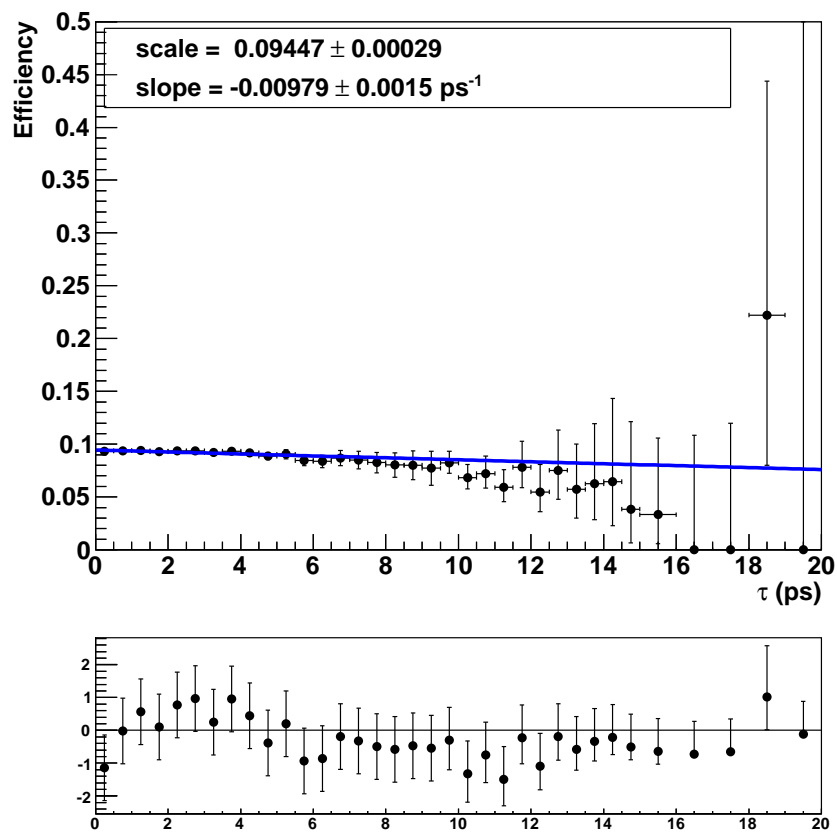


Figure 11.4.: Top plot: fitted acceptance for $B_s^0 \rightarrow J/\psi(1S) \phi$ for the alt. selection. The scale corresponds to the efficiency for $t = 0$. The selected (and truth-matched) events are normalised to *all* generated events. The fit reduced χ^2 is 0.62. Bottom plot: the pull distribution.

For the $\mathcal{CP}\mathcal{T}$ test, it is required that the acceptance is known with a sufficient precision for B^+ and B^- . The used procedure to extract the acceptance correction has access to the charge of the B-meson, allowing to split the data sample into B^+ and B^- . The results are shown in Table 11.2. The significant difference between $\beta(B^+)$ and $\beta(B^-)$ was diagnosed to be a statistical fluctuation by splitting the B^\pm data sample in the two magnet dipole polarities Up and Down, and applying the same procedure again. If a systematic shift was caused by an asymmetry depending on the B-mesons charge, the observed asymmetry would be the opposite with a change of the dipole magnet polarity. The results are shown in Table 11.3. In both subsamples the $\beta(B^+) > \beta(B^-)$ behaviour was seen.

CHANNEL	VALUE OF β [ps^{-1}]	
	Std selection	Alt. selection
$B^+ \rightarrow J/\psi(1S) K^+$	$(-1.05 \pm 0.11) \cdot 10^{-2}$	$(-0.87 \pm 0.11) \cdot 10^{-2}$
B^+ only	$(-1.19 \pm 0.15) \cdot 10^{-2}$	$(-1.09 \pm 0.16) \cdot 10^{-2}$
B^- only	$(-0.90 \pm 0.16) \cdot 10^{-2}$	$(-0.64 \pm 0.17) \cdot 10^{-2}$

Table 11.2.: Slope parameters for the total B^\pm sample, and the two subsamples B^+ and B^- .

CHANNEL AND POLARITY	VALUE OF β [ps^{-1}]	
	Std selection	Alt. selection
B^+ Up	$(-1.31 \pm 0.22) \cdot 10^{-2}$	$(-1.28 \pm 0.22) \cdot 10^{-2}$
B^+ Down	$(-1.07 \pm 0.22) \cdot 10^{-2}$	$(-0.90 \pm 0.23) \cdot 10^{-2}$
B^- Up	$(-0.84 \pm 0.22) \cdot 10^{-2}$	$(-0.57 \pm 0.24) \cdot 10^{-2}$
B^- Down	$(-0.96 \pm 0.22) \cdot 10^{-2}$	$(-0.71 \pm 0.23) \cdot 10^{-2}$

Table 11.3.: Slope parameters the two subsamples B^+ and B^- , computed separately for the dipole magnet Up and Down polarities.

11.3. Conclusion

Studies on Monte Carlo data showed that most of the observed slope comes from tracks of the daughters which are in the detector acceptance but are not reconstructed [47]. There is an increasing inefficiency in track reconstruction for tracks with an impact parameter

(IP) with respect to the beam axis greater than $600\ \mu\text{m}$ [47]. This inefficiency is partially coming from a the track reconstruction in the VELO, for the procedure requires that the track is pointing to the beam axis. Tracks passing through a sensor boundary are also known not be split into two tracks, which again decreases the reconstruction efficiency. Those two effects are dependent on the detector occupancy [48], and therefore on the average number of p p interactions per bunch crossing.

Since long-lived B-mesons are more prone to have at least one track with a (relatively) large IP with respect to the beam axis, the efficiency drops as a function of the proper time.

Chapter 12.

Results

In this chapter the measured lifetimes will be presented in Section 12.1 and the lifetime ratio measurements can be found in Section 12.3. The errors on the measurements shown in this chapter are statistical only, the systematic uncertainties will be discussed in Chapter 13. The proper time resolution is discussed in Section 12.2. The presented lifetimes and lifetime ratios do include the proper time acceptance correction. In Section 12.4 are presented cross-checks performed on the lifetime and on the lifetime ratio fitters.

12.1. Lifetime measurements

The two dimensional fit in the mass and the proper time described in Chapter 10 was used to extract the B-meson lifetime, using the dataset described in Chapter 7. The fit was performed on the $t_B \in [-2, 14]$ ps range for each channel, and all the parameters of the fit model are floated. The results obtained with the std. and alt. selections are summarised in Table 12.1.

The projections of the results of the two dimensional fit on the data for B^\pm , B^0 and B_s^0 are shown in Figure 12.1, Figure 12.3 and Figure 12.5 respectively for the std. selection. The projections for the alt. selection are presented in Figure 12.2, Figure 12.4, Figure 12.6 for B^\pm , B^0 and B_s^0 respectively.

CHANNEL	LIFETIME (STD SEL.) [ps]	LIFETIME (ALT. SEL.) [ps]
$B^+ \rightarrow J/\psi(1S) K^+$	1.663 ± 0.019	1.664 ± 0.021
$B^0 \rightarrow J/\psi(1S) K^{*0}$	1.528 ± 0.030	1.523 ± 0.029
$B_s^0 \rightarrow J/\psi(1S) \phi$	1.453 ± 0.058	1.491 ± 0.059

Table 12.1.: Results of the two dimensional fit for the lifetime of the B-mesons in the proper time range $t_B \in [-2, 14]$ ps. The proper time acceptance has been included in the fit.

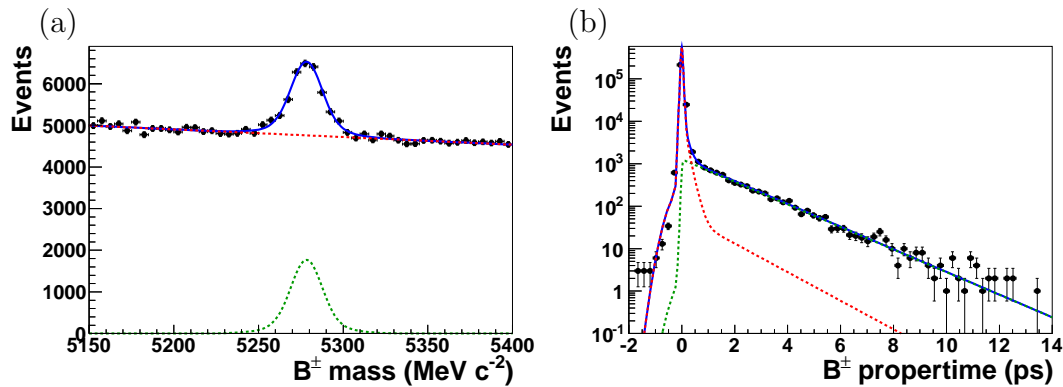


Figure 12.1.: Projections of the two dimensional fit for $B^+ \rightarrow J/\psi(1S) K^+$, std. selection: (a) the B^\pm mass and (b) the B^\pm proper time. The green dashed line is the signal PDF, the red dashed line is the background PDF, the solid blue line is the total.

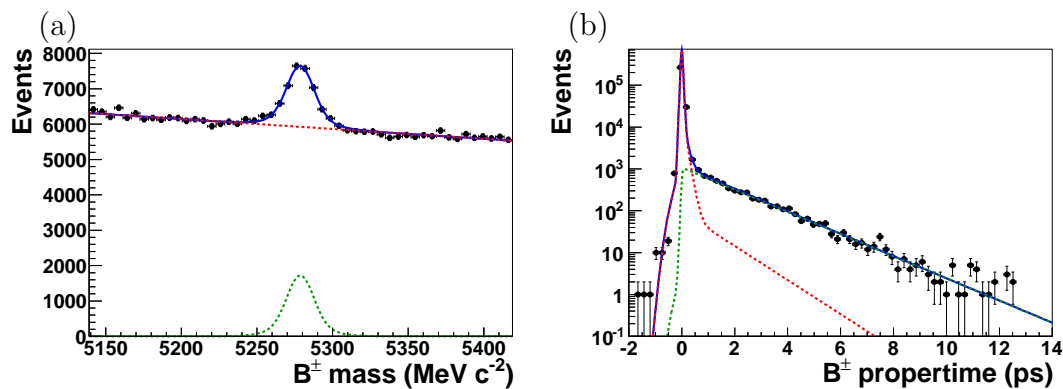


Figure 12.2.: Projections of the two dimensional fit for $B^+ \rightarrow J/\psi(1S) K^+$, alt. selection: (a) the B^\pm mass and (b) the B^\pm proper time. The green dashed line is the signal PDF, the red dashed line is the background PDF, the solid blue line is the total.

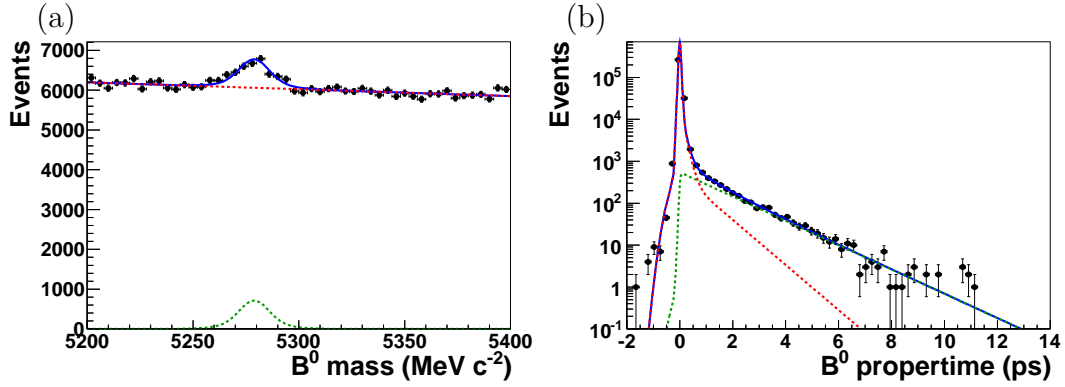


Figure 12.3.: Projections of the two dimensional fit for $B^0 \rightarrow J/\psi(1S) K^{*0}$, std. selection: (a) the B^0 mass and (b) the B^0 proper time. The green dashed line is the signal PDF, the red dashed line is the background PDF, the solid blue line is the total.

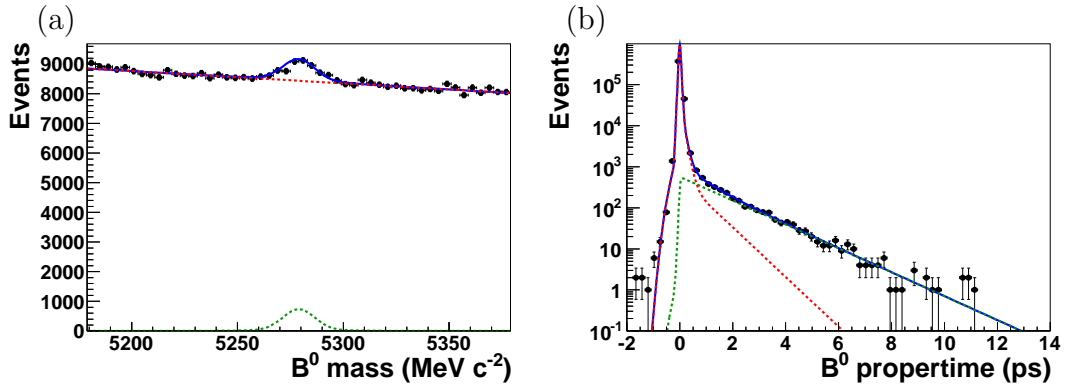


Figure 12.4.: Projections of the two dimensional fit for $B^0 \rightarrow J/\psi(1S) K^{*0}$, alt. selection: (a) the B^0 mass and (b) the B^0 proper time. The green dashed line is the signal PDF, the red dashed line is the background PDF, the solid blue line is the total.

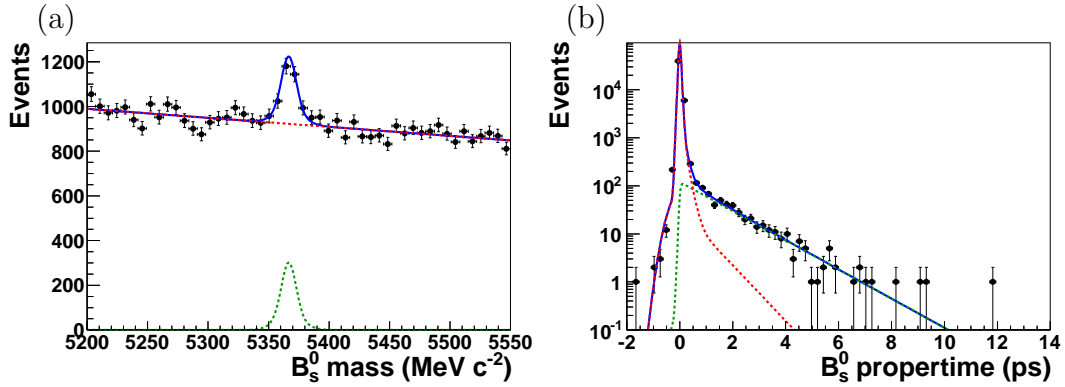


Figure 12.5.: Projections of the two dimensional fit for $B_s^0 \rightarrow J/\psi(1S) \phi$, std. selection: (a) the B_s^0 mass and (b) the B_s^0 proper time. The green dashed line is the signal PDF, the red dashed line is the background PDF, the solid blue line is the total.

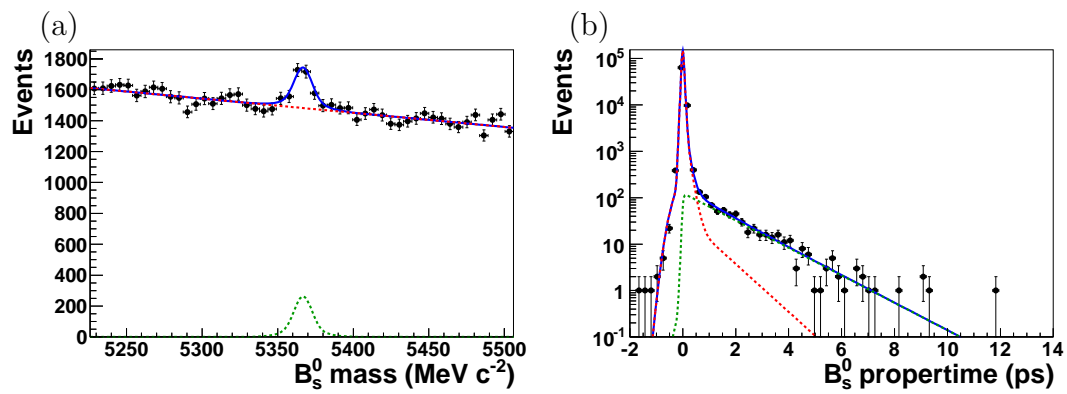


Figure 12.6.: Projections of the two dimensional fit for $B_s^0 \rightarrow J/\psi(1S) \phi$, alt. selection: (a) the B_s^0 mass and (b) the B_s^0 proper time. The green dashed line is the signal PDF, the red dashed line is the background PDF, the solid blue line is the total.

12.2. Proper time resolution

The proper time resolution is a critical parameter for LHCb. The VELO was designed to achieve a proper time resolution of $\mathcal{O}(50 \text{ fs})$ for b-hadron decays¹. This precision is one of the key points to get an accurate measurement of ϕ_s . In this study three Gaussians are used to model the resolution function, but a single number is more convenient to judge the accuracy of the proper time reconstruction. This is why two numbers were computed: the quadratic mean σ_{quad} , and the RMS of the distribution of the three Gaussians σ_{RMS} . The quadratic mean is given by:

$$\sigma_{\text{quad}}^2 = \sum_{i=1}^3 f_i \sigma_i^2$$

These two numbers were equal in all six cases, this is why Table 12.2 only gives σ_{RMS} for each channel and per selection.

CHANNEL	STD. SELECTION [ps]	ALT. SELECTION [ps]
$B^+ \rightarrow J/\psi(1S) K^+$	0.044	0.048
$B^0 \rightarrow J/\psi(1S) K^{*0}$	0.041	0.051
$B_s^0 \rightarrow J/\psi(1S) \phi$	0.057	0.059

Table 12.2.: Estimation of the proper time resolution, for each channel and the two selection.

12.3. Lifetime ratio measurements

The lifetime ratio is extracted using the simultaneous two-dimensional fit described in Chapter 10. The fit was performed on the $t_B \in [-2, 14]$ ps range for each channel with all parameters floated. The results obtained with both the std. and alt. selections are given in Table 12.3.

¹The value depends on the number of charged tracks, thus on the decay channel.

CHANNELS	RATIO (STD. SEL.)	RATIO (ALT. SEL.)
B^\pm / B^0	1.094 ± 0.023	1.096 ± 0.023
B_s^0 / B^0	0.957 ± 0.043	0.984 ± 0.043
B^- / B^+	1.024 ± 0.024	1.020 ± 0.025

Table 12.3.: Results of the two dimensional simultaneous fit for the ratio of the B-mesons lifetimes in the proper time range $t_B \in [-2, 14]$ ps. The proper time acceptance has been included in the fit.

12.4. Cross-checks

The lifetime fit is used in the proper time range $t_B \in [0.3, 14]$ ps, i.e. where the signal purity is higher. This requires the resolution parameters to be fixed to the values obtained from the $t_B \in [-2, 14]$ ps range fit, the obtained results are shown in Table 12.4. For both selections the results agree with those from Table 12.1 within less than one sigma, which is reassuring: the background model describes the data reasonably well.

CHANNEL	LIFETIME (STD SEL.) [ps]	LIFETIME (ALT. SEL.) [ps]
$B^+ \rightarrow J/\psi(1S) K^+$	1.669 ± 0.020	1.676 ± 0.022
$B^0 \rightarrow J/\psi(1S) K^{*0}$	1.519 ± 0.030	1.508 ± 0.030
$B_s^0 \rightarrow J/\psi(1S) \phi$	1.420 ± 0.058	1.474 ± 0.059

Table 12.4.: Results of the two dimensional fit for the lifetime of the B-mesons in the proper time range $t_B \in [0.3, 14]$ ps.

The lifetime ratio fitter was checked by using the same data sample twice, meaning that the expected ratio has to be one and the lifetime should correspond to the value obtained from the simple lifetime fit. This was done with the std. selection only, and the results are summarised in Table 12.5. The two ratio are compatible with one and the two lifetimes are very close to the ones from Table 12.1, this is again reassuring.

12.5. Full fit results

In Table 12.6 are shown all the parameters coming out of the two dimensional fit to extract the B^\pm lifetime for the two selections. The used PDFs were described in Chapter 10,

CHANNELS	LIFETIME [ps]	RATIO
B^\pm / B^\pm	1.667 ± 0.019	0.995 ± 0.016
B^0 / B^0	1.518 ± 0.028	1.003 ± 0.026

Table 12.5.: Results of the two dimensional simultaneous fit for the ratio of the B-mesons lifetimes in the proper time range $t_B \in [-2, 14]$ ps.

here below their mathematical forms are given with their parameters.

$$\begin{aligned} \mathcal{P}_{\text{sig}}(m_B) &= f_{\text{core}} e^{-\frac{(m_B - M)^2}{2\sigma_{\text{core}}^2}} + (1 - f_{\text{core}}) e^{-\frac{(m_B - M)^2}{2\sigma_{\text{wide}}^2}} \\ \mathcal{P}_{\text{bkg}}(m_B) &= \alpha m_B \\ \mathcal{P}_{\text{sig}}(t_B) &= \left(e^{-\frac{t}{\tau}} (1 - \beta t) \right) \otimes R(t_B, t) \\ \mathcal{P}_{\text{bkg}}(t_B) &= \left(f_{\text{LL},1} e^{-\frac{t}{\tau_{\text{LL},1}}} + f_{\text{LL},2} e^{-\frac{t}{\tau_{\text{LL},2}}} + (1 - f_{\text{LL},1} - f_{\text{LL},2}) \delta(0) \right) \otimes R(t_B, t) \end{aligned}$$

where $R(t_B, t)$ is the resolution function:

$$R(t_B, t) = (1 - f_2 - f_3) e^{-\frac{(t_B - \Delta)^2}{2(\sigma_1 \zeta)^2}} + f_2 e^{-\frac{(t_B - \Delta)^2}{2(\sigma_2 \zeta)^2}} + f_3 e^{-\frac{(t_B - \Delta)^2}{2(\sigma_3 \zeta)^2}} \quad (12.1)$$

and ζ is a nuisance parameter, which will be discussed in Chapter 13.

PARAMETER	VALUE (STD. SEL.)	VALUE (STD. SEL.)
f_{core}	$(7.58 \pm 0.31) \cdot 10^{-1}$	$(7.41 \pm 0.30) \cdot 10^{-1}$
σ_{core} [MeV/ c^2]	8.99 ± 0.16	8.76 ± 0.20
σ_{wide} [MeV/ c^2]	18.95 ± 0.96	17.70 ± 0.77
α [c^2/MeV]	$(-4.82 \pm 0.35) \cdot 10^{-2}$	$(-6.61 \pm 0.32) \cdot 10^{-2}$
τ [ps]	1.663 ± 0.019	1.664 ± 0.021
$f_{\text{LL},1}$	$(3.45 \pm 0.14) \cdot 10^{-2}$	$(3.64 \pm 0.18) \cdot 10^{-2}$
$\tau_{\text{LL},1}$ [ps]	$(1.254 \pm 0.048) \cdot 10^{-1}$	$(1.009 \pm 0.039) \cdot 10^{-1}$
$f_{\text{LL},2}$	$(1.47 \pm .22) \cdot 10^{-3}$	$(1.49 \pm 0.17) \cdot 10^{-3}$
$\tau_{\text{LL},2}$ [ps]	1.29 ± 0.14	1.065 ± 0.095
Δ [MeV/ c^2]	$(-9.7 \pm 1.0) \cdot 10^{-4}$	$(-1.15 \pm 0.10) \cdot 10^{-3}$
σ_1 [fs]	32.5 ± 4.5	32.28 ± 0.85
f_2	$(2.92 \pm 0.11) \cdot 10^{-1}$	$(3.10 \pm 0.11) \cdot 10^{-1}$
σ_2 [fs]	64.2 ± 8.8	63.1 ± 1.7
f_3	$(4.17 \pm 0.22) \cdot 10^{-3}$	$(5.65 \pm 0.54) \cdot 10^{-3}$
σ_3 [fs]	358 ± 52	264 ± 12
N_{sig}	$(9.13 \pm 0.11) \cdot 10^3$	$(7.767 \pm 0.098) \cdot 10^3$
N_{bkg}	$(238.23 \pm 0.49) \cdot 10^3$	$(296.14 \pm 0.54) \cdot 10^3$
ζ	1.00 ± 0.14	$(9.94 \pm 0.27) \cdot 10^{-1}$

Table 12.6.: Full fit results for $B^+ \rightarrow J/\psi(1S) K^+$ lifetime fit for the two selection.

Chapter 13.

Systematic uncertainties

In this chapter are presented the sources of systematic uncertainties and their magnitudes, for the three studied channels and the two selections. In Section 13.1 are treated the systematic uncertainties coming from the used fitting model, and in Section 13.2 the ones due to the acceptance correction. A discussion of the systematic uncertainties for the lifetime ratio measurement is presented in Section 13.4. A summary and the total systematic uncertainties will be presented in Section 13.5.

13.1. Fit model

The used fit model is almost the same as the one used in [45], the only difference is that the signal mass model is using two Gaussians in this study instead of one. This is why some of the presented numbers are taken from [45]. For each channel and for each selection, a table can be found in Appendix A.1, containing the different values of the lifetime with the different fit models.

13.1.1. Signal mass model

In this study the B mass signal is modelled with two Gaussians instead of one in [45]. The absolute difference with fit results using a Crystall Ball function is taken as systematic uncertainty, those two values are given in Table 13.1 for the three decay channels.

CHANNEL	FITTED LIFETIME [ps]	ABS. DIFFERENCE [ps]
$B^+ \rightarrow J/\psi(1S) K^+$	1.665 ± 0.020	0.002
$B^0 \rightarrow J/\psi(1S) K^{*0}$	1.521 ± 0.030	0.001
$B_s^0 \rightarrow J/\psi(1S) \phi$	1.456 ± 0.058	0.003

Table 13.1.: Lifetime of the B-mesons obtained using a Crystal Ball function instead of two Gaussians for the signal mass description, for the std. selection, and the absolute difference with the results from Table 12.1.

13.1.2. Background mass model

The systematic uncertainty from the background mass model is estimated by using a second order polynomial instead of a first order polynomial. The absolute difference between the two obtained lifetimes is taken as the systematic uncertainty. The fitted lifetime and the difference are found in Table 13.2.

CHANNEL	FITTED LIFETIME [ps]	ABS. DIFFERENCE [ps]
$B^+ \rightarrow J/\psi(1S) K^+$	1.664 ± 0.019	0.001
$B^0 \rightarrow J/\psi(1S) K^{*0}$	1.525 ± 0.030	0.001
$B_s^0 \rightarrow J/\psi(1S) \phi$	1.451 ± 0.058	0.002

Table 13.2.: Lifetime of the B-mesons obtained using a second order polynomial instead of a first order one for the mass background description, for the std. selection.

13.1.3. Background time model

The long lived background is modelled by two exponential, as mentioned in Section 10.1.1, which allows a good description of the Monte Carlo data, but could be inaccurate in data. The values quoted in Table 13.5 are the ones from [45], where a background subtraction is used, which is independant of any model of the proper time background distribution.

13.1.4. Time resolution model

Studies on Monte Carlo data show that the prompt J/ψ peak gives a good estimation of the resolution. The difference between the dilution of the resolutions obtained using

an inclusive J/ψ and signal Monte Carlo samples was shown to be 1.2%. Additionally, the decay time resolution was shown to vary of 1.1% with different time ranges on data. These two errors are combined linearly, and a safety factor of 2 is applied, resulting in a 4% error. Instead of using multiple fits to estimate the systematic uncertainty, a nuisance parameter which multiplies the three widths is added to the fit model (see Equation (12.1)). This nuisance parameter is floated in the fit, and is constrained by a Gaussian, having a mean of 1 and a width of 1.04. This allows to include the systematic uncertainty in the fit error.

13.2. Proper time acceptance correction

As discussed in Chapter 11, the Monte Carlo data indicates that the candidate reconstruction efficiency decreases with the proper time, even if the unbiased triggers and selections are used. This is now understood as being caused by the track reconstruction algorithm not finding all tracks with a large IP to the z axis. In this analysis the correction given in Table 11.1 is applied, and the systematic uncertainty is obtained by changing the value of β by its error. In Table 13.3 are shown the fitted lifetime which has the biggest difference with respect to the value from Table 12.1. The numbers corresponding to the alt. selection are shown in Table 13.4.

CHANNEL	FITTED LIFETIME [ps]	ABS. DIFFERENCE [ps]
$B^+ \rightarrow J/\psi(1S) K^+$	1.662 ± 0.019	0.003
$B^0 \rightarrow J/\psi(1S) K^{*0}$	1.523 ± 0.030	0.003
$B_s^0 \rightarrow J/\psi(1S) \phi$	1.457 ± 0.058	0.003

Table 13.3.: Lifetime of the B-mesons obtained varying the value of β by its error, for the std. selection.

13.3. Other systematic uncertainty sources

There are two contributions which remain to be presented: the momentum scale and the decay length scale. Both values can be found in Table 13.5 and are taken from [45].

CHANNEL	FITTED LIFETIME [ps]	ABS. DIFFERENCE [ps]
$B^+ \rightarrow J/\psi(1S) K^+$	1.668 ± 0.021	0.003
$B^0 \rightarrow J/\psi(1S) K^{*0}$	1.525 ± 0.029	0.002
$B_s^0 \rightarrow J/\psi(1S) \phi$	1.495 ± 0.059	0.004

Table 13.4.: Lifetime of the B-mesons obtained varying the value of β by its error, for the alt. selection.

The momentum scale is calibrated with a precision of $0.05 \pm 0.02\%$ [49]. The proper time expression is given by:

$$t = \frac{dm}{p} \quad (13.1)$$

where d is the flight distance, m the reconstructed mass and p the momentum. The reconstructed mass m depends on the momentum, therefore the momentum scale does not contribute to the systematic uncertainty, the error on p cancels in the ratio $\frac{m}{p}$.

The decay length scale represents the error on the measurement of the flight distance of the B-mesons in the z direction. It depends on the alignment, number of tracks in the decay, number of VELO modules containing a hit, ... A more detailed explanation can be found in [45]. The relative error on the lifetime is 0.03%.

13.4. Lifetime ratio systematic uncertainties

The sources of systematic uncertainties discussed in Sections 13.1 to 13.3 also affects the measurement of the lifetime ratio.

The systematic uncertainties of the fit model are all computed with the same method, except for the background time model, where the worst case estimate is used: the quoted systematic uncertainty on the ratio is the quadratic sum of the two systematic uncertainties on the lifetimes.

The systematic uncertainties due to the proper time acceptance are obtained from Monte Carlo data: therefore they are uncorrelated in the ratio. This is why they are computed in a similar way as for the lifetime measurement: the two β values are shifted by one σ and the maximum absolute difference¹ is quoted as the systematic uncertainty.

¹There are four different configurations taken into account.

The momentum scale does not affect the lifetime measurement, it does not affect the lifetime ratio measurement either. The decay length scale systematic uncertainty cancels in the ratio.

The fitter has a bias measured to be 0.037 ± 0.015 (see Section 10.4), this results in an additional systematic uncertainty corresponding to 3.7% of the statistical uncertainty.

The systematic uncertainties can be found in Section 13.5, complete tables are found in Appendix A.2.

13.5. Summary

In Table 13.5 a summary of the systematic uncertainties on the lifetime presented in this chapter is shown for the std. selection, whilst the summary concerning the alt. selection is presented in Table 13.6. In both cases the total systematic error is computed for each channel. The statistical uncertainty is given as well as a reference.

	$B^+ \rightarrow J/\psi(1S) K^+$	$B^0 \rightarrow J/\psi(1S) K^{*0}$	$B_s^0 \rightarrow J/\psi(1S) \phi$
Signal mass model	0.002	0.001	0.003
Background mass model	0.001	0.001	0.002
Background time model	0.001	0.004	0.002
Decay length scale	0.0005	0.0005	0.0005
Proper time acceptance	0.003	0.003	0.003
Total systematic uncertainty	0.004	0.005	0.005
Statistical uncertainty	0.019	0.030	0.058

Table 13.5.: Summary table of systematic uncertainties on the lifetime measurements, std. selection, in ps.

In Table 13.7 a summary of the systematic uncertainties on the lifetime ratio presented in this chapter is shown for the std. selection, whilst the summary concerning the alt. selection is presented in Table 13.8. In both cases the total systematic error is computed for each channel. In Table 13.8 it can be seen that the largest component in the systematic uncertainty on the B_s^0/B^0 lifetime ratio comes from the signal mass model. Comparing the fit results from the lifetime fits to the lifetime ratio fit, it appears that the double Gaussian model underestimates the lifetime of the B^0 when fitting for the ratio, but the

	$B^+ \rightarrow J/\psi(1S) K^+$	$B^0 \rightarrow J/\psi(1S) K^{*0}$	$B_s^0 \rightarrow J/\psi(1S) \phi$
Signal mass model	0.003	0.002	0.008
Background mass model	0.0005	0.002	0.002
Background time model	0.001	0.004	0.002
Decay length scale	0.0005	0.0005	0.0005
Proper time acceptance	0.004	0.003	0.004
Total systematic uncertainty	0.005	0.006	0.009
Statistical uncertainty	0.021	0.029	0.059

Table 13.6.: Summary table of systematic uncertainties on the lifetime measurements, alt. selection, in ps.

Crystal Ball model gives similar lifetime. For the B_s^0 , both models give similar lifetimes. The underestimation may be related to the correlation between low mass signal events with poorer resolution events, for which the reconstructed proper time is too low seen on Monte Carlo data.

	B^\pm / B^0	B_s^0 / B^0	B^- / B^+
Signal mass model	0.005	0.0004	0.0004
Background mass model	0.001	0.001	0.001
Background time model	0.001	0.006	0.003
Proper time acceptance	0.003	0.006	0.006
Fitter bias	0.0009	0.002	0.0009
Total systematic uncertainty	0.006	0.009	0.007
Statistical uncertainty	0.023	0.043	0.024

Table 13.7.: Summary table of systematic uncertainties on the lifetime ratio measurements, std. selection.

	B^\pm / B^0	B_s^0 / B^0	B^- / B^+
Signal mass model	0.001	0.009	0.003
Background mass model	0.001	0.0001	0.0002
Background time model	0.001	0.006	0.003
Proper time acceptance	0.005	0.003	0.006
Fitter bias	0.0009	0.002	0.0009
Total systematic uncertainty	0.005	0.011	0.007
Statistical uncertainty	0.023	0.043	0.025

Table 13.8.: Summary table of systematic uncertainties on the lifetime ratio measurements, alt. selection.

Chapter 14.

Conclusions

In this chapter are summarised the main results on the lifetime and lifetime ratio measurements. In Table 14.1 the lifetime values extracted from the two dimensional fits for the two selections are given. All the obtained results are compatible with the world average, also given as a comparison. With the used amount of data the limiting factor is definitely the statistical uncertainty, but with the data collected in 2011 ($> 1 \text{ fb}^{-1}$) this will not be the case any more. LHCb will soon be able to get the world's best measurement of these three lifetimes.

CHANNEL	STD SEL. [ps]	ALT. SEL. [ps]	PDG [ps]
$B^+ \rightarrow J/\psi(1S) K^+$	$1.663 \pm 0.019 \pm 0.004$	$1.664 \pm 0.021 \pm 0.005$	1.641 ± 0.008
$B^0 \rightarrow J/\psi(1S) K^{*0}$	$1.528 \pm 0.030 \pm 0.005$	$1.523 \pm 0.029 \pm 0.006$	1.519 ± 0.007
$B_s^0 \rightarrow J/\psi(1S) \phi$	$1.453 \pm 0.058 \pm 0.005$	$1.491 \pm 0.059 \pm 0.009$	1.425 ± 0.041

Table 14.1.: Results of the two dimensional fit for the lifetime of the B-mesons in the proper time range $t_B \in [-2, 14]$ ps, where the first error is statistical and the second is systematic. The world average from PDG [34] is given as a comparison.

In Table 14.2 are summarised the lifetime ratios extracted from the two dimensional simultaneous fit, for the two selections. The HFAG [39] values are given for comparison, but it should be noted that the value they use for the B_s^0 lifetime is not the same (as mentioned in Chapter 10 and Section 6.3.2). The ratios are compatible with present measurements, and there is no sign of \mathcal{CPT} -violation in the $B^- - B^+$ system.

Existing \mathcal{CPT} tests performed with lifetime ratios seem to be uncommon, in Table 14.3 are presented some examples from [34]. The \mathcal{CPT} test performed in this study cannot

CHANNELS	STD SEL.	ALT. SEL.	HFAG
B^\pm / B^0	$1.094 \pm 0.023 \pm 0.006$	$1.096 \pm 0.023 \pm 0.005$	1.081 ± 0.006
B_s^0 / B^0	$0.957 \pm 0.043 \pm 0.009$	$0.984 \pm 0.043 \pm 0.011$	0.973 ± 0.015
B^- / B^+	$1.024 \pm 0.024 \pm 0.007$	$1.020 \pm 0.025 \pm 0.007$	—

Table 14.2.: Results of the two dimensional simultaneous fit for the lifetime ratio of the B-mesons in the proper time range $t_B \in [-2, 14]$ ps, where the first error is statistical and the second is systematic. The world average from HFAG [39] is given as a comparison.

compete with the world most precise \mathcal{CPT} test made with lifetime ratios (using μ^\pm), but seems to be the first one using B-mesons. The precision achieved in this study is comparable to the one reached in the existing results from baryon studies.

PARTICLE	PDG
μ^+ / μ^-	1.00002 ± 0.00008
π^+ / π^-	1.0006 ± 0.0007
K^+ / K^-	1.0010 ± 0.0009
Σ^+ / Σ^-	0.9994 ± 0.0012
$\Lambda / \bar{\Lambda}$	0.999 ± 0.009
Ω^- / Ω^+	1.00 ± 0.05
Ξ^- / Ξ^+	0.99 ± 0.07

Table 14.3.: Measured particle / antiparticle lifetime ratios from [34].

Appendix A.

Systematic uncertainty tables

The complete systematic uncertainty tables are presented in this chapter.

A.1. Lifetime measurements

In Tables A.1 to A.6 are presented all the systematics for the three channels and the two selections. In each table the fitted lifetime is given for:

- the nominal fit, i.e. the quoted value of the lifetime (Nominal),
- the fit using a Crystal Bass function to describe the signal mass shape (Crystall Ball sig),
- the fit using a second order polynomial to describe the background mass shape (Second order poly bkg),
- the fit where $\beta + \sigma_\beta$ is used instead of β (Increased β),
- the fit where $\beta - \sigma_\beta$ is used instead of β (Decreased β).

The absolute difference is also given.

SCENARIO	FITTED LIFETIME [ps]	ABS. DIFFERENCE [ps]
Nominal	1.663 ± 0.019	—
Crystall Ball sig	1.665 ± 0.020	0.002
Second order poly bgk	1.662 ± 0.019	0.001
Increased β	1.660 ± 0.019	0.003
Decreased β	1.666 ± 0.019	0.003

Table A.1.: Lifetime for $B^+ \rightarrow J/\psi(1S) K^+$, std. sel.

SCENARIO	FITTED LIFETIME [ps]	ABS. DIFFERENCE [ps]
Nominal	1.664 ± 0.021	—
Crystall Ball sig	1.667 ± 0.021	0.003
Second order poly bgk	1.664 ± 0.021	0.0005
Increased β	1.662 ± 0.021	0.002
Decreased β	1.668 ± 0.021	0.004

Table A.2.: Lifetime for $B^+ \rightarrow J/\psi(1S) K^+$, alt. sel.

SCENARIO	FITTED LIFETIME [ps]	ABS. DIFFERENCE [ps]
Nominal	1.528 ± 0.030	—
Crystall Ball sig	1.527 ± 0.030	0.001
Second order poly bgk	1.527 ± 0.030	0.001
Increased β	1.526 ± 0.030	0.002
Decreased β	1.531 ± 0.030	0.003

Table A.3.: Lifetime for $B^0 \rightarrow J/\psi(1S) K^{*0}$, std. sel.

SCENARIO	FITTED LIFETIME [ps]	ABS. DIFFERENCE [ps]
Nominal	1.523 ± 0.029	—
Crystall Ball sig	1.521 ± 0.030	0.002
Second order poly bgk	1.521 ± 0.029	0.002
Increased β	1.521 ± 0.029	0.002
Decreased β	1.526 ± 0.029	0.003

Table A.4.: Lifetime for $B^0 \rightarrow J/\psi(1S) K^{*0}$, alt. sel.

SCENARIO	FITTED LIFETIME [ps]	ABS. DIFFERENCE [ps]
Nominal	1.453 ± 0.058	—
Crystall Ball sig	1.456 ± 0.058	0.003
Second order poly bgk	1.451 ± 0.058	0.002
Increased β	1.450 ± 0.058	0.003
Decreased β	1.456 ± 0.058	0.003

Table A.5.: Lifetime for $B_s^0 \rightarrow J/\psi(1S) \phi$, std. sel.

SCENARIO	FITTED LIFETIME [ps]	ABS. DIFFERENCE [ps]
Nominal	1.491 ± 0.059	—
Crystall Ball sig	1.483 ± 0.059	0.008
Second order poly bgk	1.489 ± 0.058	0.002
Increased β	1.487 ± 0.058	0.004
Decreased β	1.495 ± 0.059	0.004

Table A.6.: Lifetime for $B_s^0 \rightarrow J/\psi(1S) \phi$, alt. sel.

A.2. Lifetime ratio measurements

In Tables A.7 to A.12 are presented all the systematics for the three ratios and the two selections. In each table the fitted ratio is given for:

- the nominal fit, i.e. the quoted value of the lifetime (Nominal),
- the fit using a Crystal Bass function to describe the signal mass shape (Crystall Ball sig),
- the fit using a second order polynomial to describe the background mass shape (Second order poly bgk),
- the fit where $\beta_1 + \sigma_{\beta_1}$ is used instead of β_1 and $\beta_2 + \sigma_{\beta_2}$ instead of β_2 (β_{++}),
- the fit where $\beta_1 + \sigma_{\beta_1}$ is used instead of β_1 and $\beta_2 - \sigma_{\beta_2}$ instead of β_2 (β_{+-}),
- the fit where $\beta_1 - \sigma_{\beta_1}$ is used instead of β_1 and $\beta_2 + \sigma_{\beta_2}$ instead of β_2 (β_{-+}),
- the fit where $\beta_1 - \sigma_{\beta_1}$ is used instead of β_1 and $\beta_2 - \sigma_{\beta_2}$ instead of β_2 (β_{--}),

The absolute difference is also given.

SCENARIO	FITTED RATIO	ABS. DIFFERENCE
Nominal	1.094 ± 0.023	—
Crystall Ball sig	1.089 ± 0.023	0.005
Second order poly bgk	1.095 ± 0.023	0.001
β_{++}	1.094 ± 0.023	0.0001
β_{+-}	1.095 ± 0.025	0.001
β_{-+}	1.091 ± 0.023	0.003
β_{--}	1.091 ± 0.023	0.003

Table A.7.: Lifetime ratio for B^\pm and B^0 , std. sel.

SCENARIO	FITTED RATIO	ABS. DIFFERENCE
Nominal	1.096 ± 0.023	—
Crystall Ball sig	1.097 ± 0.024	0.001
Second order poly bgk	1.097 ± 0.023	0.001
β_{++}	1.093 ± 0.025	0.003
β_{+-}	1.098 ± 0.023	0.005
β_{-+}	1.092 ± 0.023	0.004
β_{--}	1.095 ± 0.025	0.001

Table A.8.: Lifetime ratio for B^\pm and B^0 , alt. sel.

SCENARIO	FITTED RATIO	ABS. DIFFERENCE
Nominal	0.957 ± 0.043	—
Crystall Ball sig	0.958 ± 0.043	0.001
Second order poly bgk	0.958 ± 0.043	0.001
β_{++}	0.957 ± 0.043	0.0004
β_{+-}	0.961 ± 0.042	0.004
β_{-+}	0.956 ± 0.043	0.001
β_{--}	0.959 ± 0.043	0.002

Table A.9.: Lifetime ratio for B_s^0 and B^0 , std. sel.

SCENARIO	FITTED RATIO	ABS. DIFFERENCE
Nominal	0.984 ± 0.043	—
Crystall Ball sig	0.975 ± 0.043	0.009
Second order poly bgk	0.984 ± 0.043	0.0001
β_{++}	0.985 ± 0.044	0.001
β_{+-}	0.987 ± 0.044	0.003
β_{-+}	0.982 ± 0.040	0.002
β_{--}	0.986 ± 0.041	0.002

Table A.10.: Lifetime ratio for B_s^0 and B^0 , alt. sel.

SCENARIO	FITTED RATIO	ABS. DIFFERENCE
Nominal	1.024 ± 0.024	—
Crystall Ball sig	1.024 ± 0.023	0.0004
Second order poly bgk	1.025 ± 0.024	0.001
β_{++}	1.024 ± 0.024	0.0001
β_{+-}	1.029 ± 0.024	0.005
β_{-+}	1.018 ± 0.024	0.006
β_{--}	1.024 ± 0.024	0.0004

Table A.11.: Lifetime ratio for B^- and B^+ , Std. sel.

SCENARIO	FITTED RATIO	ABS. DIFFERENCE
Nominal	1.020 ± 0.025	—
Crystall Ball sig	1.023 ± 0.026	0.003
Second order poly bgk	1.020 ± 0.026	0.0002
β_{++}	1.020 ± 0.025	0.0002
β_{+-}	1.025 ± 0.026	0.005
β_{-+}	1.014 ± 0.025	0.006
β_{--}	1.020 ± 0.026	0.0001

Table A.12.: Lifetime ratio for B^- and B^+ , alt. sel.

Appendix B.

Additional plots

In this chapter are presented plots resulting from the two dimensional fits for the lifetime. In Appendix B.1 are shown the plots for the lifetime and in Appendix B.2 the plots related to the lifetime ratio measurements. The fitted function are projected on the plots, always with the same colour convention: blue is the total PDF, dashed red is the background PDF and dashed green the signal PDF.

B.1. Lifetime fits

In this section are presented the plots resulting from the fit for the lifetime. The seen plots are the projection of the mass PDF, and three projections of the time PDF: on the signal region (defined by a 3σ window around the peak), the low and high B mass sidebands (defined to be 5σ away from the peak). The $B^+ \rightarrow J/\psi(1S) K^+$ results are shown on Figure B.1 and Figure B.2 for the std. and alt. selections respectively. Similarly the $B^0 \rightarrow J/\psi(1S) K^{*0}$ and $B_s^0 \rightarrow J/\psi(1S) \phi$ are presented on Figure B.3, Figure B.4, Figure B.5 and Figure B.6.

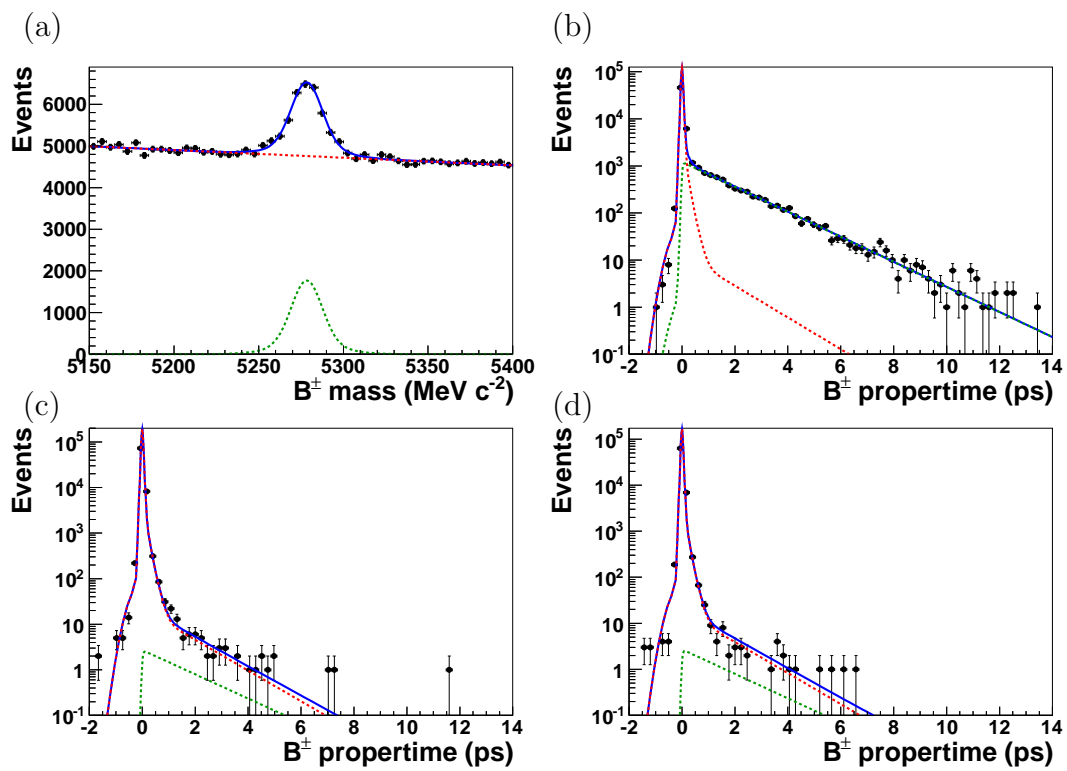


Figure B.1.: Projections of the two dimensional fit for the lifetime in $B^+ \rightarrow J/\psi(1S) K^+$, std. selection. Subfigure (a) shows the mass distribution, (b) shows the proper time distribution in the signal region, (c) the proper time distribution in the low mass sideband and (d) the proper time distribution in the high mass sideband.

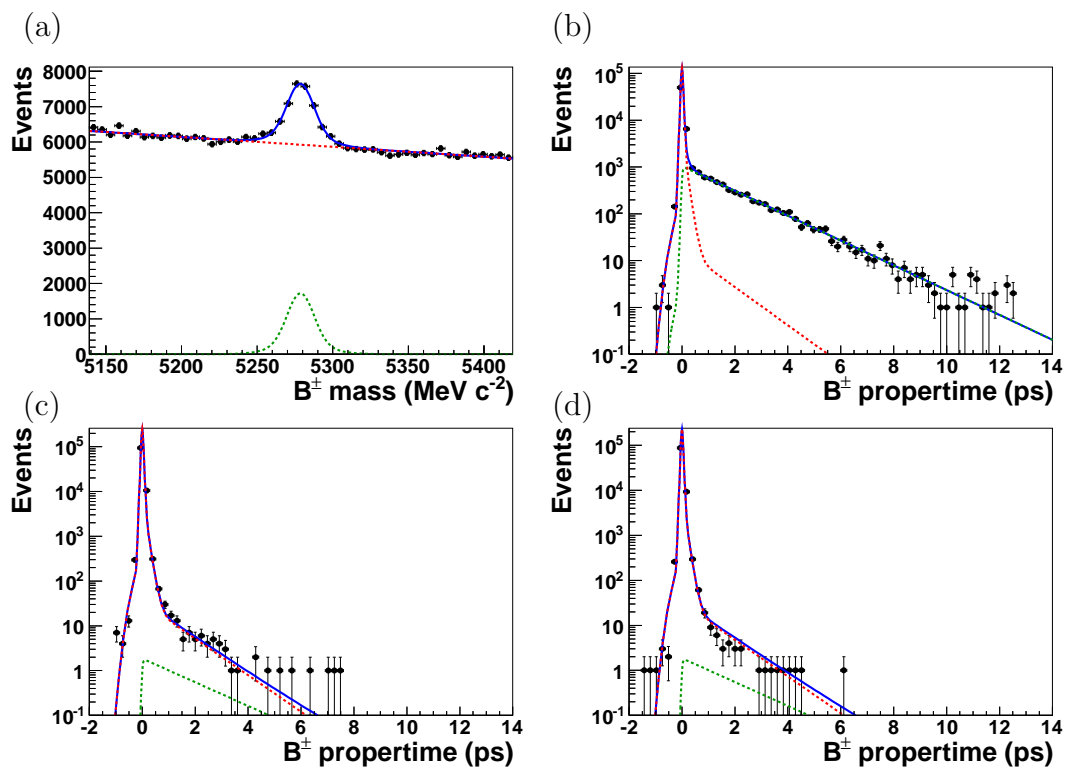


Figure B.2.: Projections of the two dimensional fit for the lifetime in $B^+ \rightarrow J/\psi(1S) K^+$, alt. selection. Subfigure (a) shows the mass distribution, (b) shows the proper time distribution in the signal region, (c) the proper time distribution in the low mass sideband and (d) the proper time distribution in the high mass sideband.

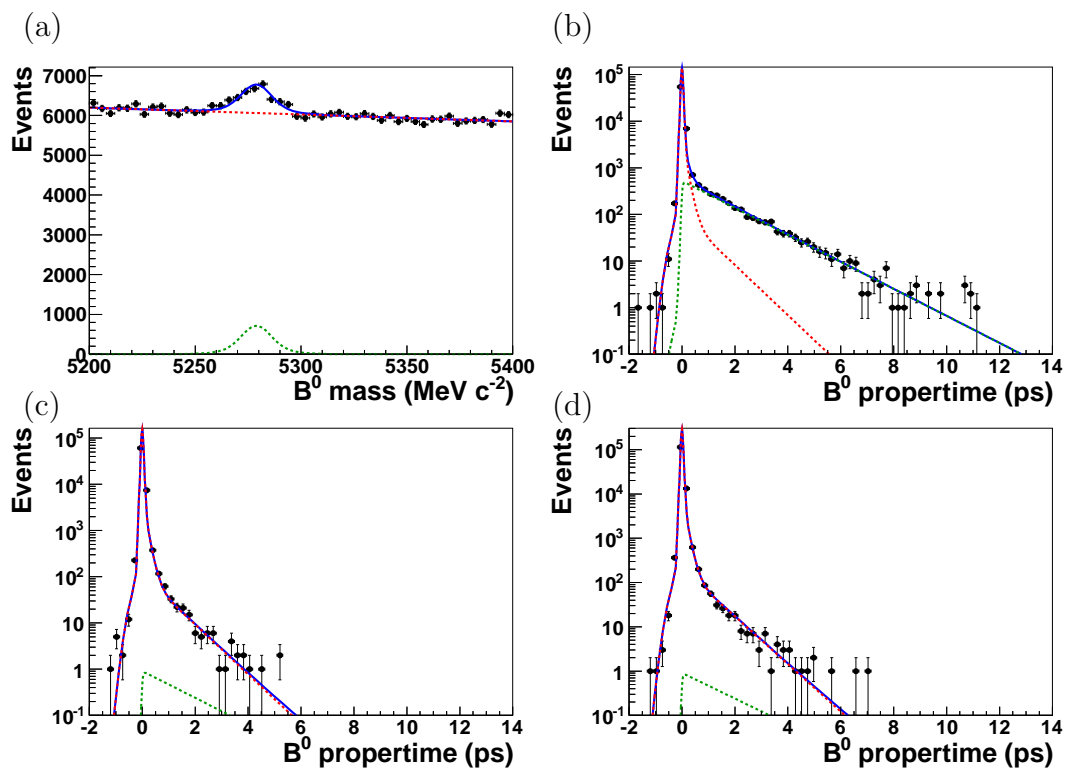


Figure B.3.: Projections of the two dimensional fit for the lifetime in $B^0 \rightarrow J/\psi(1S) K^{*0}$, std. selection. Subfigure (a) shows the mass distribution, (b) shows the proper time distribution in the signal region, (c) the proper time distribution in the low mass sideband and (d) the proper time distribution in the high mass sideband.

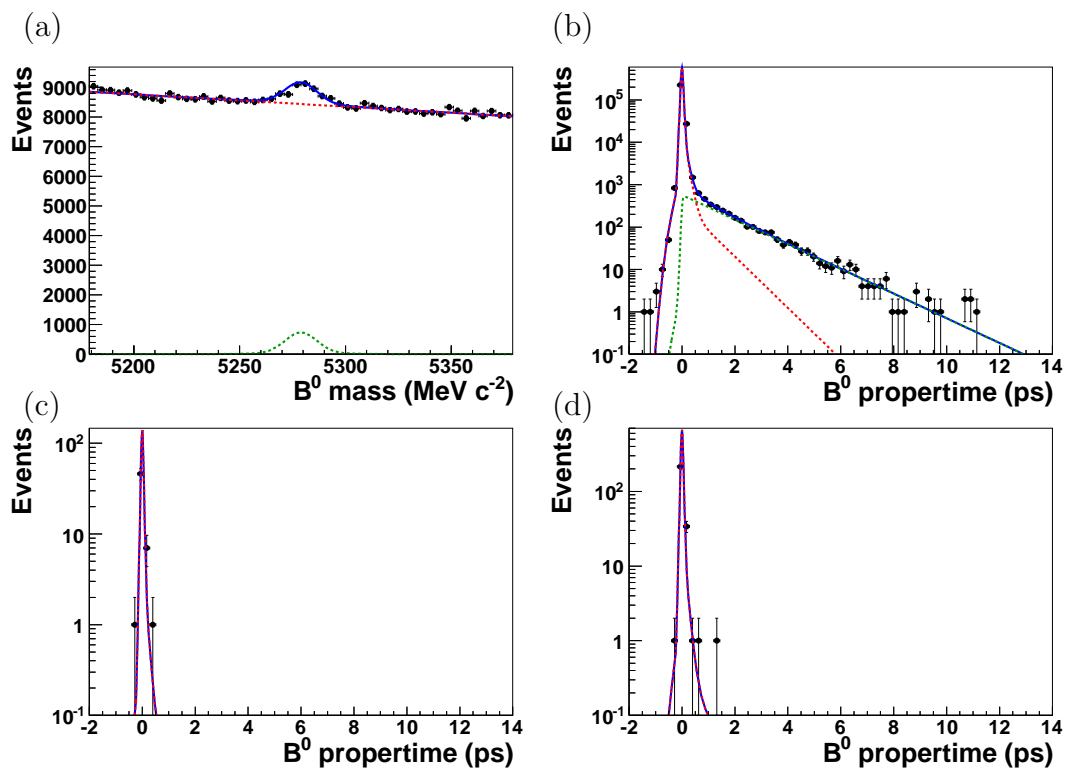


Figure B.4.: Projections of the two dimensional fit for the lifetime in $B^0 \rightarrow J/\psi(1S) K^{*0}$, alt. selection. Subfigure (a) shows the mass distribution, (b) shows the proper time distribution in the signal region, (c) the proper time distribution in the low mass sideband and (d) the proper time distribution in the high mass sideband.

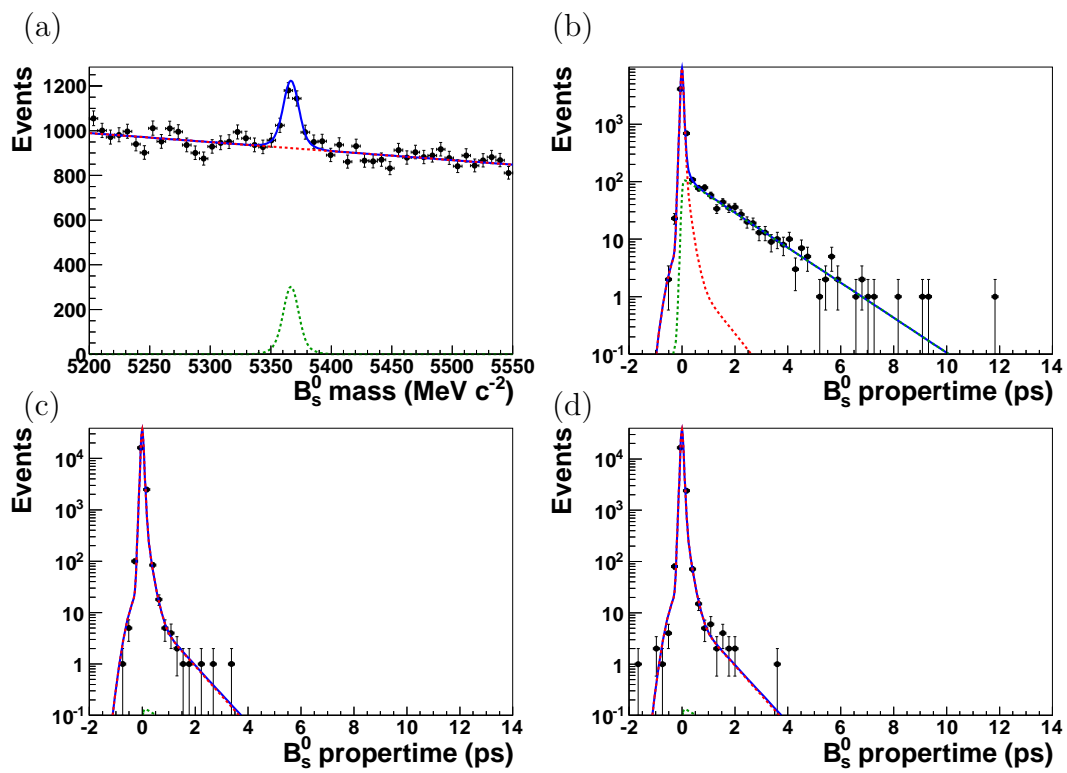


Figure B.5.: Projections of the two dimensional fit for the lifetime in $B_s^0 \rightarrow J/\psi(1S)\phi$, std. selection. Subfigure (a) shows the mass distribution, (b) shows the proper time distribution in the signal region, (c) the proper time distribution in the low mass sideband and (d) the proper time distribution in the high mass sideband.

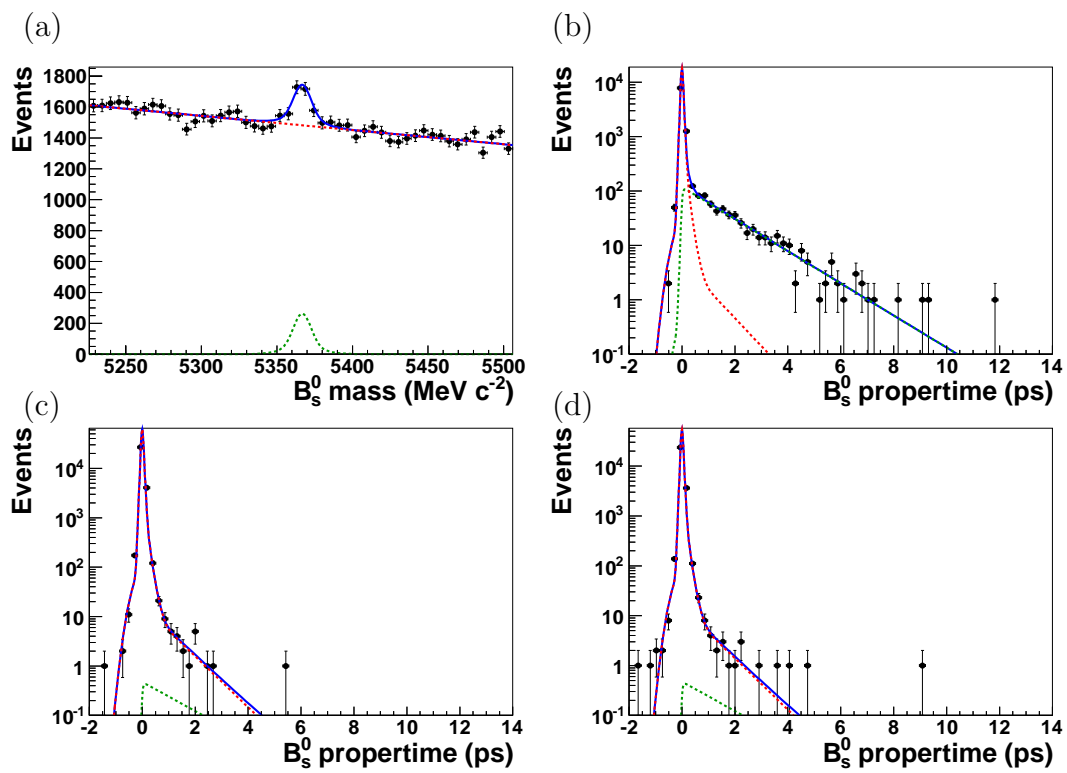


Figure B.6.: Projections of the two dimensional fit for the lifetime in $B_s^0 \rightarrow J/\psi(1S) \phi$, alt. selection. Subfigure (a) shows the mass distribution, (b) shows the proper time distribution in the signal region, (c) the proper time distribution in the low mass sideband and (d) the proper time distribution in the high mass sideband.

B.2. Lifetime ratio fits

In this section are presented the plots resulting from the fit for the lifetime ratios. The seen plots are the projection of the mass PDF, and the projections of the time PDF.

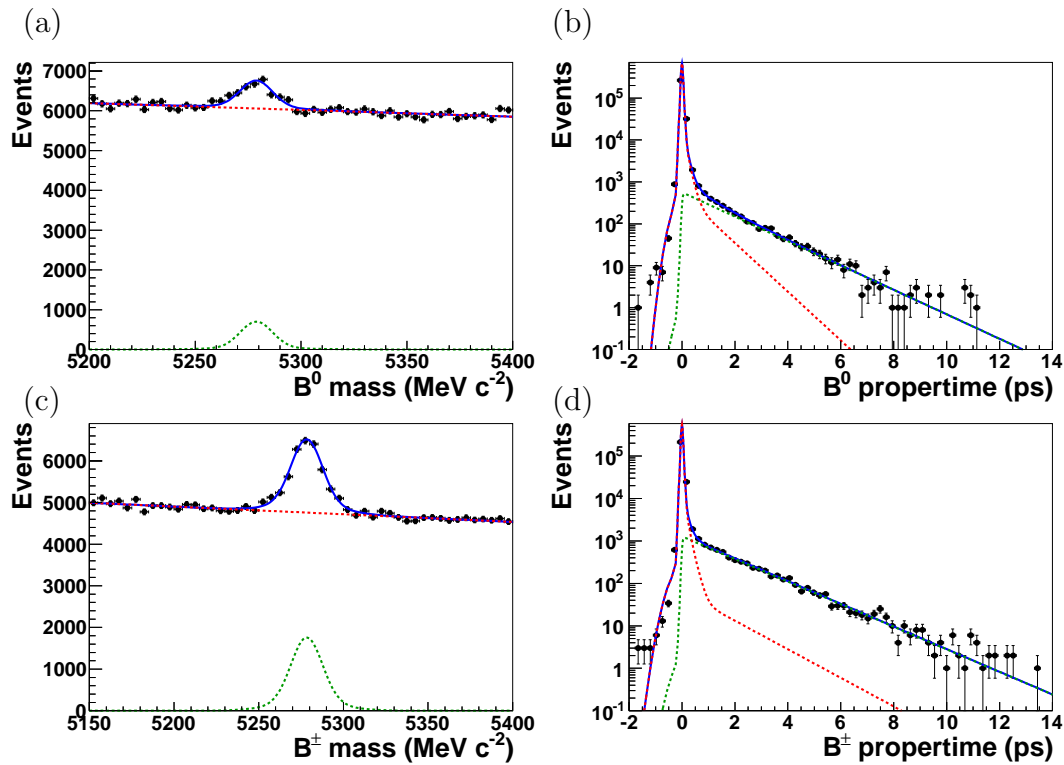


Figure B.7.: Projections of the two dimensional simultaneous fit for the B^\pm / B^0 lifetime ratio, std. selection. Subfigure (a) shows the mass distribution of B^0 , (b) shows the B^0 proper time distribution in the full mass window, (c) the mass distribution of B^\pm , (d) shows the B^\pm proper time distribution in the full mass window.

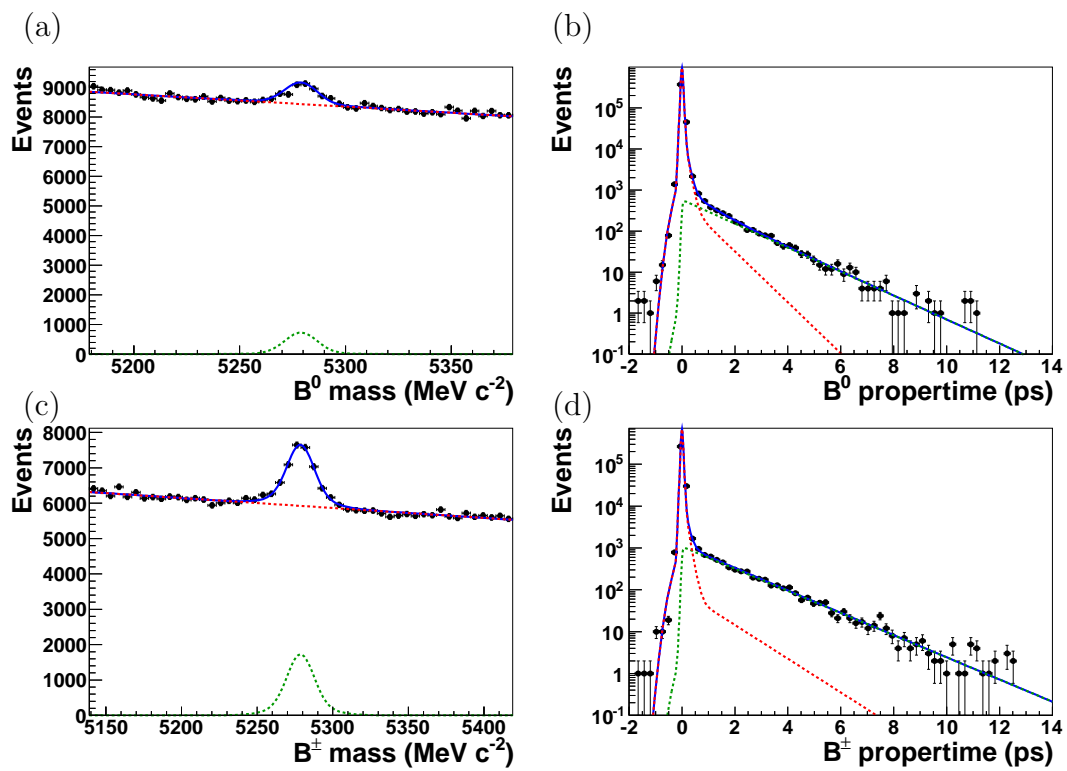


Figure B.8.: Projections of the two dimensional simultaneous fit for the B^\pm / B^0 lifetime ratio, alt. selection. Subfigure (a) shows the mass distribution of B^0 , (b) shows the B^0 proper time distribution in the full mass window, (c) the mass distribution of B^\pm , (d) shows the B^\pm proper time distribution in the full mass window.

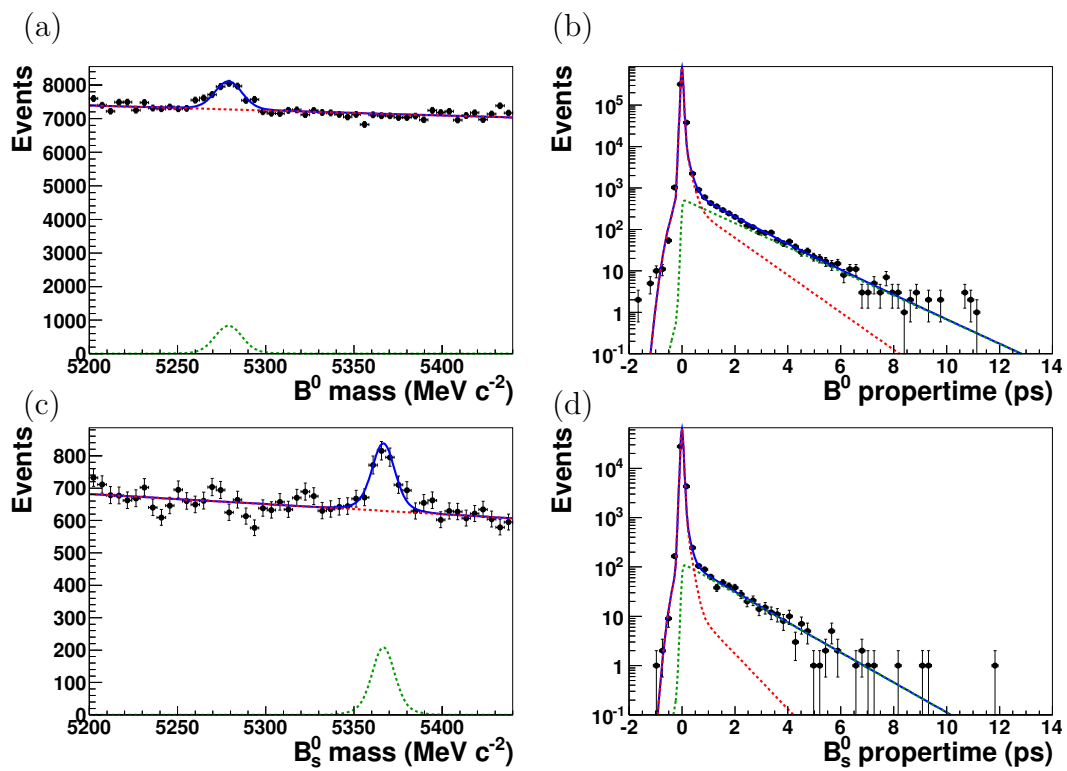


Figure B.9.: Projections of the two dimensional simultaneous fit for the B_s^0 / B^0 lifetime ratio, std. selection. Subfigure (a) shows the mass distribution of B^0 , (b) shows the B^0 proper time distribution in the full mass window, (c) the mass distribution of B_s^0 , (d) shows the B_s^0 proper time distribution in the full mass window.

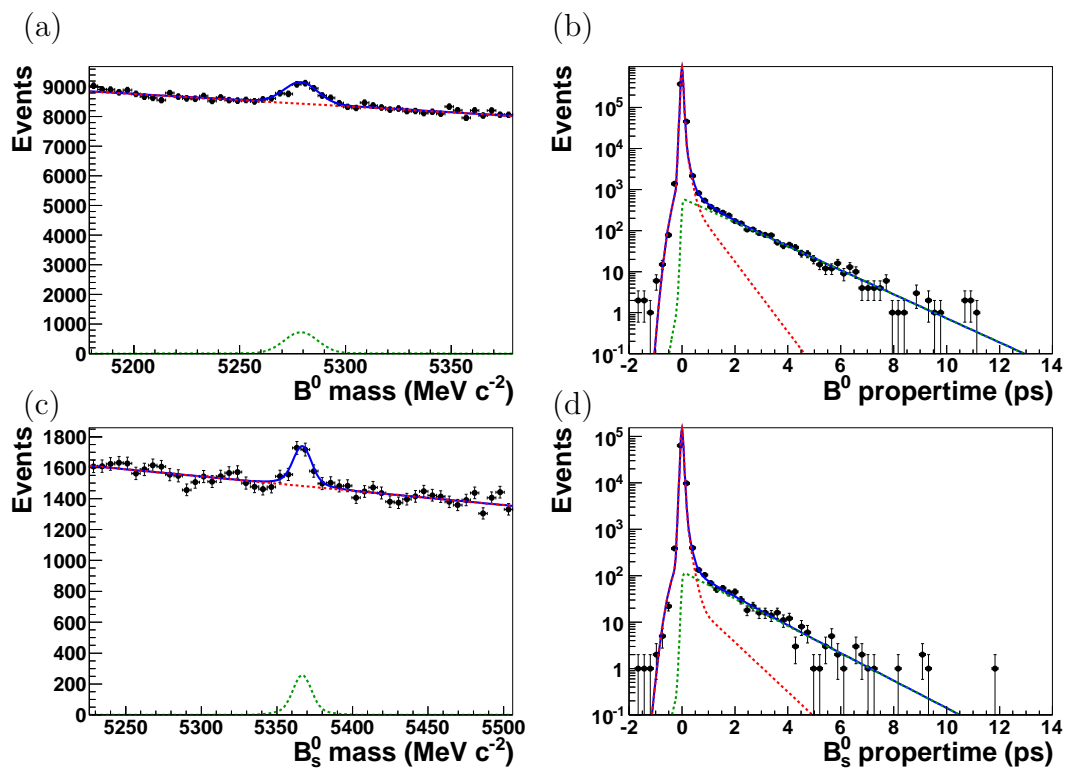


Figure B.10.: Projections of the two dimensional simultaneous fit for the B_s^0/B^0 lifetime ratio, alt. selection. Subfigure (a) shows the mass distribution of B^0 , (b) shows the B^0 proper time distribution in the full mass window, (c) the mass distribution of B_s^0 , (d) shows the B_s^0 proper time distribution in the full mass window.

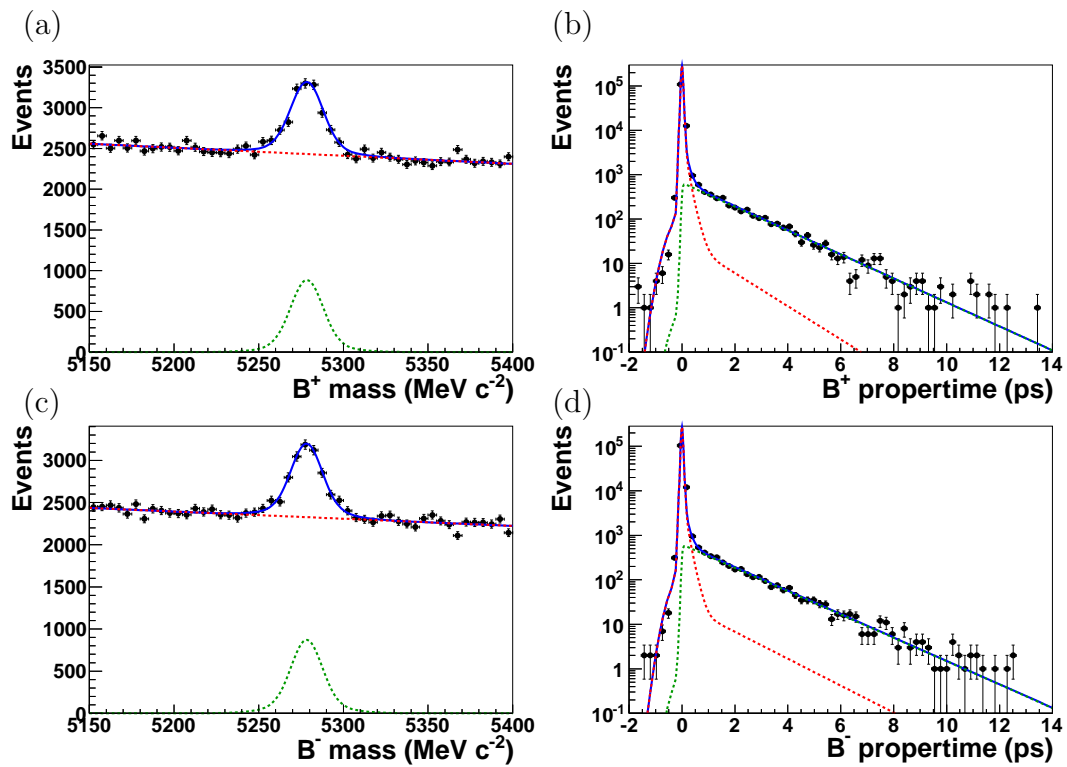


Figure B.11.: Projections of the two dimensional simultaneous fit for the B^- / B^+ lifetime ratio, std. selection. Subfigure (a) shows the mass distribution of B^+ , (b) shows the B^+ proper time distribution in the full mass window, (c) the mass distribution of B^- , (d) shows the B^- proper time distribution in the full mass window.

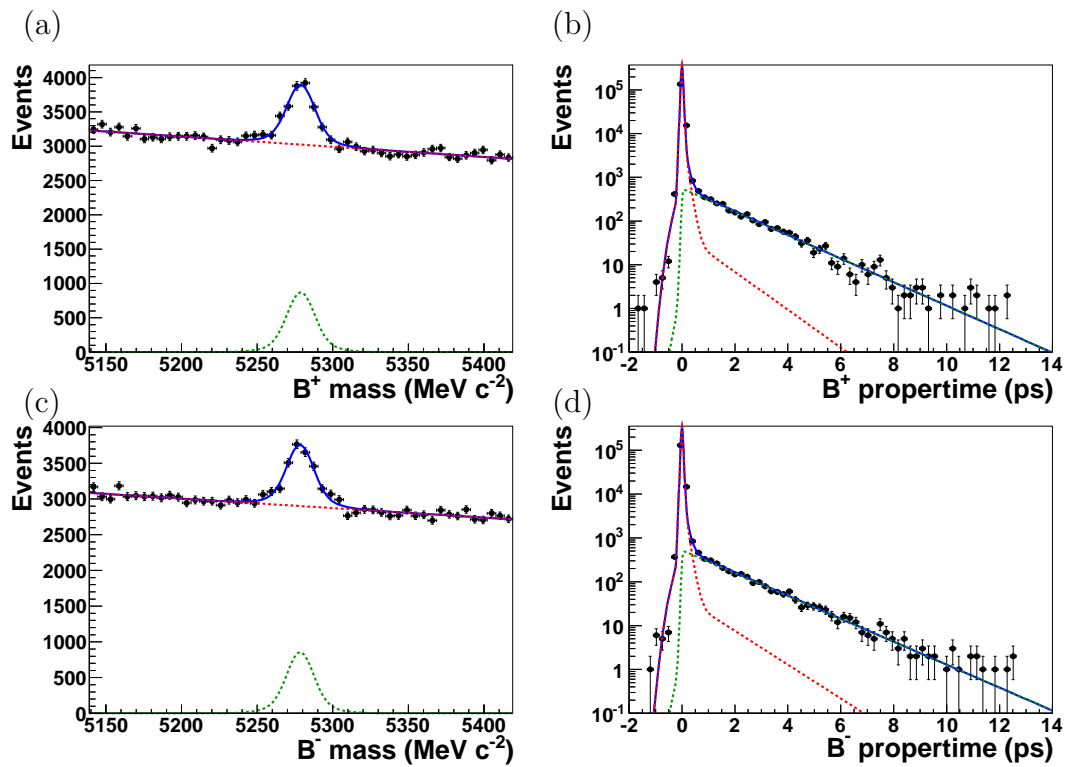


Figure B.12.: Projections of the two dimensional simultaneous fit for the B^- / B^+ lifetime ratio, alt. selection. Subfigure (a) shows the mass distribution of B^+ , (b) shows the B^+ proper time distribution in the full mass window, (c) the mass distribution of B^- , (d) shows the B^- proper time distribution in the full mass window.

Appendix C.

Various mass plots

In this chapter are presented the mass plots of the reconstructed daughters of the studied B-mesons. In Appendix C.1 are shown the J/ψ mass plots from the $B^+ \rightarrow J/\psi(1S) K^+$ channel for the two selections. Appendix C.2 shows the J/ψ and K^{*0} plots for $B^0 \rightarrow J/\psi(1S) K^{*0}$, and in Appendix C.3 are presented the J/ψ and ϕ plots for $B_s^0 \rightarrow J/\psi(1S) \phi$. The fitted function are projected on the plots, always with the same colour convention: blue is the total PDF, dashed red is the background PDF and dashed green the signal PDF. The proper time range is always $t_B \in [-2, 14]$ ps and the mass windows correspond to the ones used to get the results from Table 12.1.

C.1. $B^+ \rightarrow J/\psi(1S) K^+$

A double Gaussian function is used to fit the J/ψ mass shape and a linear function is used to model the background.

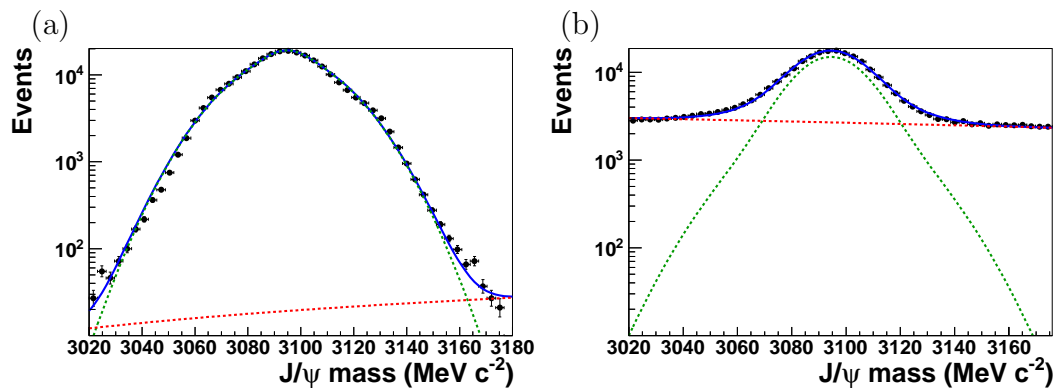


Figure C.1.: J/ψ mass distribution from $B^+ \rightarrow J/\psi(1S) K^+$, (a) is the std. selection and (b) is the alt. one.

C.2. $B^0 \rightarrow J/\psi(1S) K^{*0}$

A double Gaussian function is used to fit the J/ψ mass shape and a linear function is used to model the background (Figure C.4). The K^{*0} mass on Figure C.3 is fitted with a single Gaussian and a linear background function.

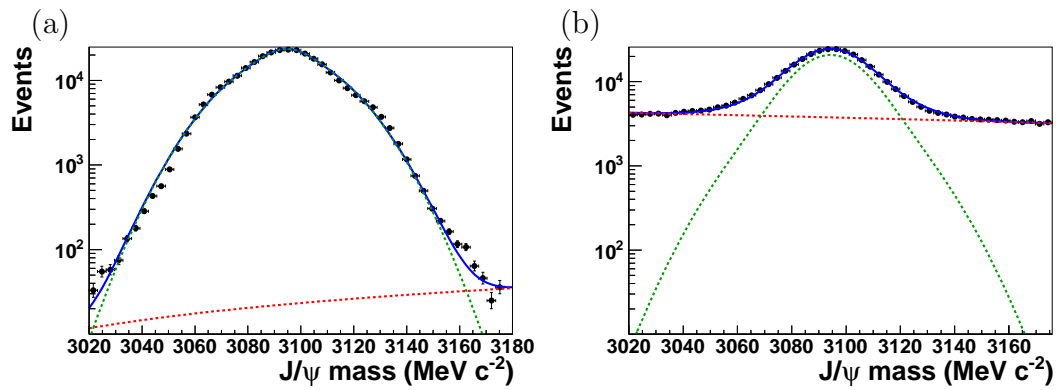


Figure C.2.: J/ψ mass distribution from $B^0 \rightarrow J/\psi(1S) K^{*0}$, (a) is the std. selection and (b) is the alt. one.

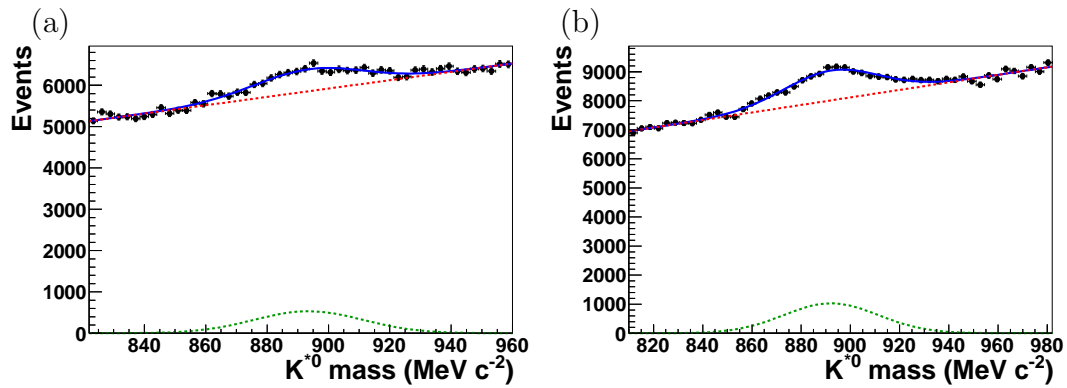


Figure C.3.: K^{*0} mass distribution from $B^0 \rightarrow J/\psi(1S) K^{*0}$, (a) is the std. selection and (b) is the alt. one.

C.3. $B_s^0 \rightarrow J/\psi(1S) \phi$

In Figure C.4 a double Gaussian function is used to fit the J/ψ mass shape and a linear function is used to model the background. The ϕ mass on Figure C.5 is fitted with a single Gaussian and a parabolic background function.

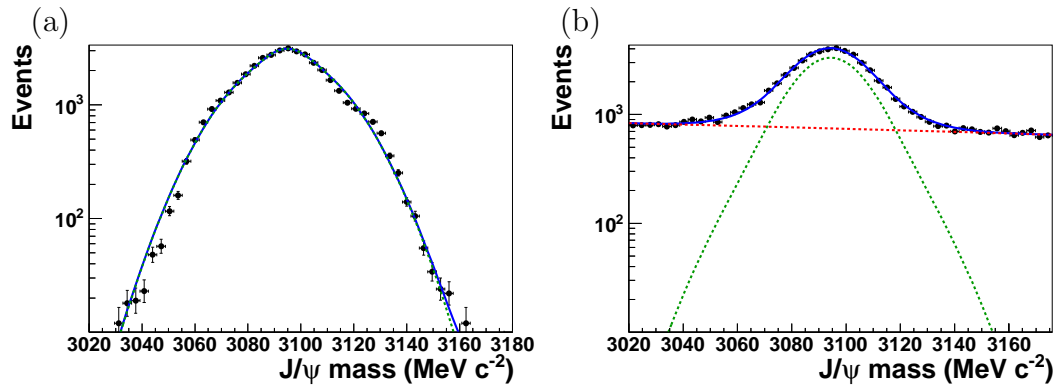


Figure C.4.: J/ψ mass distribution from $B_s^0 \rightarrow J/\psi(1S) \phi$, (a) is the std. selection and (b) is the alt. one.

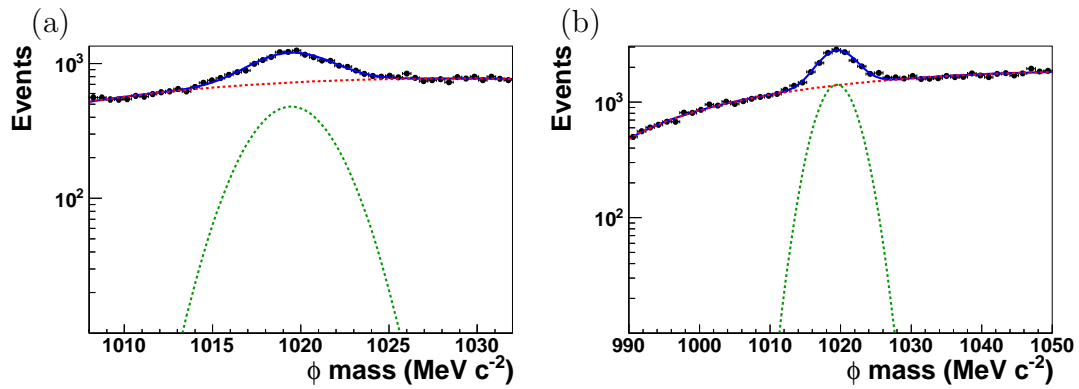


Figure C.5.: ϕ mass distribution from $B_s^0 \rightarrow J/\psi(1S) \phi$, (a) is the std. selection and (b) is the alt. one.

Appendix D.

Resolution plots

In this chapter are presented the plots of the prompt peak regions obtained from the lifetime fit in the full proper time range $t_B \in [-2, 14]$ ps. $B^+ \rightarrow J/\psi(1S) K^+$ plots are shown in Figure D.1, $B^0 \rightarrow J/\psi(1S) K^{*0}$ on Figure D.2 and $B_s^0 \rightarrow J/\psi(1S) \phi$ on Figure D.3. The fitted functions are projected on the plots, always with the same colour convention: blue is the total PDF, dashed red is the background PDF and dashed green the signal PDF.

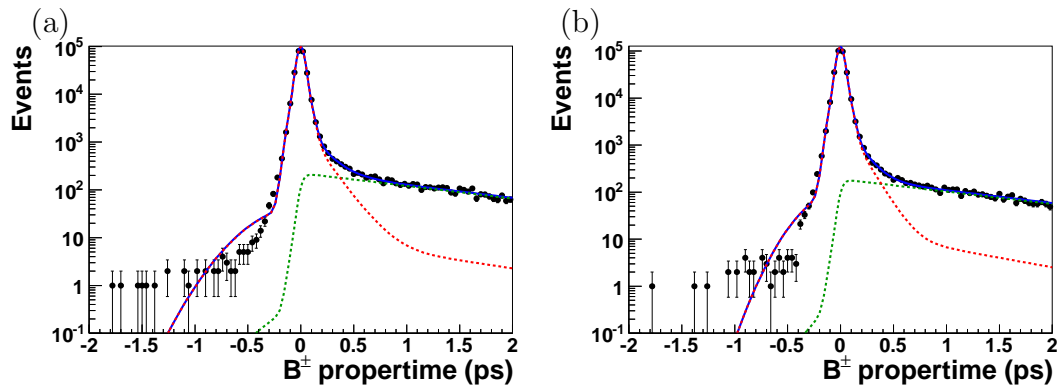


Figure D.1.: Zoom on the prompt peak region, $B^+ \rightarrow J/\psi(1S) K^+$. Subfigure (a) shows the std. selection and (b) the alt. selection.

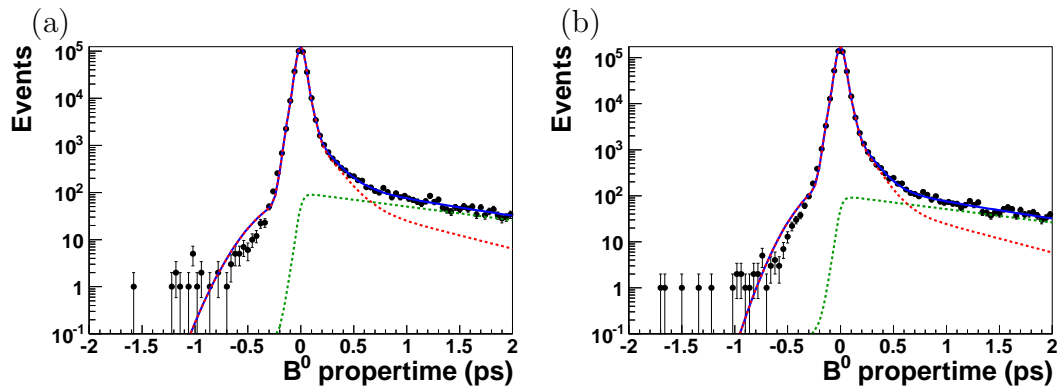


Figure D.2.: Zoom on the prompt peak region, $B^0 \rightarrow J/\psi(1S) K^{*0}$. Subfigure (a) shows the std. selection and (b) the alt. selection.

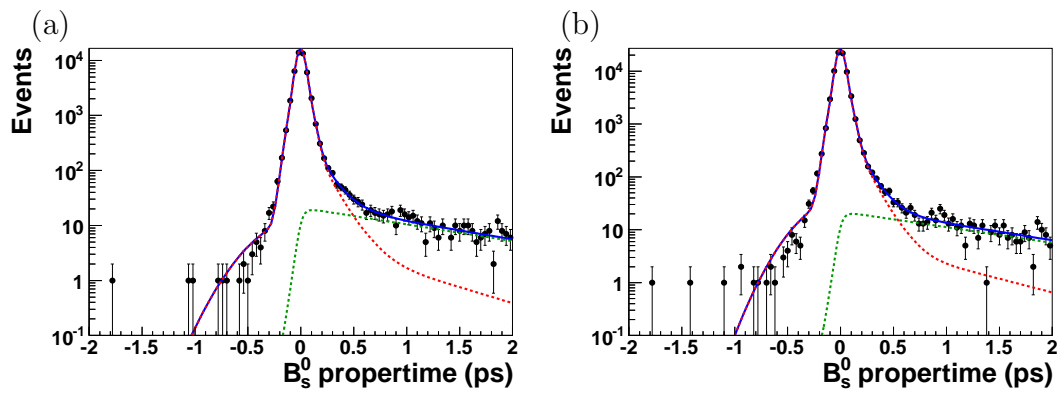


Figure D.3.: Zoom on the prompt peak region, $B_s^0 \rightarrow J/\psi(1S) \phi$. Subfigure (a) shows the std. selection and (b) the alt. selection.

Bibliography

- [1] Lyndon Evans and Philip Bryant, “LHC Machine,” *Journal of Instrumentation*, vol. 3, no. 08, p. S08001, 2008.
- [2] J. R. J. Bennett et al, “Design Concept For a 100-GeV $e^+ e^-$ Storage Ring (LEP),” Tech. Rep. CERN-77-14, CERN, 1977.
- [3] Brüning, Oliver Sim Ed and Collier, Paul Ed and Lebrun, P Ed and Myers, Stephen Ed and Ostojic, Ranko Ed and Poole, John Ed and Proudlock, Paul Ed, *LHC Design report*, vol. v. 1. CERN Libraries, 2004.
- [4] “Prompt charm production in p p collisions at $\sqrt{s} = 7$ TeV,” Dec 2010.
- [5] The LHCb collaboration, “Measurement of $\sigma(\text{pp} \rightarrow \text{b}\bar{\text{b}} \text{X})$ at $\sqrt{s} = 7$ TeV in the forward region. oai:cds.cern.ch:1291838,” *Phys. Lett. B*, vol. 694, pp. 209–216. 16 p, Sep 2010. Comments: 11 pages, 5 figures, submitted to Physics Lett. B.
- [6] LHCb, S. Amato et al, “LHCb Technical Proposal,” Tech. Rep. CERN-LHCC-98-4, CERN, 1998.
- [7] The LHCb collaboration et al, “The LHCb Detector at the LHC,” *Journal of Instrumentation*, vol. 3, no. 08, p. S08005, 2008.
- [8] LHCb, “Reoptimized Detector Design and Performance,” Tech. Rep. CERN-LHCC-2003-030, CERN, 2003.
- [9] “PVSS-2 Prozessvisualisierungs- und Steuerungs-System) SCADA tool.” <http://www.pvss.com>.
- [10] “PVSS service at CERN.” <http://j2eeps.cern.ch/wikis/display/EN/PVSS+Service>.
- [11] “Qt : a cross platform application and UI framework.” <http://qt.nokia.com/>.
- [12] Myers, D. R., “The LHC experiments Joint COntrol Project,” pp. 633–635, 1999.

- [13] Löchner, S and Schmelling, M, “The Beetle Reference Manual - chip version 1.3, 1.4 and 1.5,” Tech. Rep. LHCb-2005-105. CERN-LHCb-2005-105, CERN, Geneva, Nov 2006.
- [14] Legger, F and Bay, A and Haefeli, G and Locatelli, L, “TELL1 : development of a common readout board for LHCb,” Tech. Rep. LHCb-2004-100. CERN-LHCb-2004-100. 1-2, CERN, Geneva, Nov 2004.
- [15] Keune, Anne and Lingemann, Joschka and Needham, Matthew, “Emulation of the ST TELL1 Algorithms,” Tech. Rep. LHCb-INT-2011-040. CERN-LHCb-INT-2011-040, CERN, Geneva, Sep 2011.
- [16] Szumlak, T and Parkes, C, “Description of the Vetra Project and its Application for the VELO Detector,” Tech. Rep. LHCb-2008-022. CERN-LHCb-2008-022, CERN, Geneva, May 2008.
- [17] Luisier, J, “Configuration of TELL1 boards from XML database with PVSS,” Tech. Rep. LHCb-INT-2011-017. CERN-LHCb-INT-2011-017, CERN, Geneva, May 2011.
- [18] Haefeli, G, *Contribution to the development of the acquisition electronics for the LHCb experiment*. PhD thesis, EPFL Lausanne, Geneva, 2004.
- [19] “XML DOM Tutorial.” <http://www.w3schools.com/dom/default.asp>.
- [20] Haefeli, G., “tell1lib documentation.” http://lphe.epfl.ch/tell1/tell1lib_c-code.htm.
- [21] Potterat, Cédric and Bay, A, *Direct Search for Standard Model-Like Higgs Boson and Software Integration of Data Acquisition Cards*. PhD thesis, Lausanne, EPFL, Lausanne, 2010. Presented on 06 May 2010.
- [22] Haefeli, G. and Bay, A. and Gong, A. and Gong, H. and Muecke, M. and Neufeld, N. and Schneider, O., “The LHCb DAQ interface board TELL1,” *Nuclear Instruments and Methods in Physics Research A*, vol. 560, pp. 494–502, May 2006.
- [23] Needham, M, “Track Reconstruction in the LHCb Inner Tracker,” Tech. Rep. LHCb-PUB-2009-005. CERN-LHCb-PUB-2009-005, CERN, Geneva, May 2009.
- [24] Needham, M, “Identification of Ghost Tracks using a Likelihood Method,” Tech. Rep. LHCb-2008-026. CERN-LHCb-2008-026. LPHE-2008-004, CERN, Geneva, May 2008.
- [25] Nicolas, L and Needham, M, “Alignment of the Inner Tracker Stations Using

- First Data,” Tech. Rep. LHCb-PUB-2009-012. CERN-LHCb-PUB-2009-012, CERN, Geneva, Nov 2009.
- [26] Needham, M and Luisier, J, “Measurement of the Inner Tracker Efficiency,” Tech. Rep. LHCb-INT-2010-031. CERN-LHCb-INT-2010-031, CERN, Geneva, Jul 2010.
- [27] Salam, Abdus, “Weak and Electromagnetic Interactions,” pp. 367–377, 1968.
- [28] Glashow, S.L., “Partial Symmetries of Weak Interactions,”
- [29] Weinberg, Steven, “A Model of Leptons,” *Phys.Rev.Lett.*, vol. 19, pp. 1264–1266, 1967.
- [30] Adeva, B et al, “Roadmap for selected key measurements of LHCb,” Dec 2009. Comments: 379 pages.
- [31] Charles, J. and others, “CP violation and the CKM matrix: Assessing the impact of the asymmetric B factories,” *Eur. Phys. J.*, vol. C41, pp. 1–131, 2005.
- [32] Giurgiu, Gavril, “New Measurement of the B_s^0 Mixing Phase at CDF,” *PoS*, vol. ICHEP2010, p. 236, 2010.
- [33] Aaij, R et al, “Tagged time-dependent angular analysis of $B_s^0 \rightarrow J/\psi(1S) \phi$ decays with the 2010 LHCb data,” May 2011. LHCb-CONF-2011-006.
- [34] K. Nakamura et al (Particle Data Group), “The Review of Particle Physics,” *J. Phys. G* 37, 2010.
- [35] Grozin, A.G., “Introduction to the heavy quark effective theory. part 1,” 1992.
- [36] Neubert, Matthias, “B decays and the heavy-quark expansion,” *Adv. Ser. Direct. High Energy Phys.*, vol. 15, pp. 239–293, 1998.
- [37] Bellini, G. and Bigi, Ikaros I.Y. and Dornan, P.J., “Lifetimes of charm and beauty hadrons,” *Phys.Rept.*, vol. 289, pp. 1–155, 1997.
- [38] Tarantino, Cecilia, “Beauty hadron lifetimes and B meson CP violation parameters from lattice QCD,” *Eur.Phys.J.*, vol. C33, pp. S895–S899, 2004.
- [39] Asner, D et al, “Averages of b-hadrons, c-hadrons, and τ -lepton Properties,” 2010.
- [40] “The BRUNEL project.” <http://lhcb-release-area.web.cern.ch/LHCb-release-area/DOC/brunel/>.

-
- [41] “The DAVINCI project.” <http://lhcb-release-area.web.cern.ch/LHCb-release-area/DOC/davinci/>.
- [42] “Dirac: Community grid solution.” <http://diracgrid.org/>.
- [43] “Root: A data analysis framework.” <http://root.cern.ch/drupal/>.
- [44] Panman, J, “The LHCb Upgrade,” Aug 2011.
- [45] Aaij, R and Amhis, Y and Cowan, G and van Eijk, D and Hulsbergen, W and Khanji, B and Lefevre, R and Leroy, O and Luisier, J and Maurice, E and Muster, B and Nakada, T and Raven, G and Schneider, O and Xie, Y, “Selections and lifetime measurements for exclusive $b \rightarrow J/\psi(1S) X$ decays with $J/\psi(1S) \rightarrow \mu^+ \mu^-$ with 2010 data,” Apr 2011. LHCb-CONF-2011-001.
- [46] The DecayTreeFitter was originally developed by Wouter Hulsbergen for the Babar experiment and imported to LHCb analysis. See <https://twiki.cern.ch/twiki/bin/view/LHCb/DecayTreeFitter>.
- [47] H. Dijkstra, “Measuring Lifetime Bias in Data.” August 2011.
- [48] O. Callot, “VELO tracking at large IP.” October 2011.
- [49] Needham, M, “Momentum scale calibration with first LHCb data,” Tech. Rep. LHCb-INT-2011-012. CERN-LHCb-INT-2011-012, CERN, Geneva, Apr 2011.

List of Figures

1.1.	LEP and LHC underground structures	6
1.2.	LHC injection chain cite	7
1.3.	Distribution function of number of events with 0, 1, 2, 3 and 4 interaction per bunch crossing.	10
1.4.	$b\bar{b}$ production at the LHC	11
2.1.	Polar angle distribution of produced $b\bar{b}$ pairs	14
2.2.	The LHCb detector	15
2.3.	VELO r and ϕ sensors	18
2.4.	TT layout	19
2.5.	Layout of the IT station 2 layer x	20
3.1.	Noise pattern in an IT TELL1 board	30
3.2.	CMS noise in an IT TELL1 board	35
4.1.	User interface of the fwTell1XML component	40
5.1.	Example of TED event in IT	52
5.2.	Efficiency vs. window size for IT2CSideU layer	54
5.3.	Comparison of efficiency curve with and without isolation criteria applied	55
5.4.	Efficiencies per sector in IT, February 2010's data	57
5.5.	Beetle pulse shape	59

5.6. Layer spillover efficiencies	59
5.7. Efficiency vs confirmation threshold, IT2BottomX1	60
5.8. Efficiency vs confirmation threshold, IT3CSideU	61
5.9. Spillover efficiency vs confirmation threshold, IT2BottomX1	62
5.10. Spillover efficiency vs confirmation threshold, IT3CSideX2	63
5.11. Layer spillover efficiencies, additional cut applied	63
8.1. Triggers flowchart	79
9.1. Distribution of events rejected by next best χ_{IP}^2 cut	89
9.2. Distribution of events rejected by best candidate selection	90
9.3. Mass distribution of truth-matched selected $B^+ \rightarrow J/\psi(1S) K^+$ events . . .	94
9.4. Mass distribution of truth-matched selected $B^0 \rightarrow J/\psi(1S) K^{*0}$ events . . .	94
9.5. Mass distribution of truth-matched selected $B_s^0 \rightarrow J/\psi(1S) \phi$ events	95
9.6. Proper time resolution of truth-matched selected $B^+ \rightarrow J/\psi(1S) K^+$ events	96
9.7. Proper time resolution of truth-matched selected $B^0 \rightarrow J/\psi(1S) K^{*0}$ events	96
9.8. Proper time resolution of truth-matched selected $B_s^0 \rightarrow J/\psi(1S) \phi$ events .	97
9.9. Fit to the mass distribution of $B^+ \rightarrow J/\psi(1S) K^+$ candidates	99
9.10. Fit to the mass distribution of $B^0 \rightarrow J/\psi(1S) K^{*0}$ candidates	99
9.11. Fit to the mass distribution of $B_s^0 \rightarrow J/\psi(1S) \phi$ candidates	99
10.1. Toy study results for τ_B	105
10.2. Toy study results for m_B	105
11.1. Generated proper time distribution distorted into reconstructed distribution	108
11.2. Fitted acceptance for $B^+ \rightarrow J/\psi(1S) K^+$, alt. selection	109
11.3. Fitted acceptance for $B^0 \rightarrow J/\psi(1S) K^{*0}$, alt. selection	110

11.4. Fitted acceptance for $B_s^0 \rightarrow J/\psi(1S) \phi$, alt. selection	111
12.1. Projections of the two dimensional fit for $B^+ \rightarrow J/\psi(1S) K^+$, std. selection	116
12.2. Projections of the two dimensional fit for $B^+ \rightarrow J/\psi(1S) K^+$, std. selection	116
12.3. Projections of the two dimensional fit for $B^0 \rightarrow J/\psi(1S) K^{*0}$, std. selection	117
12.4. Projections of the two dimensional fit for $B^0 \rightarrow J/\psi(1S) K^{*0}$, std. selection	117
12.5. Projections of the two dimensional fit for $B_s^0 \rightarrow J/\psi(1S) \phi$, std. selection .	117
12.6. Projections of the two dimensional fit for $B_s^0 \rightarrow J/\psi(1S) \phi$, std. selection .	118
B.1. Projections of the two dimensional fit for the lifetime in $B^+ \rightarrow J/\psi(1S) K^+$, std. selection	140
B.2. Projections of the two dimensional fit for the lifetime in $B^+ \rightarrow J/\psi(1S) K^+$, alt. selection	141
B.3. Projections of the two dimensional fit for the lifetime in $B^0 \rightarrow J/\psi(1S) K^{*0}$, std. selection	142
B.4. Projections of the two dimensional fit for the lifetime in $B^0 \rightarrow J/\psi(1S) K^{*0}$, alt. selection	143
B.5. Projections of the two dimensional fit for the lifetime in $B_s^0 \rightarrow J/\psi(1S) \phi$, std. selection	144
B.6. Projections of the two dimensional fit for the lifetime in $B_s^0 \rightarrow J/\psi(1S) \phi$, alt. selection	145
B.7. Projections of the fit for the B^\pm / B^0 lifetime ratio , std. selection	146
B.8. Projections of the fit for the B^\pm / B^0 lifetime ratio , alt. selection	147
B.9. Projections of the fit for the B_s^0 / B^0 lifetime ratio , std. selection	148
B.10. Projections of the fit for the B_s^0 / B^0 lifetime ratio , alt. selection	149
B.11. Projections of the fit for the B^- / B^+ lifetime ratio , std. selection	150
B.12. Projections of the fit for the B^- / B^+ lifetime ratio , alt. selection	151

C.1.	J/ψ mass distribution from $B^+ \rightarrow J/\psi(1S) K^+$	153
C.2.	J/ψ mass distribution from $B^0 \rightarrow J/\psi(1S) K^{*0}$	154
C.3.	K^{*0} mass distribution from $B^0 \rightarrow J/\psi(1S) K^{*0}$	154
C.4.	J/ψ mass distribution from $B_s^0 \rightarrow J/\psi(1S) \phi$	155
C.5.	ϕ mass distribution from $B_s^0 \rightarrow J/\psi(1S) \phi$	155
D.1.	Zoom on the prompt peak region, $B^+ \rightarrow J/\psi(1S) K^+$	157
D.2.	Zoom on the prompt peak region, $B^0 \rightarrow J/\psi(1S) K^{*0}$	158
D.3.	Zoom on the prompt peak region, $B_s^0 \rightarrow J/\psi(1S) \phi$	158

List of Tables

1.1. Cross-sections at LHC	9
3.1. STBadLinkMasker results	37
4.1. GBE parameters	43
5.1. Number of events in the different datasets	52
5.2. Number of selected tracks	56
5.3. Summary of efficiency values	58
6.1. B-meson lifetimes	76
6.2. B-meson lifetime ratios	76
7.1. Number of events per Monte Carlo sample	78
9.1. Branching fraction for all decays and B-meson production fractions. Values from PDG[34] and from the Monte Carlo simulation are indicated.	84
9.2. $J/\psi(1S) \rightarrow \mu^+\mu^-$ selection	85
9.3. $B^+ \rightarrow J/\psi(1S) K^+$ selection	86
9.4. $B^0 \rightarrow J/\psi(1S) K^{*0}$ selection	87
9.5. $B_s^0 \rightarrow J/\psi(1S) \phi$ selection	88
9.6. Number of candidates per event	90
9.7. Efficiencies on Monte Carlo data, $B^+ \rightarrow J/\psi(1S) K^+$	91

9.8. Efficiencies on Monte Carlo data, $B^0 \rightarrow J/\psi(1S) K^{*0}$	92
9.9. Efficiencies on Monte Carlo data, $B_s^0 \rightarrow J/\psi(1S) \phi$	93
9.10. Mass PDF parameters from Monte Carlo data, std. selection	95
9.11. Mass PDF parameters from Monte Carlo data, alt. selection	95
9.12. Proper time resolution parameters from Monte Carlo data, std. selection	97
9.13. Proper time resolution parameters from Monte Carlo data, alt. selection	97
9.14. Signal and background yields	98
9.15. Signal purities	98
10.1. Toy study results for the lifetime ratio fitter	105
11.1. Acceptance correction values	110
11.2. Acceptance correction values for B^\pm	112
11.3. Acceptance correction values for B^\pm , split by polarity	112
12.1. Fitted lifetimes for the two selections	116
12.2. Estimation of the proper time resolution	119
12.3. Fitted ratios for the two selections	120
12.4. Fitted lifetimes for the two selections, reduced proper time range	120
12.5. Fitted ratios	121
12.6. Full fit results for $B^+ \rightarrow J/\psi(1S) K^+$ lifetime fit	122
13.1. Estimation of the signal mass model systematic uncertainty	124
13.2. Estimation of the background mass model systematic uncertainty	124
13.3. Estimation of the proper time acceptance systematic uncertainty (std. sel.)	125
13.4. Estimation of the proper time acceptance systematic uncertainty (alt. sel.)	126
13.5. Summary table of systematic uncertainties on lifetime, std. selection	127

13.6. Summary table of systematic uncertainties on lifetime, alt. selection . . .	128
13.7. Summary table of systematic uncertainties on lifetime ratio, std. selection	128
13.8. Summary table of systematic uncertainties on lifetime ratio, alt. selection	129
14.1. Measured lifetimes for the two selections	131
14.2. Measured lifetime ratios for the two selections	132
14.3. Measured particle / antiparticle lifetime ratios	132
A.1. Lifetime for $B^+ \rightarrow J/\psi(1S) K^+$, std. sel.	134
A.2. Lifetime for $B^+ \rightarrow J/\psi(1S) K^+$, alt. sel.	134
A.3. Lifetime for $B^0 \rightarrow J/\psi(1S) K^{*0}$, std. sel.	134
A.4. Lifetime for $B^0 \rightarrow J/\psi(1S) K^{*0}$, alt. sel.	134
A.5. Lifetime for $B_s^0 \rightarrow J/\psi(1S) \phi$, std. sel.	135
A.6. Lifetime for $B_s^0 \rightarrow J/\psi(1S) \phi$, alt. sel.	135
A.7. Lifetime ratio for B^\pm and B^0 , std. sel.	136
A.8. Lifetime ratio for B^\pm and B^0 , alt. sel.	136
A.9. Lifetime ratio for B_s^0 and B^0 , std. sel.	136
A.10. Lifetime ratio for B_s^0 and B^0 , alt. sel.	137
A.11. Lifetime ratio for B^- and B^+ , Std. sel.	137
A.12. Lifetime ratio for B^- and B^+ , alt. sel.	137

Curriculum Vitae

Johan LUISIER

Rue de la Gare 20
1607 Palézieux-Gare
Switzerland

Phone : +41 79 341 33 53
email : johan.luisier@a3.epfl.ch

Born : January 2, 1984
Nationality : Swiss
Marital status : Single

Education and degrees

2007 - 2011	PhD Studies in High-Energy Physics at LPHE (EPFL), supervised by Prof. Tatsuya NAKADA.
March 2007	M.Sc. degree in Physics, Swiss Federal Institute of Technology (EPFL). Member of the LHCb collaboration. Physics Studies at EPFL.
1999 - 2002	Maturité type “Physics and applied Mathematics”, Gymnase de Burier, price in Mathematics.

Languages

French Mother tongue
English Working language, good oral and written skills
German Basic knowledge from school

Computer sciences

- System administrator (Linux server) at LPHE.
- Good C++ programming skills (Qt, boost, ROOT).
- Knowledge of Python, Perl.
- Knowledge of Gaudi framework.
- Knowledge of PVSS.
- L^AT_EX.
- Basic knowledge of FORTRAN.

Research subjects

PhD studies :

- I was involved in the building of the Inner Tracker stations, and early commissioning.
- I was piquet for the Silicon Tracker.
- I developed a package to extract the Silicon Tracker TELL1 calibration from data. I then wrote a PVSS component to create recipes from a XML database.
- I studied the hit efficiency in the Inner Tracker.
- I provided the proper time acceptance correction for the ϕ_s measurement done at LHCb with 2010's data.

Master thesis : “Etude de faisabilité et implémentation d’un trigger à di-électron pour le HLT de LHCb”, Laboratory of High Energy Physics (LPHE), EPFL. The obtained results showed a significant improvement of efficiency for di-electron channels. This work was then carried on by my supervisor.

Presentations at international conferences

June 2011 “Performance of the LHCb Silicon Tracker detector in the LHC” given at the Second International Conference on Technology and Instrumentation in Particle Physics (TIPP), Chicago, USA, LHCb-TALK-2011-112.

Publications

- May 2011 “Tagged time-dependent angular analysis of $B_s^0 \rightarrow J/\psi(1S) \phi$ decays with the 2010 LHCb data”, R. Aaij et Al, LHCb-CONF-2011-006.
- May 2011 “Configuration of TELL1 boards from XML database with PVSS”, J. Luisier, CERN-LHCb-INT-2011-017.
- April 2011 “Selections and lifetime measurements for exclusive $b \rightarrow J/\psi(1S) X$ decays with $J/\psi(1S) \rightarrow \mu^+ \mu^-$ with 2010 data”, R. Aaij et Al, LHCb-CONF-2011-001.
- July 2010 “Measurement of the Inner Tracker Efficiency”, M. Needham and J. Luisier, CERN-LHCb-INT-2010-031.
-

Hobbies and interests

- 2008 - present Shooting instructor (assault rifle) for the “Société Amis du Tir Le Bouillet / Frenières / Bex”.
- 2007 - present Member of the “Chœur Atout”, a choir from Vevey, member of the committee since 2010.
-